PAPN 2015

Masaryk University

Potential Application of Plasma
and Nanomaterials 2015

Book of Contributed Papers

12. 11. – 13. 11. 2015

Brno

Czech Republic

Masaryk University

Potential Application of Plasma and Nanomaterials 2015

Book of Contributed Papers

12th November – 13th November 2015

Brno, Czech Republic

Brno 2015

Contact Address
NANOcontact
Masaryk University
Faculty of Science
Kotlarska 2
611 37 Brno
Czech Republic

tel: +420 549 498 677
e-mail: nanocontact@physics.muni.cz
http://nanocontact.cz

Editors
Jan Čech, Pavel Souček, Dana Skácelová, Jaroslav Hnilica

Preface

The conference „Potential Application of Plasma and Nanomaterials 2015" is a part of the project „Educational and contact center for nanotechnology surfaces modification for industry" at Masaryk University under the identification number CZ.1.07/2.4.00/12.0061 created within Operational Programme Education for Competitiveness – 2.4 Partnership and networks.

The aim of the conference is to enable to its participants an exchange of information and personal contacts between industrial companies and scientific researchers. This will enable setting up a mutual cooperation in the area of the surface nano-technological modification of materials.

The proceedings contain the contributed papers provided by the authors by November 24, 2015. The texts have not been edited.

<div align="right">The Local Organizing Committee</div>

Contents

Structure and mechanical properties of Ni doped nc-TiC/a-C(:H) coatings

J. Daniel[1] , P. Souček[1] , L. Zábranský , M. Stupavská[1] , K. Bernátová[1] , V. Buršíková[1] and P. Vašina[1]

[1]*Department of Physical Electronics, Masaryk University, Brno (Czech Republic),*
E-mail: pepadaniel@mail.muni.cz

Nanocomposite nc-TiC/a-C:H thin coatings combine mechanical properties such as high hardness with tribological properties, low friction and wear. In order to specifically design the physical and chemical properties of nc-TiC/a-C:H coatings selective doping with weak-carbide forming element can be used. In this paper we report on preparation and analyses of titanium-carbon coatings doped with a nickel. Hybrid PVD-PECVD process as well as HiPIMS process were used to deposit samples with various titanium, nickel and carbon content. Several sets of samples prepared with different deposition conditions. Chemical composition of the samples as well as structure of the samples and their hardness was analysed and compared.

1. Introduction

Transition metal carbide based coating systems have been systematically studied for decades because of their interesting combination of physical and chemical properties such as high hardness, low friction coefficient and good thermal stability [1]. These systems can form hard nanocomposite structure where nanocrystalline carbide grains are surrounded by amorphous carbon phase. One of the most widely studied transition metal carbides is a nc-TiC/a-C:H systeme which consists from nanocrystalline TiC grains embedded in an amorphous hydrogenated carbon matrix [2]. The synthesis of hydrogenated nc-TiC/a-C:H composite is mostly performed by sputtering of titanium target in hydrocarbon (acetylene or methane) containing plasma by a hybrid PVD–PECVD process [3, 4].

The main parameters which determines mechanical properties of nc-TiC/a-C(:H) coating system are the relative content of nanocrystalline and amorphous phases, size of the nanocrystalline grains or the mean grain separation (i.e. mean distance between two grains with shape usually approximated by cube [5]). A possible tool for influencing some of those parameters, e.g. size of the grains, is selective doping of this system by a non-carbide forming element such as nickel, proposed by Lewin et al. [6].

2. Experimental setup

Hybrid PVD-PECVD process of titanium target sputtering in argon and acetylene atmosphere enables us to deposit a set of nc-TiC/a-C:H coatings. Substrate holder was biased to -100 V. For different carbon content only flux of acetylene was changed. Two targets were used – 99.95 % Ti target for preparation of Ni-free coatings

7

and target which consists of 92.5 % of Ti and 7.5 % of Ni for preparation of Ni-doped sets of nc-TiC/a-C:H coatings.

The same sets of samples with Ni and without Ni were also prepared by high power impulse magnetron sputtering (HiPIMS). During HiPIMS deposition process the substrate was on the floating potencial.

Depositions of all coatings were made with well balanced magnetic field configuration. For all sets of samples, tungsten carbide (WC) as a substrate was used.

To determine the chemical composition, EDX analysis of the coatings were performed using Tescan MIRA FEG SEM equipped with an Oxford Instruments EDX detector.

Sizes of the nanocrystalline grains as well as the lattice parameter of the samples were determined using X-ray diffraction (XRD) utilizing Rigaku Difractometer SmartLab Type F, operated with Cu Kα radiation (wavelength 0.1542 nm) in a grazing angle of incidence configuration.

The structure parameters, such as the mean grain separation or the ratio of amorphous carbide phase (i.e. amorphous carbon matrix between the nanocrystalline grains) was determined by X-ray photoelectron spectroscopy (XPS). The Thermo Scientific *K*-Alpha XPS system (Thermo Fisher Scientific, UK) equipped with a micro-focused, monochromatic Al *K*α X-ray source (1486.6 eV) was used. The spectra were acquired in the constant analyzer energy mode with pass energy of 200 eV for the survey. The charge shift of the spectra was corrected by setting the C1s peak at 285 eV.

The hardness of the samples was measured by Fischerscope H100 depth sensing indenter (DSI) equipped with a Berkovich tip and than determined using standard Oliver-Pharr [8] method.

3. Results and discussion

Set of samples with different content of a carbon was prepared for both Ni-free and Ni-doped samples and the influence of a nickel in the nc-TiC/a-C(:H) system was tested. Sample composition as well as the presence of the nickel was determined using EDX technique attached to SEM. Although the target with the fixed ratio Ni/Ti to preparation of a Ni-doped coatings was used, a ratio Ni/Ti was no constant for coatings prepared with different acetylene flow rates.

X-ray diffraction analysis indicates that systeme consists only from TiC grains, no nickel grains were detected. We suppose that nickel is incorporated to TiC grains. Comparison of the grains size, obtained from XRD data, is shown in Fig. 1 (case of DCMS) and Fig. 2 (HiPIMS case).
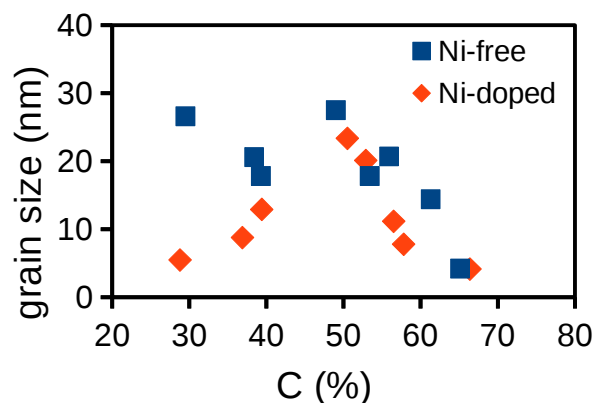
Fig. 1. Size of TiC nanocrystallites in the coatings prepared by DCMS.
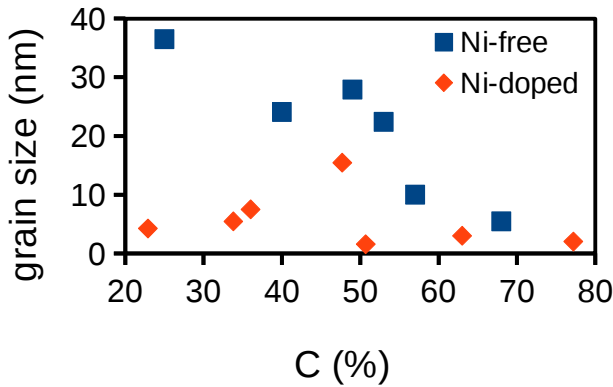
Fig. 2. Size of TiC nanocrystallites in the coatings prepared by HiPIMS.

Comparison of the lattice parameter evolution for DCMS and HiPIMS coatings is shown in Fig. 3. Only comparison of Ni-free coatings is presented, no influence of a nickel adition to lattice parameter was observed. As one can see, the lattice parameters of samples prepared by HiPIMS is also allways smaller then the lattice parameters of samples prepared by DCMS and even smaller than value of the lattice parameter of bulk TiC (4,328 Å) which is in agreement with Sarakinos et. al. [6] .
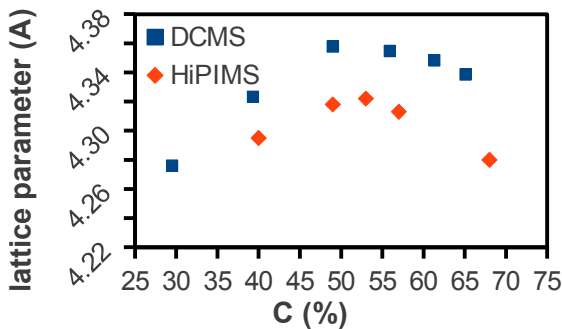
Fig. 3. Lattice parameter of the Ni-free coatings prepared by.

Hardness of the samples was obtained from nanoindentation analysis. Results (Fig. 4 and Fig. 5) shows that the coatings prepared by HiPIMS are more hard than coatings prepared by DCMS, but the nickel addition has almost no influence of the coating hardness.
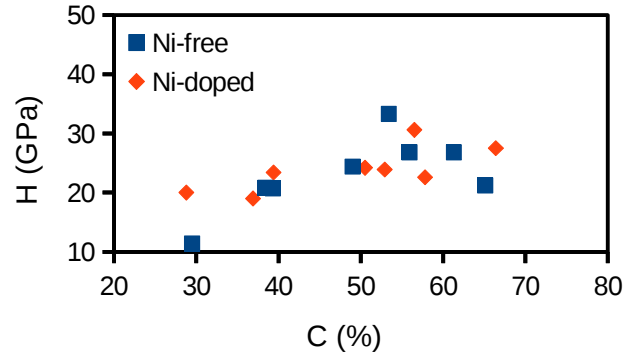
Fig. 4. Effect of Ni-addition on coating hardness. DCMS case.
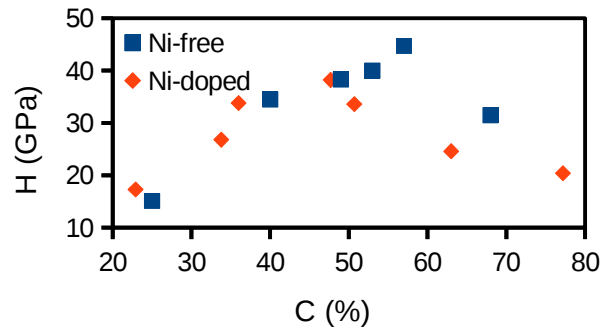
Fig. 5. Effect of Ni-addition on coating hardness. HiPIMS case.

In samples where total carbon content is up to about 50 - 55 % no significal influence of Ni-doping was observed. The Ni-free samples with lower carbon content are differs from the Ni-doped samples in grain sizes. XPS measurements shows us that addition of a nickel to coating causes increasing of amount of an amorphous carbon phase, according to assumption. A nickel is incorporate to the TiC nanocrystallites and a titanium made bonds with a nickel, because it is more energeticly favourable than bonds with a carbon. The carbon is than realased from the nanocrystallites to the amorphous matrix, as Lewin et. al. proposed [7].

From XPS data it can be obtained mean grain separation (MGS) of the Ni-free

coatings. The samples prepared by DCMS had a MGS about (0,8 - 1) nm, but the samples prepared by HiPIMS had a MGS only in the range from 0,5 to 0,8 nm. The amount of amorphous carbon phase for both of sets increase with incerasing total amount of carbon, but for coatings, where the total amount of C is less than cca 50 %, difference was observed. In DCMS prepared samples was about (20 – 30) % of amorphous carbone, but in HiPIMS prepared samples the amount of amorphous carbon rapidly decrese with decreasing total amount of C to 5 % for sample with 40 % of carbon.

Possible explanation for observed reduction of the grain sizes by the nickel addition would be effect of releasing of carbon from the nanocrystallites to amorphous matrix. Releasing of carbon can cause either increasing of an amorphous carbon content (and then increasing of MGS) or a reduction of grain size. Because the MGS is almost the same (or even smaller), released carbon covers the grains which can not growing. With increasing total content of carbon increases an amount of amorphous phase, effect of released carbon is less pronounced and a reduction of grain size decrease.

4 Conclusion

- Several sets of Ni-free and Ni-doped nc-TiC/a-C(:H) samples were prepared both by DC magnetron sputtering (hybrid PVD-PECVD process) and by high power impulse magnetron sputtering (HiPIMS).
- No influence of Ni-doping to hardness of coatings was observed.
- The lattice parameter of the grains in the DCMS prepared coatings is higher than the laticce parameter of the grains in the HiPIMS prepared

coatings in agreement with [6].
- With less than 50 % of total carbon content nickel doping has a strong influece of the grain size. Due to effect of the carbon releasing from nanocrystalline grains the size of the grains is smaller for Ni-doped coatings than for Ni-free coatings.

5 Acknowledgment

6 References

[1] A.A. Voevodin, J.S. Zabinski, J. Mater. Sci., **33** (1998), p. 319

[2] P. Souček et al., *Surface & Coating Technology* **211** 111-116 (2012)

[3] K. Polychronopoulou, C. Rebholz, M.A. Baker, L. Theodorou, N.G. Demas, S.J. Hinder, A.A. Polycarpou, C.C. Doumanidis, K. Böbel, Diamond Relat. Mater., **17** (2008), p. 2054

[4] W. Gulbinski, S. Mathur, H. Shen, T. Suszko, A. Gilewicz, B. Warcholinski, Appl. Surf. Sci., **239** (2005), p. 302

[5] U. Jansson, E. Lewin, *Thin Solid Films* **536**, 1-24 (2013)

[6] K. Sarakinos, D. Magnfält, V. Elofsson, B. Lü, *Surface & Coatings Technology* **257**, 326-332, (2014)

[7] U. Jansson, E. Lewin et al., *Surface & Coatings Technology* **206**, 583–590 (2011)

[8] W.C. Oliver, G.M. Pharr, J. Mater. Res., **19**, p.3 (2004)

Improvement of wettability high density polyethylene by plasma treatment: Impact of distance between sample and DCSBD electrode

H. Dvořáková[1] , M. Stupavská[1], Jan Čech[1] , P. Sťahel[1]

[1]Department of Physical Electronics, Masaryk University, Brno (Czech Republic), E-mail: hana.dvorakova@mail.muni.cz

Polyethylene is desired material in a broad range of industrial applications thanks its great mechanical properties and chemical resistance. The drawback of polyethylene is extremely low surface energy, which limits its usage in application requiring a wettability surface and good adhesion.

For this reason high density polyethylene (HDPE) was selected as testing material in this study. Polyethylene was treated using Diffuse Coplanar Surface Barrier Discharge (DCSBD) operated at frequency 30 kHz at atmospheric pressure in ambient air. Influence of distance between sample and DCSBD electrode on wettability plasma treated polyethylene was investigated. Sample-to-electrode distance was set at 0.1, 0.2 and 0.3 mm and treatment time was 1.5 s – 20 s.

Wettability of plasma treated polyethylene was evaluated via static contact angle measurement and calculation of surface energy. For an analysis of the atomic composition and functional group on the surface XPS was used.

1 Introduction

High density polyethylene (HDPE) is used in a broad range of industrial applications thanks its good mechanical properties. For some applications (e.g. biomedicine, microelectronics and production of composites) is necessary increasing its extremely low surface energy, which causes its poor adhesion and low wettability. [1, 2]

Improvement of wettability is traditionally performed by wet chemical treatment (etching or introduction of hydrophilic functional groups) [3, 4]. Besides chemical activation, UV-light, electron beams, ion beams, X-rays, γ-rays, lasers and plasma treatment can be used for surface modification. [2, 5]

Plasma treatment enables an increase of surface energy polymers without affecting the bulk properties during short treatment time [8]. The most frequently used method of plasma modification is treatment in low pressure discharge with common treatment time in the range of minutes. [6, 7, 8]

A promising alternative to low-pressure discharges are discharges operated at atmospheric pressure (jet, atmospheric pressure glow discharge (APGD) and dielectric barrier discharge (DBD)) [9, 10, 11, 12, 13], which do not require a vacuum system and have good applicability in industrial in-line processes. Standard treatment time of polymers is in the range of second due the higher concentration of active species.

The aim of this work is to optimize the conditions of plasma treatment, in order to obtain high surface energy of HDPE during the short treatment time. Surface activation was performed in the atmospheric Diffuse Coplanar Surface Barrier Discharge (DCSBD) because of its good applicability in in-line processes.

To determine the optimal treatment conditions three different distances between sample and electrode were used. The surface energy of plasma treated and untreated HDPE was determined by measuring the

sessile drop contact angles. Atomic composition and functional group on the surface was investigated via X-ray photoelectron spectroscopy (XPS).

2 Experimental
2.1 Material
Plates of HDPE with dimensions 2.5 x 9.5 cm^2 were used as substrate in this study. The surface energy of untreated HDPE was 38.6 mJ/m^2. In order to optimize for real industrial process, samples were not cleaned before plasma treatment. Therefore surface properties were not measured on the analytical clean surface.

2.2 Plasma treatment
Samples were modified in so called Diffuse Coplanar Surface Barrier Discharge (DCSBD) [14] operated at atmospheric pressure and in ambient air. DCSBD electrode with active discharge area 20 x 8 cm^2 consists of two parallel electrodes with IDT geometry embedded in flat dielectric from Al$_2$O$_3$ ceramic (Fig. 1).
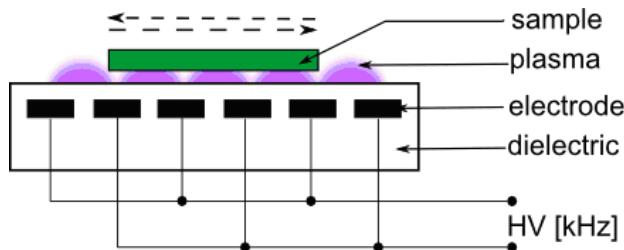
Fig. 1: *Schema of experimental setup.*

Discharge was generated using sine-wave high voltage with the operated frequency of 30 kHz. Power density was 3.25 W/cm^2. Sample-to-electrode distance was set at 0.1, 0.2 and 0.3 mm and treatment times were 1.5, 3, 5, 8, 10, 15 and 20 s.

2.3 Surface energy
Wettability and surface energy of samples was determined by measurement of static contact angle (CA) with use sessile drop method. The CA of two standard liquids

(water and diiodomethan) was measured using See system (Advex Instruments) and surface energy (SE) and their components were calculated by Owens, Wendt, Rabel and Kaelble model (OWRK):

$$(1 + \cos\theta)\gamma_l = 2\left(\sqrt{\gamma_s^{LW}\gamma_l^{LW}} + \sqrt{\gamma_s^{AB}\gamma_l^{AB}}\right)$$

LW stands for the Lifshitz-Van der Waals component of surface total surface energy and *AB* represents the acid-base component. $\cos\theta$ represents a measured contact angle of sample *s* with liquid *l*.

Total surface energy was determined by the sum *LW* and *AB* component of the surface energy:

$$\gamma = \gamma^{LW} + \gamma^{AB}$$

Contact angles for each sample and test liquid were measured eight times and first measurement was performed within five minutes after the plasma processing in order to reduce the aging effect.

2.4 XPS
The XPS measurements were done on the ESCALAB 250Xi (ThermoFisher Scientific). System is equipped with 500 mm Rowland circle monochromator with microfocused Al Kα X-Ray source. An X-ray beam with 200 W power (650 microns spot size) was used. The survey spectra were acquired with pass energy of 50 eV and resolution of 1 eV. High-resolution scans were acquired with pass energy of 20 eV and resolution of 0.1 eV. In order to compensate the charges on the surface electron flood gun was used. Spectra were referenced to the hydrocarbon type C 1s component set at a binding energy of 284.8 eV. The spectra calibration, processing and fitting routines were done using Avantage software. Control XPS measurement was performed on untreated samples.

3 Results

Wettability of HDPE significantly increased after plasma treatment in DCSBD.

Fig. 2 shows SE of plasma treated HDPE as a function of plasma treatment time for three different sample-to-electrode distances, i.e. 0.1, 0.2 and 0.3 mm.

SE of samples rapidly increased during first 3 seconds of plasma treatment and for longer exposure times value of SE increased only slightly due to saturation of the plasma treatment effect.

The highest values of SE were found in the saturated part of SE dependence, i.e. 50, 56 and 66 mJ/m^2 for sample-to-electrode distances 0.1, 0.2 and 0.3 mm, respectively.

It was found that sample-to-electrode distance has significant influence on the value of SE which increases with decreasing sample-to-electrode distance.
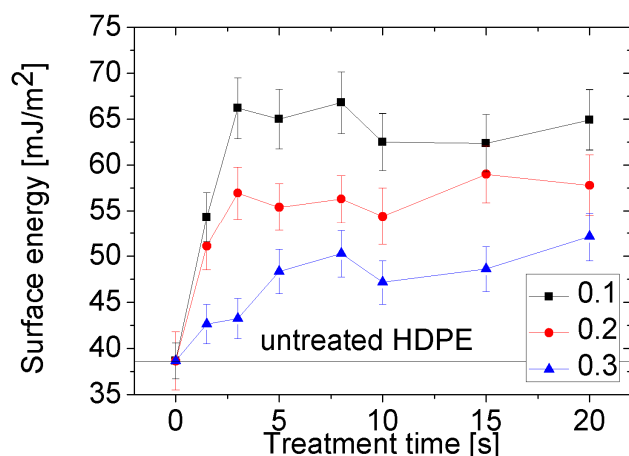
Fig. 2: *Dependence of surface energy of plasma treated HDPE on plasma treatment time for sample-to-electrode distances 0.1, 0.2 and 0.3 mm. Surface energy of untreated HDPE was 38,6 mJ/m^2.*

This dependence of SE corresponds well with results of XPS analyse. Table 1 shows the atomic and functional groups composition of untreated and plasma treated samples for three sample-to-electrode distances (0.1, 0.2 and 0.3 mm). O/C ratio and concentration of karbonyl (C=O) and karboxyl (O=C-O) functional groups

increased with decreasing distance sample-to-electrode.

This means that the sample-to-electrode distance influences not only the O/C ratio but also the concentration of oxygen functional groups on the surface.

sample-to-electrode distance	Un.	0.1	0.2	0.3
C-C/C-H (%)	96	56	71	78
C-O (%)	4	19	15	8
C=O (%)	0	14	8	7
O=C-O (%)	0	11	6	7

Tab. 1: *Atomic composition and functional groups on surface untreated and plasma treated HDPE for three different distances between sample and electrode. Exposition time was 15 s.*

4 Conclusion

Significant improvement of the wettability of HDPE was obtained by treatment using DCSBD in ambient air at atmospheric pressure. The excellent value of SE more than 66 mJ/m^2 was obtained for treatment time 3 s and sample-to-electrode distance 0.1 mm. This showed, that DCSBD plasma source is a suitable plasma source for plasma modification of HDPE in in-line industrial application.

We have found strong dependence between the value of SE and sample-to-electrode distance and results of XPS showed that this distance influences also concentration of oxygen functional groups.

5 Acknowledgment

6 References

[1] C.-M. Chan, T.-M. Ko, H. Hiraoka: Surface Science Reports 24 (1996), 1-54.

[2] J. Peyroux, M. Dubois, E. Tomasella, E. Petit, D. Flahaut: Applied Surface Science 315 (2014), 426-43.

[3] S.L. Fávaro, A.F. Rubira, E.C. Muniz, E. Radovanovic: Polymer Degradation and Stability 92 (2007), 1219-1226.

[4] A.P. Kharitonov, G.V. Simbirtseva, A. Tressaud , E. Durand , C. Labrugère, M. Dubois: Journal of Fluorine Chemistry 165 (2014), 49-60.

[5] S. Wu, J. Zhang , X. Xu: Polymer International 52 (2003), 1527–1530.

[6] M. Lehocký, H. Drnovská, B. Lapčíková, A. M. Barros-Timmons, T. Trindade, M. Zembala, L. Lapčík Jr: Colloids and Surfaces A: Physicochemical and Engineering Aspects 222 (2003), 125-131.

[7] D. M. Choi, C.K. Park, K. Cho, C.E. Park: Polymer 38 (1997), 6243-6249.

[8] H. Drnovská, L. Lapčík Jr., V. Buršíková, J. Zemek, A. M. Barros-Timmons: Colloid and Polymer Science 281 (2003), 1025–1033.

[9] M. Noeske, J. Degenhardt, S. Strudthoff, U. Lommatzsch: International journal of adhesion and adhesives 24 (2004), 171-177.

[10] N. Encinas, B. Díaz-Benito, J. Abenojar, M. A. Martínez: Surface and Coatings Technology 205 (2010), 396-402.

[11] S. Bhowmik, T. K. Chaki, S. Ray, F. Hoffman, L. Dorn: International journal of adhesion and adhesives 24 (2004), 461-470.

[12] G. Borcia, C. A. Anderson, N. M. D. Brown: Applied surface science 221 (2004), 203-214.

[13] M. Šíra, D. Trunec, P. Stahel, V. Buršíková, Z. Navrátil, J. Buršík: Journal of physics D: Applied physics 38 (2005), 621.

[14] M. Šimor, P. Vojtek, M. Černák, A. Brablec: Applied Physics Letters 81 (2002), 2716-2718.

Microwave diagnostics of low pressure and atmospheric plasma

Jan Faltýnek, Vít Kudrle

Department of Physical Electronics, Masaryk University, Brno (Czech Republic),
E-mail: faltynek@mail.muni.com

The paper presents microwave diagnostic techniques adapted to plasma sources in non-trivial geometries combined with numerical modelling. Their advantages and limitations are revealed by the experimental results.

1 Introduction
1.1 General introduction

The microwave (MW) techniques for material [1] and plasma diagnostics have been routinely used for more than 50 years [2]. The main advantage over even more popular spectroscopy and electric probes is, that they usually provide instantaneous data without much data processing left to handle. The measurement can be also very fast and often provides good temporal resolution while having negligible influence on the plasma due to low operating power. Finally with more diagnostic methods available, there are more possibilities to choose from. Apart from cross-verification of results, this freedom of choice is important as for numerous plasma sources at least some methods fail.

Naturally there can be complications to address in MW methods as well. Note that microwave wavelengths are comparable with characteristic dimensions of most experimental set-ups and the electromagnetic (EM) fields can therefore become very complicated. In effect this can contradict standard theory assumptions and various elaborate approximations must be used. In recent years this topic has experienced a renaissance with the advances in numerical modeling, allowing us to effectively treat problems that cannot be solved analytically or by simple approximations. The diagnostics of discharges in non-standard geometries and/or conditions is such a case.

This paper presents the experience with combination of microwave diagnostic methods and numerical modeling for the investigation of various plasma sources with non-trivial geometries.

1.2 Plasma as dielectric medium

From the electrodynamics point of view, the plasma properties can be described by either the complex conductivity or complex permittivity. Under certain assumptions the relation between plasma parameters and dielectric behavior (for which the complex permittivity is used) can be derived [1] from the Boltzmann equation, resulting in

$$\varepsilon_r = 1 - \frac{n_e e^2 (\omega + i\nu_m)}{m_e \varepsilon_0 \omega (\nu_m^2 + \omega^2)} \tag{1}$$

where m_e denotes mass of electron, e elemental charge, ε_0 permittivity of vacuum and ω the angular frequency of propagating waves. The variables (plasma parameters) are the electron density n_e and the electron-neutral collision frequency for momentum transfer ν_m.

Two popular methods are presented in this contribution. In first case the electron density is determined using the plasma influence on the resonator eigenfrequency. Second method involves the plasma induced phase shift of the propagating wave measured by microwave interferometry. The former is used to study in capacitively coupled plasma (CCP) at low pressures, while the latter investigates the surfatron filamentary

atmospheric plasma jet and the atmospheric dielectric barrier discharge in DCSBD configuration.

1.3 Open MW resonator method

Among many resonator types microwave resonators are particularly popular due to their convenient dimensions for laboratory use. The eigenfrequency of such a resonator is governed by two main factors – its geometry and its material properties. In case of the open resonator the electromagnetic field reaches outside the body of the resonator and therefore also the material surrounding the open end of the resonator slightly affects the eigenfrequency.

Our experimental solution [3] uses the X-band (~10 GHz) Gunn diode oscillator driven coaxial probe (i.d. 10 mm) excited in TEM mode. The probe is separated from the plasma chamber by silica tube (Fig. 1).
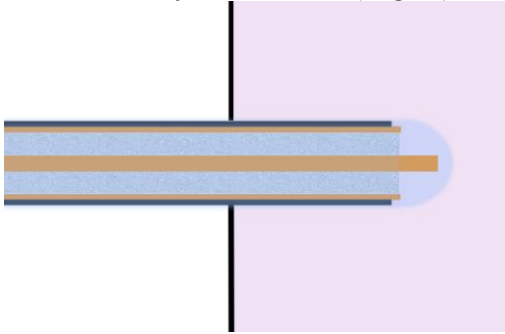
Fig. 1: *Coaxial resonant probe fitted into the plasma reactor. The silica tube (blue) separates the probe and plasma chamber.*

Since the electromagnetic field is expected to vanish with increasing distance from the probe, the plasma density could be in fact measured locally. The oscillation frequency is measured by counter several times per second and so the time dependent studies should be possible as well.

The studied low-pressure plasma is kept in stainless steel plasma reactor Temelin which has spherical shape (i.d. 25 cm) with two planparalell electrodes of which one is excited by RF generator PG 50 (maximum power of 50 W) at 13.56 MHz. The second electrode is grounded as well as the rest of the reactor walls.

Since the shift in eigenfrequency should be only small compared to its absolute value, dropping higher terms in Taylor expansion leads to a linear formula

$$n_e = A \cdot \Delta f \qquad (2)$$

where A is experimental constant.

1.4 MW interferometry of atmospheric plasma jet

Microwave interferometry is (similarly to resonator method) one of the best known and most used microwave methods. The universal concept of interferometry applied in microwave region has a few specifics (signal has to be transmitted through waveguides, usually TE_{10} mode is excited etc.), but regardless of that the general theory remains the same. For our experiments the Mach-Zehnder configuration with quadrature detection is chosen (Fig. 2). It provides real-time measurements and the possibility to separate the phase shift and changes in amplitude. Therefore it should be theoretically possible to simultaneously determine both n_e and ν_m.
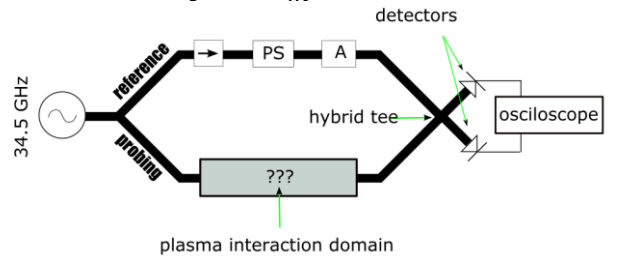
Fig. 2: *Mach-Zehnder microwave interferometer*

The phase shift $\Delta\varphi$ of the signal in the reference arm (r) and the probing arm (p) can be derived from power P incident on detectors (+ and −)

$$P_\pm = \frac{C}{4}\left(\frac{E_p^2}{2} + \frac{E_r^2}{2} \pm E_p E_r \cos(\Delta\varphi)\right) \quad (3)$$

where C is constant and the measurement is performed once with both arms open and once with reference arm attenuated.

In experiments the 34.5 GHz (Ka band) Gunn diode MW oscillator (Spacek Labs Inc. GKa-350) signal is split into probing and reference arms made of standard WR28 waveguide. In the reference arm a variable attenuator and variable phase shifter are placed. Faraday isolator in the reference arm suppresses any unwanted reflections. The signal from both arms is combined using the hybrid tee and detected by two microwave diodes (DKa-2N, Spacek Labs Inc.) and the detector output signal is digitized by Agilent DSO 1022A oscilloscope.

The plasma interaction domain is the unique feature for each plasma source. It has to be, as the electron density of atmospheric pressure with non trivial geometry is difficult to determine (unlike the case of CCP) by most methods due to the geometry and small dimensions of the plasma domain.

In case of surfatron (SAIREM 80) plasma jet (driven by 2.45 GHz SAIREM generator, mean power up to 300 W) the interaction of plasma filaments and microwaves takes place as the silica discharge tube (i.d. 1.5mm, o.d. 4 mm) passes through 8mm hole drilled in a broader side a waveguide section, see Fig. 3.
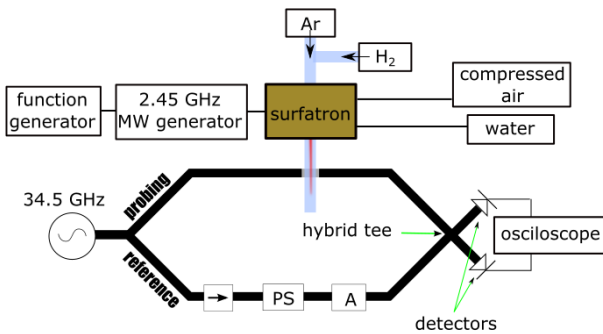
Fig. 3: *The interaction of plasma filaments and microwaves schematic for surfatron*

1.5   MW interferometry of DCSBD

The last discharge (studied by the same method and same interferometer as the atmospheric plasma jet) is the DCSBD device. Plasma is excited by 15 kHz high voltage generator and the approx. area covered by plasma can be up to 140 cm^2 at higher discharge power (in practice the maximum is 400 W).

This atmospheric plasma forms a thin (0.3 mm) layer over the dielectric (alumina) surface. More precisely the plasma is filamentary, but the macroscopic appearance is quite homogeneous.

The interaction of microwaves with plasma is mediated by a part of the probing arm which consists of a rectangular dielectric (PTFE) section with ends fitting into standard WR28 metallic waveguide. This dielectric waveguide is placed 1.5 mm above the ceramic DCSBD surface (Fig. 4). In this case the plasma interacts with microwave evanescent field over the whole width of the DCSBD device, (i.e. 7.5 cm) as the EM wave travels partially outside the dielectric waveguide in so-called hybrid mode.
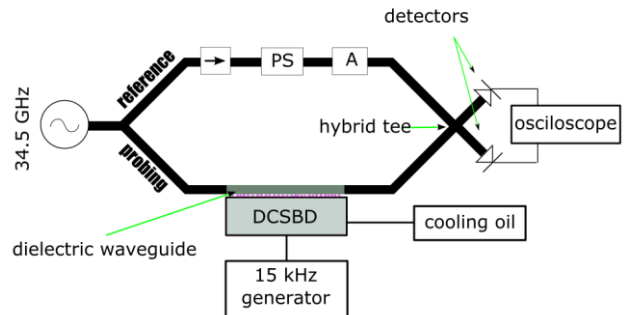
Fig. 4: *The interaction domain solution for DCSBD*

1.6   Numerical modelling

The geometry of these three discharges and experimental set-ups dictates the use of the numerical modelling as the classical assumptions are not satisfied. The finite element method (FEM) based software COMSOL Multiphysics (RF module) was used to simulate the plasma interaction domain of each discharge. More important

than the computed EM field is the eigenfrequency (in case of resonator probe) or phase shift (in case of interferometry) as functions of plasma domain material properties. While the phase shift is directly contained in elements of the model scattering matrix, the eigenfrequency can be identified in the frequency dependence of the reflection coefficient S_{11}. Such model may also answer more fundamental questions such as: "Is the EM wave transmitted through tiny plasma domains or is the scattering around the dominant process?" or "Can the proper choice of wavelengths change it?"

In short, results of modelling may be used to predict whether the considered method will be functional, treat different phenomena (such as occurrence of a second plasma filament in the discharge tube) or improve the classical formulae for electron density determination.

2 Results and discussion

2.1 Resonator probing of CCP discharge

In low pressure case the collisions are not as important as at the atmospheric pressure. The imaginary part of complex permittivity (1) therefore vanishes and we get its collisionless form

$$\varepsilon_r = 1 - \frac{n_e e^2}{m_e \varepsilon_0 \omega^2} \qquad (4)$$

which suggests that (with the help of proper numerical model) we could determine the plasma density directly.

While measurements of plasma (either in pure Ar or in Ar+O_2, pressure in range 5-12 Pa, discharge power up to 45 W) show that the method is functional and even Δf is linearly dependent on discharge power (which seems reasonable), parasitic phenomena, such as thermal expansion of the silica walls result in additional long-term shift in eigenfrequency (Fig. 5).
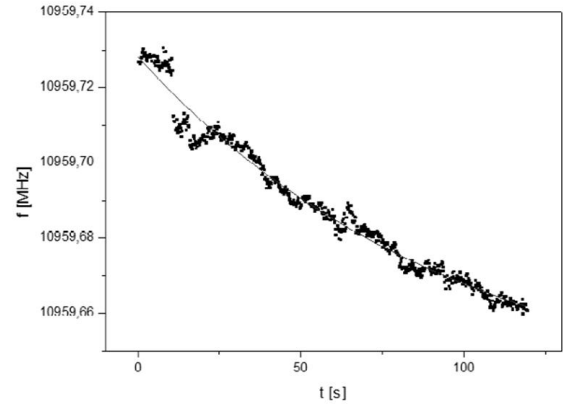
Fig. 5: *Resonant frequency sweep due to heating during 120 s*

Even though the sweep is rather slow and could be minimized by faster measurement (Fig.6), it effectively prevents sole use of numerical model. Moreover, the excited mode of the resonator is probably quite high which increases its sensitivity to imperfections such as vacuum pump vibrations (the probe is not fixed in silica tube).
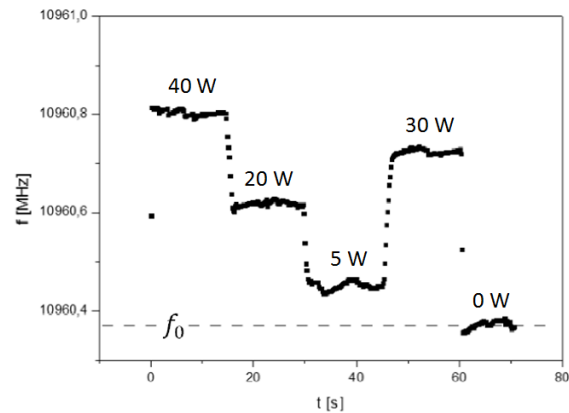
Fig. 6: *Measurement of the eigenfrequency at varying discharge power in pure argon*

Therefore the probe was calibrated using compensated Langmuir probe placed symmetrically in the discharge. It turns out that the experimental dependency between plasma density and eigenfrequency is linear and so the equation (2) is indeed correct.

Despite not being able to directly determine electron density, the numerical model is used to study an influence of the probe geometry on sensitivity of the method

and on the volume of the plasma domain affecting the eigenfrequency (Fig. 7).
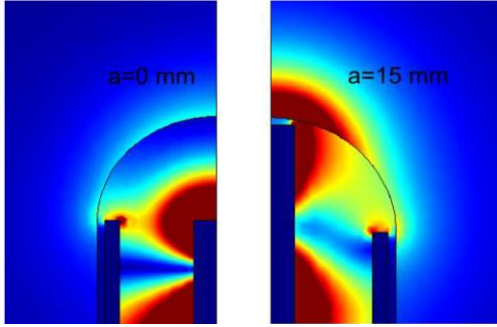
Fig. 7: *Computed EM field norm for different length "a" of the central conductor.*

Generally speaking the probe results show that this method is perfectly adequate for stationary low pressure plasma and could provide spatially resolved electron density in suitable configuration. Obviously the temporal resolution is too low to observe plasma decay processes, yet processes in order of seconds and higher can be studied.

2.2   MW interferometry of atmospheric plasma jet

In case of the second studied plasma [4] source the microwave interferometry was employed. The problems present in resonator method are insignificant here (partly due to lesser sensitivity of interferometric measurement to geometric imperfections or heating). The atmospheric pressure operation however implies that (1) cannot be simplified and therefore one more degree of freedom represented by the collision frequency has to be solved. As mentioned in section 1.4, this could be possible thanks to the quadrature detection.

In this case, the numerical model is also needed. We can see for example (Fig. 8), that the analytical plot of phase shift is completely different from the one predicted by the numerical model.
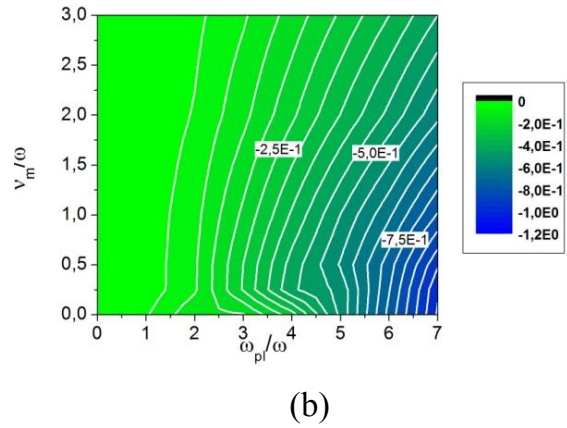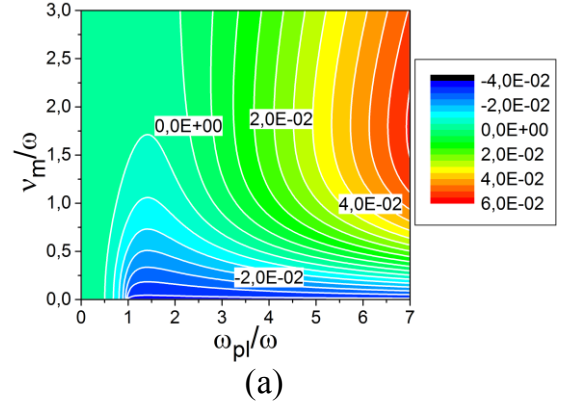
Fig.8 *Comparison of analytical (a) and model (b) phase shift per length of plasma domain wrt. plasma parameters.*

Unfortunately there is even one more unknown that cannot be avoided in these cases and that is the power channelling outside of the interferometer. In both cases it cannot is inevitably present (by principle) and varies greatly in the presence of plasma. Therefore the determination of collision frequency by standard interferometry is very inaccurate. At this point both references from other authors [5] and the numerical model results suggest the approximate value of $\nu_m = 2 \times 10^{11} s^{-1}$.

While the measurement of discharge in continuous wave regime is common, this study focused on amplitude modulated regime (the discharge power modulated by sine function) is interesting regarding the temporal resolution of the method. The plot of 1717 Hz modulated discharge (Fig. 9) shows that it is very precise and such

interferometer could be even used to study decay processes in plasma.
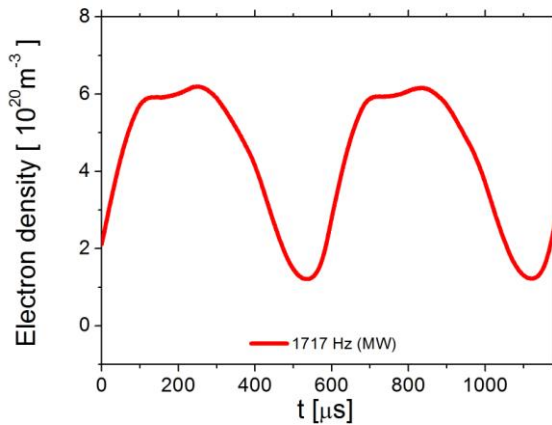
Fig.9 *Temporal evolution of plasma density during two periods of amplitude modulation.*

2.3 Interferometry of DCSBD

Finally we have the DCSBD plasma in the air to be diagnosed. The discharge power at 15 kHz is varied between 100 and 300 W. The 1.5 mm distance between dielectric waveguide and the dielectric barrier (Fig. 10) surface is a compromise – getting too close results in loss of the signal (channelling out of the system) while large distance the EM wave does not interact with plasma.
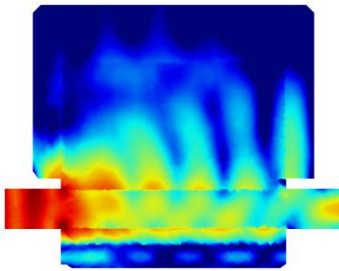
Fig. 10: *Logarithm of the electric field norm in the side view (with clearly visible dielectric waveguide, air gap + plasma and alumina)*

As data on oscilloscope read, with increasing discharge power there is indeed increasing phase shift observable. Thorough examination of the phase shift and its slow temporal evolution suggests however that in this third case, the microwave interferometry fails.

In reality the phase shift is induced by the heating and thermal expansion of the dielectric waveguide and not by the plasma itself. Similarly to 2.2, measurement on short time scale with abrupt changes of discharge parameters could separate the plasma induced and heating induced phase shifts. It is better to measure when switching off the discharge (as the apparent change is more abrupt than when switching the discharge on). Unfortunately, to the best of our efforts, no phase shift induced by plasma is measureable even then.

Let us discuss the reason why the method is insensitive to the plasma presence. Plasma filaments in this case could be too dense (EM waves rather scatter on plasma filaments rather than going through them) and due to the orientation of wave propagation and the plasma plane the scattering is also negligible. Extremely low plasma density ($n_e < 5 \times 10^{18}$ m^{-3} according to model) could also have this effect, although it is not as likely – measurement performed with 15 GHz interferometer in the same configuration shows no phase shift as well.

3 Conclusion

After this case study we may state that microwaves are very powerful tool on its own. They can determine the electron density easily with temporal and spatial resolution. Now that computational power of numerical solvers has grown the modelling methods are also a popular topic in the community and some scientists focus only on modelling, predicting results in hypothetical situations. In all presented studied cases, it can be seen that the possible experimental issues the method may have can be addressed by numerical model and vice versa (models generally need to be compared with reality), thus the symbiosis of experiment and modelling is very effective similarly as the combined use of more methods at once is more powerful tool than each method

separately (such as the Langmuir probe and the resonant MW probe). Finally while every numerical model is limited when compared to real world, a reasonable model can be successfully used to estimate some directly immeasurable unknowns (e.g. ν_m in MW interferometry)

4 Acknowledgment

5 References

[1] Tesař J.: Měření permitivity plynů rezonátorovou metodou, diploma thesis, MU, Brno, (2010)

[2] Heald M. A. and Wharton C. B.: Plasma Diagnostics with Microwaves, New York, Wiley (1964)

[3] Faltýnek J.: Určení hustoty plazmatu rezonátorovou metodou, bachelor thesis, MU, Brno, (2012)

[4] Faltýnek J.: Mikrovlnná diagnostika plazmatu, diploma thesis, MU, Brno, (2014)

[5] Vyskočil J., Musil J.: J. Phys. D: Appl Phys., 13 (1980) L25–L28.

Effect of pulse off time on temporal evolution of sputtered species densities in multi-pulse HiPIMS discharge

M. Fekete[1], J. Hnilica[1], P. Vašina[1]

[1]*Department of Physical Electronics, Masaryk University, Brno (Czech Republic), E-mail: mfekete@mail.muni.cz*

The aim of this paper is to experimentally study effect of preceding pulse on the temporal evolution of number densities of sputtered species during the subsequent pulse for different delay time between two successive high-power pulses in the pulse packet. Time evolutions of sputtered species during and after pulse in single-pulse mode are presented, too. Intensities of selected lines of buffer gas were acquired during every measurement.

1 Introduction

High power impulse magnetron sputtering (HiPIMS) is nowadays often discussed topic. Intensive gas rarefaction taking place during the HiPIMS pulse decreases the number of sputtered species and buffer gas atom collisions and influences the velocity distribution function of sputtered atoms in the direction parallel to the magnetron cathode as was experimentally shown in [1]. Consequently, the gas rarefaction should not influence only the deposition rate, but should decrease the resident time of the sputtered atom in the magnetized plasma region and simultaneously its ionization probability. Back diffusion of buffer gas atoms is relatively time-consuming process (at least several hundred of μs as modelled by [2]). Sequences of successive short high-power pulses significantly increase the deposition rate compared to standard HiPIMS process keeping similar ionization efficiency of the sputtered species because the multi-pulse operation with short pulses limits the metal ion back-attraction [3]. The development of the subsequent pulse should be influenced by the preceding pulse. The local density of the buffer gas at the beginning of the pulse will be reduced by action the preceding pulses. The aim of this paper is to perform an experimental study of the effect of the preceding pulse on the time evolution of the concentration of titanium atoms and ions during the upcoming pulse as a function of the delay time between these two successive pulses. The measured data will be mutually compared and discussed.

2 Experimental setup

Measurements were realized on the magnetron sputtering system Alcatel SCM 650. The sputtering system was equipped with Ti target (99.95% purity) of 200 mm diameter and balanced magnetic field configuration. The discharge was powered by a Melec SIPP 2000 HiPIMS generator. The maximum allowed voltage is up to 1 kV and maximum allowed current is up to 500A. The pulse length was set to 200 μs. Repetition frequency was 20 and 10 Hz in single-pulse and multi-pulse mode, respectively.

The deposition chamber was pumped by Roots and turbomolecular pump to a pressure of 10^{-4} Pa. Argon (99.999%) was used as a buffer gas. The working pressure was set to 5 Pa, measured by MKS Baratron and argon gas flow was 135 sccm.

The Melec generator is equipped with a current and voltage probe for electric measurements. The optical emission spectroscopy (OES) has been carried out using a Jobin-Yvon Horiba FHR1000

spectrometer (Czerny-Turner) with 1 m focal length and 2400 grooves·mm⁻¹ grating. Intensified CCD camera (Andor IStar 720) served as a detector. The total integration time was set to achieve sufficient line intensities. The optical fibre was placed to moveable holder to collect the light 2.6 cm above the target.

3 Results and discussion

The number densities of sputtered species in their ground levels were calculated using on-site developed technique based on effective branching fractions. In the technique, theoretically determined branching fractions (which are functions of ground state densities of atoms and ions) are fitted to experimentally measured fractions of the relative intensities of carefully selected lines of measured species. Also intensity of Ar atom line (696.54 nm) and Ar ion line (434.80 nm) was examined under these conditions.

3.1 Single-pulse operation

Time evolution of titanium atom and ion number density during intense HIPIMS pulse was studied (see Fig. 1). Titanium atom density starts to increase rapidly at the time of 40 µs after the beginning of the pulse; it shows a maximum (5×10^{17} m⁻³) at time of 70 µs followed by a slow decrease. Ti ion density starts to increase at time 40 µs after the beginning of the pulse similarly as the titanium atom density. This increase can be divided into two phases; during the first phase till the time of 100 µs the increase of titanium ion density is faster compared to the second phase (after 100 µs). Time evolution of the total concentration of all sputtered titanium particles (i.e. ions and neutrals - see Fig. 1) very well reproduces the temporal evolution of the discharge current. Thus, as the discharge current increases, more titanium particles are sputtered from the target and also the ionized fraction of the
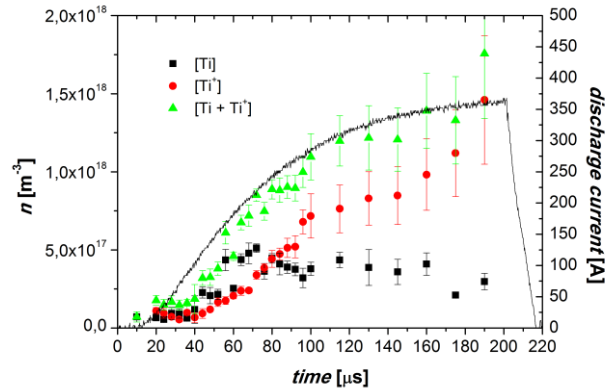
Fig. 1: *Temporal evolutions of sputtered species number densities during the 200 µs HiPIMS pulse.*

sputtered particles increases. 50 percent ionization of sputtered particles is achieved at time of 80 µs.

Temporal evolution of Ar atom and ion line intensity is shown in Fig. 2. Initial fast increase of Ar atom line intensity is after 40 µs followed by a rapid decrease and from the time of approx. 100 µs, the Ar atom line intensity is stable. This time evolution can be assigned to combination of buffer gas rarefaction and fast cooling of the electron temperature by sputtered particles. Intensity of Ar ion line follows the evolution of the discharge current.
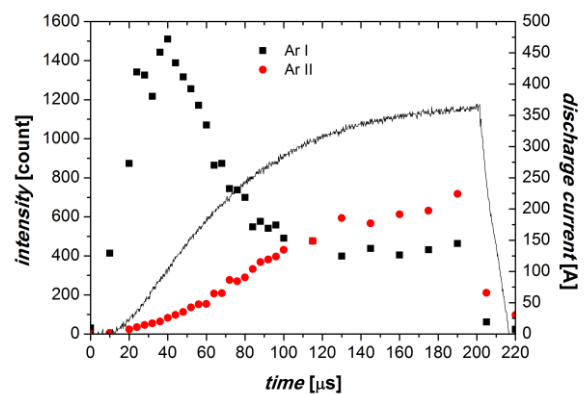
Fig. 2: *Temporal evolutions of intensities of Ar lines during the 200 µs HiPIMS pulse.*

To obtain the time evolution of the concentration of the sputtered particles after the end of the intense HIPIMS pulse i.e. in the off time, when the active discharge is

already terminated and no energetic electrons are present, it is necessary for the application of developed spectroscopic method to provide additional excitation of sputtered particles. Thus, sufficiently short and relatively weak scanning pulse was applied at different times after finishing of the main pulse to excite the sputtered species remaining from the main intense HiPIMS pulse. Pulses were excited by the same voltage, the length of the main intense HiPIMS pulse was set to 200 μs, and the length of the scan pulse was set to 30 μs. The spectra were integrated over the whole scan pulse and it is supposed that the amount of sputtered species during the scan pulse is negligible compared to residual densities of the sputtered species produced during the main pulse.
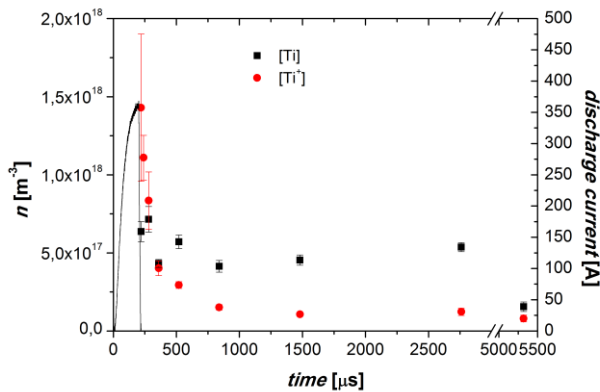
Fig. 3: *Sputtered species number densities during the off time.*

Number density of Ti atoms and Ti ions is shown in Fig. 3 together with the evolution of the discharge current of the main pulse. The density of Ti ions is much higher at the end of the main pulse compared to the density of Ti atoms. Nevertheless, the Ti ions number density decreases rapidly in comparison with Ti atoms number density. It was attributed to different transport mechanisms of titanium atoms and ions after the end of the HiPIMS pulse. Atoms are being transported by diffusion, however ions obey ambipolar diffusion which is faster.
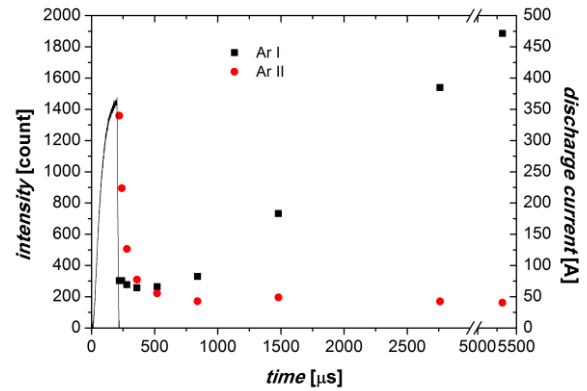
Fig. 4: *Intensities of Ar lines during the off time.*

On Fig. 4, there is plotted the evolution of the intensity of Ar atom and Ar ion line acquired during the scan pulse. The Ar ion line intensity is relatively constant after approx. 500 μs, however Ar atom line intensity steadily increases. Fast decrease of Ar ion line intensity was attributed to fast transport of Ar ions out from the studied region governed by ambipolar diffusion. Non-zero intensity of Ar ion line for times higher than 500 μs is attributed solely to the excitation of ions created during the scan pulse. The increase in intensity of Ar lines is observed from the end of the main HiPIMS pulse up to a maximum study time of 5 ms. The characteristic diffusion time of Ar atoms into the magnetized region from its perimeter was measured [1] and modelled [2], [4] to be in the order of several hundred of microseconds. The observed long-lasting increase in the intensity of the Ar atom line can not be attributed solely to back diffusion of Ar atoms into the studied area.

3.2 Multi-pulse operation
A pulse packet containing two successive HiPIMS pulses, each of the duration of 200 μs, was created. The temporal evolution of the number densities of Ti atom and Ti ion was determined for the multi-pulse operation of the HiPIMS process as a function of the delay time between the pulses in the pulse

packet. The results obtained for delay times of 200 µs, 400 µs and 1500 µs are shown in Fig. 5. Time evolutions of sputtered species densities of the first pulse in the pulse sequence are identical to the evolutions in the single-pulse mode operation and are discussed is Section 3.1.
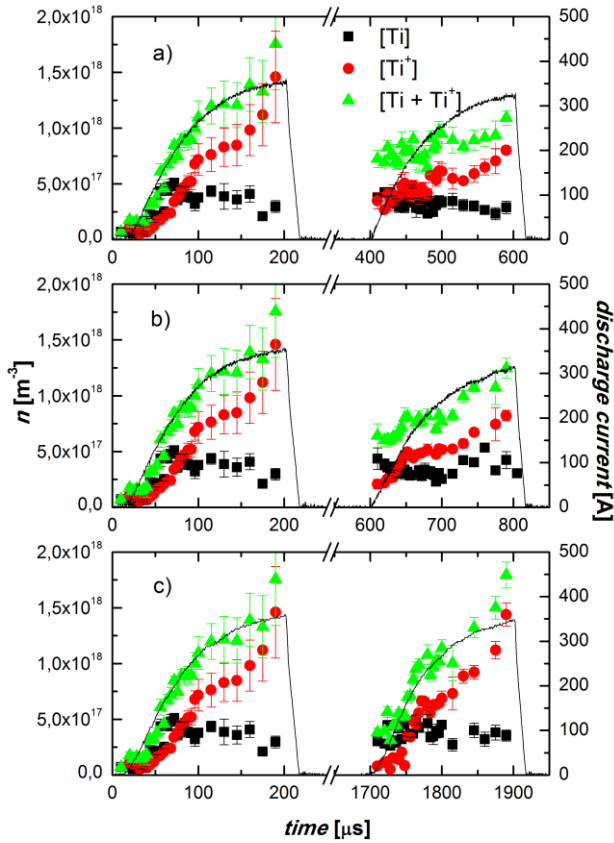
Fig. 5: *Evolutions of sputtered species number densities in multi-pulse mode with delay time: a) 200 µs, b) 400 µs and 1500 µs.*

Temporal evolution of titanium atom density of subsequent pulse from pulse packet with 1500 µs delay (Fig. 5c) starts from non-zero value of 4x10^{17} m^{-3} and stay constant at this value during the whole pulse. This initial non-zero number density is remainder of the titanium atoms produced by the preceding pulse. The initial density of Ti ions is very low (close to our detection limit). Fast transport (ambipolar diffusion) of titanium ions causes zero value of titanium ion density at the beginning of the subsequent pulse (see Fig. 3) in the case of

1500 µs off time. Despite that the initial density of Ti ions in the beginning of the subsequent pulse is zero. The time evolution of Ti ion density during the subsequent pulse is different compared to the preceding pulse. Ti ion density increases faster in the first phase compared to the preceding pulse evolution. The breakpoint into the second phase is observed earlier (70 µs after beginning of the subsequent pulse compared to 100 µs of the preceding pulse). The value (1.5x10^{18} m^{-3}) of the Ti ion number density at the end of the subsequent pulse is equal to the value of Ti ion number density at the end of the preceding pulse. 50 percent ionization of sputtered particles is achieved at the time of 60 µs. Faster evolution was attributed to the non-zero value of Ti atom density at the beginning of the subsequent pulse. Already at the beginning of the subsequent pulse there exists a reservoir of slow, thermalized neutral titanium atoms, which can be very easily ionized and thus more rapid increase in the concentration of ions in comparison with the case of the preceding pulse can be expected. At the end of the subsequent pulse, the sputtered particles produced during the subsequent pulse substantially exceed the residual particle concentration originating from the preceding pulse. Thus, the influence of the preceding pulse should be negligible and the values of the Ti atom and ion density at the end of the subsequent pulse should be the same as at the end of the preceding pulse. Time evolution of the total concentration of all sputtered titanium particles well reproduces the temporal evolution of the discharge current, except the initial stage of the subsequent pulse. In conclusion, even for relatively large off time such as 1500 µs, the influence of the preceding pulse on the subsequent pulse was proved.

For the three studies off times of 200 µs, 400 µs and 1500 µs the residual value of the titanium atom density at the beginning of the subsequent pulse remains unchanged at

value of approx. 4×10^{17} m^{-3}, see Fig. 5. The residual Ti ion density for the off time of the 400 μs is clearly non-zero, see Fig. 5b. Temporal evolution of titanium ion density starts at the value 2×10^{17} m^{-3}. Transition into the second phase occurs at the time of 50 μs after the beginning of the subsequent pulse, whereas the same was detected at 100 μs in the preceding pulse. The transition into the second phase for the subsequent pulse with off time of 1500 μs was detected at time 70 μs after beginning of the subsequent pulse. So, the first phase in the subsequent pulse with off time of 400 μs is sharper and shorter compared to both the preceding pulse and the subsequent pulse with larger off time of 1500 μs. The value of Ti ion density attained at the end of the pulse with off time of 400 μs is lower (7.5×10^{17} m^{-3}) compared to the value attained at the end of the preceding pulse and also the subsequent pulse with off time of 1500 μs. Time evolution of the total concentration of all sputtered titanium particles reproduces the temporal evolution of the discharge current after 50 μs from the beginning of the subsequent pulse. 50 percent ionization of sputtered particles is achieved at time 40 μs, i.e. earlier compared to the preceding pulse and also the subsequent pulse with off time of 1500 μs. Reduction the off time of 1500 μs to 400 μs therefore accelerates the time development of the Ti ion density in the first phase, but at the end of the subsequent pulse much lower concentrations are reached.

In the case of sequence of the pulses with the 200 μs off time between two successive pulses, see Fig. 5a, only the second phase of temporal evolution of titanium ion density is observed. The value (7.5×10^{17} m^{-3}) of Ti ion density at the end of the subsequent pulse is equal to the value of Ti ion density at the end of the subsequent pulse in case of 400 μs off time between two successive pulses i.e. much lower than the maximum value attained during the preceding pulse. 50

percent ionization of sputtered particles is achieved already at the beginning of the subsequent pulse where both the residual Ti atom and ion density equals 3×10^{17} m^{-3}. Total concentration attained at the end of subsequent pulse of the sputtered species is the lowest from all tested pulses.

4 Conclusion

Using on-site developed spectroscopic method, the time evolutions of the Ti atom and ion densities during and after single HiPIMS pulse and for a sequence of two successive HiPIMS pulses were determined. Two phases in the temporal evolution of titanium ion density were identified. The first phase is characterized by fast increase of the Ti ion density which increases much slowly in the second phase. In multi-pulse operation, the transition between these two phases is kept constant for the preceding pulse. However, it shifts towards the beginning of the subsequent pulse as the off time between the pulses in the pulse packet decreases. After the preceding pulse, the Ti ion density decreases faster than Ti atom density. Even for very large off time (1500 μs) the residual density of Ti atoms originating from the preceding pulse was detected at the beginning of the subsequent pulse. Non-zero value of Ti atom at the beginning of the subsequent pulse causes probably faster increase of Ti ion density in the first stage of the subsequent pulse development compared to the preceding pulse in the pulse packet.

6 References

[1] M. Palmucci, N. Britun, S. Konstantinidis, R. Snyders, J. Appl. Phys. 114 (2013) 113302

[2] C. Huo, M. A. Raadu, D. Lundin, J. T. Gudmundsson, A. Anders, N. Brenning, Plasma Sources Sci. Technol. 21 (2012) 045004

[3] O. Antonin, V. Tiron, C. Costin, G. Popa, T. M. Minea, J. Phys. D: Appl. Phys. 48 (2015) 015202

[4] T. Kozák, A. D. Pajdarová , J. Appl. Phys. 110 (2011) 103303

Surface dielectric barrier discharge generated using liquid electrodes and it application for surface treatment of polymer tubes

O. Galmiz[1], D. Pavliňák[1], M. Zemánek[1], A. Bucek[1], A. Brablec[1], and M. Černák[1]

[1]Department of Physical Electronics, Masaryk University, Brno, Kotlarska 2, 60137, Czech Republic. E-mail: oleksandr.galmiz@gmail.com

In this contribution authors present an atmospheric pressure plasma technique developed for technically simple treatment of inner and/or outer surfaces of hollow dielectric bodies e.g. plastic tubes. It is based on a novel type of surface dielectric barrier discharge that is generated along the surface of treated dielectric using water-solution electrodes. The discharge was studied by optical emission spectrometry in order to estimate the rotational and vibrational temperatures. The effect of plasma treatment on PTFE and PVC tubes was verified by contact angle measurements.

1.　　Introduction

Non-thermal atmospheric pressure plasmas in comparison with those of low-pressure plasmas often provide more convenient and cheaper alternatives for industrial applications [1]. That is why it has been studied for a variety of applications such as generation of ozone, pollution control and plasma medicine applications [2].

One of the most significant areas of atmospheric-pressure plasma applications are surface activations [3,4] of various materials, where active species (charged and excited particles, radiation, radicals, etc.) generated by the plasma react with the surface of material removing the contaminants from the surface and introducing there new functional groups. In this way the surface properties as wetting, adhesion, and printability [5] may be significantly influenced.

For more than a half of century dielectric barrier discharges (DBDs) have been used for the surface activations of man-made polymer materials [6,7]. One of such configurations is the surface dielectric barrier discharge (SDBD) arrangement. In this arrangement the discharge develops from a metallic electrode and propagates along the surface of a dielectric material serving as a dielectric barrier between the discharge electrodes. A disadvantage of SDBDs for many applications is a short life time of their metallic electrodes due to their galvanic contact with the reactive plasma.

Another type of the non-thermal plasma generating atmospheric-pressure gas discharges attracting increasing attention mainly because of their ability to produce strongly oxidizing species (OH, O, H_2O_2, etc.) and UV radiation is the discharge generated in contact with water or other liquids [8–10].

The studies of the application of such discharge were focused, mainly, on the water remediation, however, also the applications for the polymer plasma surface activations of polymers have been already studied [11–13].

Combining the basic features of SDBDs and using water-solutions as the discharge electrodes, a plasma technique was

developed both for the water remediation and plasma activations of hollow body surfaces. To illustrate the application potential of such SDBD and its basic physical properties we present a simple example of permanent hydrophilization of inner and outer surfaces of polytetrafluoroethylene (PTFE) tubes, which are widely used in engineering but their hydrophobic surfaces often limits applications, e.g., in the biomedical field. And, polyvinyl chloride (PVC) tubes which play a key role in the plastics industry and continues to be a polymer of major importance.

2. Experimental setup

The schematic block drawing of the SDBD is shown in Fig. 1 while the reactor chamber and the side view in to the reactor are shown in Fig. 2. The discharge was generated at atmospheric pressure from the boundary line of air, dielectric barrier, and the surface of 5% solution of oxalic acid in distilled water with the conductivity of 70 mS/cm. The oxalic acid was used to increase the conductivity of water.

The electrodes were situated inside of a glass dish (volume 50 ml) filled with approximately 200 ml of the oxalic acid solution. The PTFE or PVC tube (dielectric barrier) was filled with the solution which was connected to the generator by the stainless steel electrode.

During our experiments the system was operated at up to 30 W power, and the discharge plasma was ignited along the whole outer perimeter of the tube (3 cm).

All photos of discharge were done with the camera Casio EXF1.

a)

b)
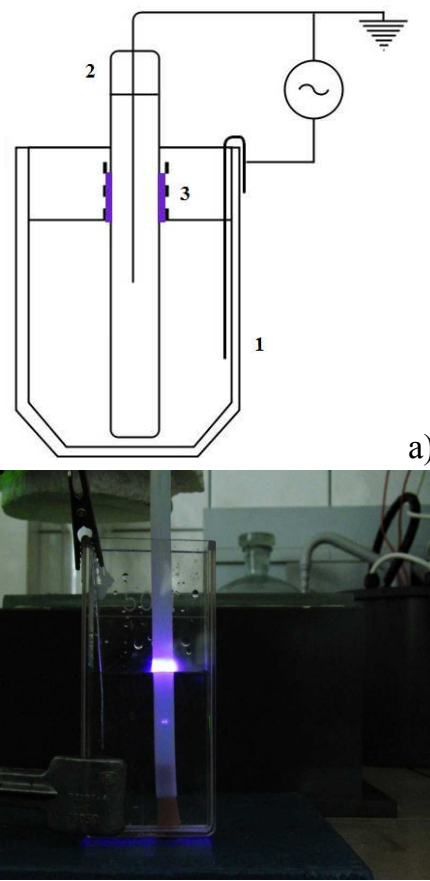
Fig. 1: *a) schematic drawing of the SDBD reactor: 1 – glass reactor with oxalic acid solution, 2 - PTFE or PVC tube with 5 ml oxalic acid solution (conductivity 70 mS/cm), 3 – plasma region, b) photo of the glass reactor.*

During the plasma treatment the tube was mounted in one position and the thin visually diffuse plasma layer generated in ambient air was moved from the top of the tube to its lower part. This effect was achieved by changing of solution levels. For that the reactor was moved down with the constant controlled speed.
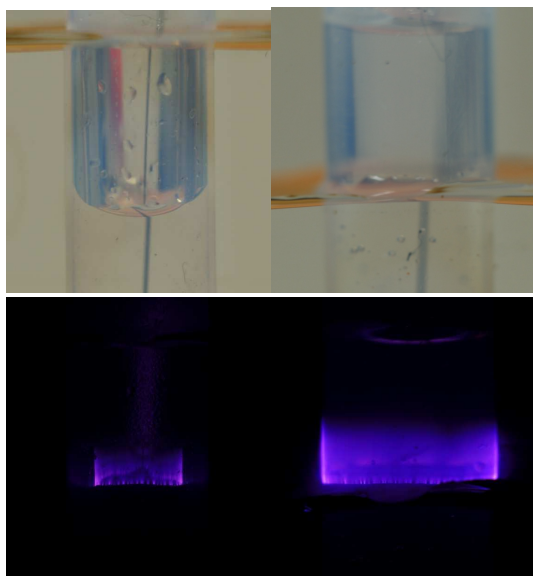
Fig. 2: *Photos of the reactor and discharge.*

nitrogen, the 306.3 nm system of OH radicals and the first negative system N_2^+ ($B^2\Sigma_u \rightarrow X^2\Sigma_g$).
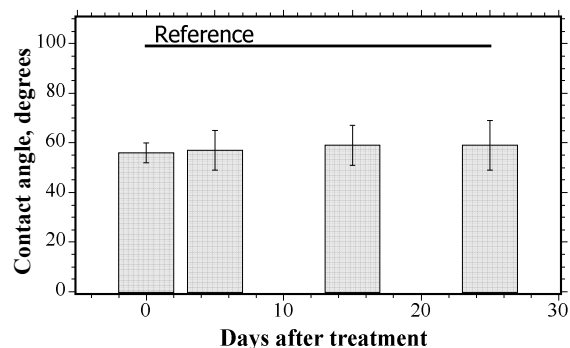
Figure 3. *Graph of aging effect on plasma treated PTFE tubes.*
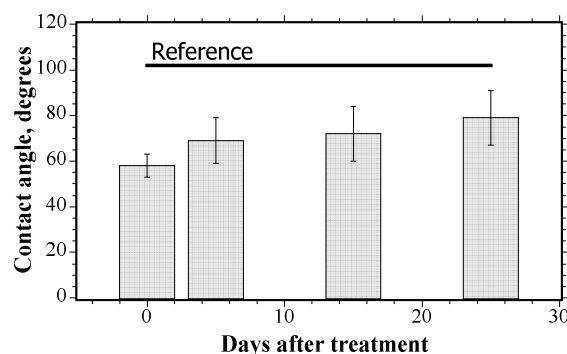
Figure 4. *Graph of aging effect on plasma treated PVC tubes.*

3. Results and discussion

Static contact angle measurements were performed on untreated and plasma-treated inner and outer surfaces of the polymer tubes by KRÜSS DSA30. Using the surface curvature corrections the results obtained for the outer and inner surfaces treated were practically the same. Figure 3 illustrates that the contact angles obtained for PTFE material were less than 90º and just slightly increasing on aging. Results obtained after treatment of PVC tubes are presented in figure 4. The contact angle values (Fig. 3) are close to those obtained by 40 s exposures of PTFE films by filamentary and glow dielectric barrier discharge in air and to those reached by an 20 min wet treatment with H_2O_2/H_2SO_4 (1:1) [14,15].

The emission spectra were recorded in the spectral range of 250 –750 nm. It was found that in the emission spectra of the discharge generated in air at atmospheric pressure and influenced only by water and water vapours one can identify the most intensive bands belongs to the second positive system of

For all three power values (3W, 6W, 9W) the rotational temperature was in the range 333K ± 5K. Also, rotational temperature was calculated from the line profile of OH ($A^2\Sigma^+$ - $X^2\Pi$, $\Delta\nu = 0$) rotational Q1 bandwith. Such peaks as 3/2, 5/2, 9/2, 11/2, 13/2 were used. Temperatures obtained have values of 480 ± 45K.

The measured vibrational temperature reaches values of about 2350K. The estimated error is about 320K

Conclusions

Obtained results show that the above described technique is viable and technically simple alternative to other plasma surface treatments of dielectric hollow bodies. Plasma temperature that was obtained by means of OES showed that this type of discharge could be used in treatement of temperature sensitive materials. PTFE and PVC material was successfully treated. The surface properties were changed from hydrophobic into hydrophilic. It was shown that the effect is noticeable even in a month after the treatment.

Reference

[1]   Park J, Henins I, Herrmann H W, Selwyn G S and Hicks R F 2001 Discharge phenomena of an atmospheric pressure radio-frequency capacitive plasma source *J. Appl. Phys.* **89** 20

[2]   Fridman a, Chirokov a and Gutsol a 2005 Non-thermal atmospheric pressure discharges *J. Phys. D. Appl. Phys.* **38** R1–24

[3]   Bárdos L and Baránková H 2010 Cold atmospheric plasma: Sources, processes, and applications *Thin Solid Films* **518** 6705–13

[4]   Liston E M, Martinu L and Wertheimer M R 1993 Plasma surface modification of polymers for improved adhesion: a critical review *J. Adhes. Sci. Technol.* **7** 1091–127

[5]   Roth J R 2001 *Industrial Plasma Engineering: Volume 2 - Applications to Nonthermal Plasma Processing* (CRC Press)

[6]   Kogelschatz U 2003 Dielectric-barrier Discharges : Their History , Discharge Physics , and Industrial Applications **23** 1–46

[7]   Wagner H-E, Brandenburg R, Kozlov K V, Sonnenfeld a., Michel P and Behnke J F 2003 The barrier discharge: basic properties and applications to surface treatment *Vacuum* **71** 417–36

[8]   Jiang B, Zheng J, Qiu S, Wu M, Zhang Q, Yan Z and Xue Q 2014 Review on electrical discharge plasma technology for wastewater remediation *Chem. Eng. J.* **236** 348–68

[9]   Joshi R P and Thagard S M 2013 Streamer-Like Electrical Discharges in Water: Part I. Fundamental Mechanisms *Plasma Chem. Plasma Process.* **33** 1–15

[10] Bruggeman P and Leys C 2009 Non-thermal plasmas in and in contact with liquids *J. Phys. D. Appl. Phys.* **42** 053001

[11] Brablec A., Slavicek P., Stahel P., Cizmar T., Trunec D., Simor M., Cernak M. 2002 Underwater pulse electrical diaphragm discharges for surface treatment of fibrous polymeric materials *Czech. J. Phys* **52** 491

[12] Nikiforov A Y and Leys C 2006 Surface Treatment of Cotton Yarn by Underwater Capillary Electrical

Discharge *Plasma Chem. Plasma Process.* **26** 415–23

[13]   Joshi R S, Friedrich J F and Wagner M H 2009 Study of carboxylic functionalization of polypropylene surface using the underwater plasma technique *Eur. Phys. J. D* **54** 249–58

[14]   Fang Z, Qiu Y and Luo Y 2003 Surface modification of polytetrafluoroethylene film using the atmospheric pressure glow discharge in air *J. Phys. D. Appl. Phys.* **36** 2980–5

[15]   Lohbach C, Bakowsky U, Kneuer C, Jahn D, Graeter T, Schafers H-J and Lehr C-M 2002 Wet chemical modification of PTFE implant surfaces with a specific cell adhesion molecule *Chem. Commun.* 2568–9

Parylene C and SiO$_x$ bilayers for archaeological artefacts preservation

J. Horak[1], M. Prochazka[1], L. Blahova[1], F. Krcma[1]

[1]Department of Physical Chemistry, Brno University of Technology, Brno (Czech Republic),
E-mail: xchorakj@fch.vutbr.cz

Parylene C is an auspicious material for metallic archaeological artefacts protection because of its good barrier properties and transparency. However its mechanical properties aren't sufficient especially against scratches. The aim of this paper is to give an overview about progress in treatment of metallic substrates using Parylene C layer and about an intention to increase its mechanical properties by a hardcoating layer.

1 Introduction

A lot of metallic archaeological materials is suffering because of an inappropriate protection and bad storage conditions in museums. That is why there is an intention to develop a procedure that will secure these objects better. For example, with protective barrier layers resistant to corrosion caused by vapours and fluids. There are several requirements that must be met. Material for those applications must be easily removable (e.g. for later analysis) and transparent (for later exhibition). Another requirement is that the procedure of deposition cannot harm the sample or its surface.

Based on our literature research poly-paraxylylene based film prepared by Chemical Vapour Deposition (CVD) [1] was selected. There are several types of poly-paraxylylene derivatives which are called the Parylenes [1,2]. Each of them has its unique properties. In our research dichloro-di-paraxylylene derivative was used. Its commercial name is Parylene C and it has good optical and dielectric properties as well as good barrier properties against vapours and gases. [3] Parylene C coating has been used for many interesting applications in an aggressive environment like film for neural electrodes [4], implantable sensors [5], drug delivery patches [6] or in bone fixation [3]. Parylene C has been used as a barrier film for some non-metallic artefacts, like silk [7], beetles, paper documents and others [8]. Unfortunately, Parylene C suffers from a few unwanted properties. First, there is a limited adhesion to the substrate. There are several approaches how to increase the adhesion [1,9,10] but, because of the requirement of easy removability, we are using special interface with controlled mechanical properties that allows us to get rid of the Parylene if it is needed. Then, although barrier properties of Parylene C are adequate, hardness and mechanical resistance of prepared layers are inadequate especially during manipulation. We tried to improve Parylene C mechanical properties by adding a hardcoating layer. Because of the transparency requirement and because the temperature of deposition should not be too high (cannot harm the sample), we chose SiO$_x$ layer prepared by Plasma Enhanced Chemical Vapour Deposition (PECVD) [11] as the most suitable solution. Because of different inorganic/organic character of both films, we used plasma pretreatment of Parylene C layer before the SiO$_x$ deposition. We did a few experiments that comprised multi bilayers.

2 Experimental

Bilayer and multi bilayer Parylene C-SiO$_x$ systems were made. Silicon wafers (SUMCO corp. C126-001, thickness 610-640 µm) were cleaned in ethanol, dried by pressure air and inserted into the apparatus for the Parylene CVD deposition. The same procedure was done for metallic (low alloyed steel) and polypropylene substrates.

Parylene C layer was formed from dichloro-di-paraxlylene. Whole process scheme with conditions is shown in Fig. 1. The thickness of prepared layers was controlled by dose of the precursor. Estimated thickness of prepared layers is 2 µm.
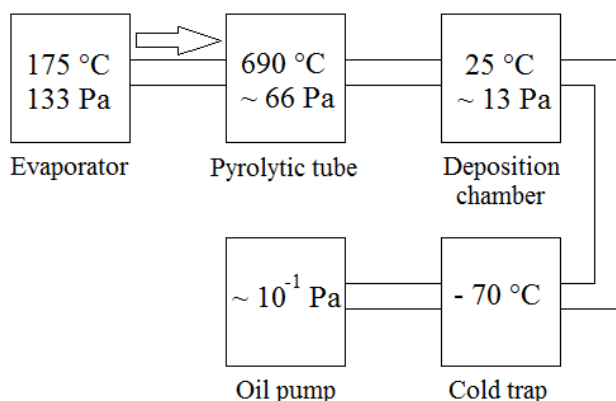
Fig.1: *Scheme of Parylene C deposition with conditions*

Directly after Parylene C film deposition, samples were transferred into the PECVD apparatus where samples were pretreated by argon plasma (2 minutes, 20 W, 10 sccm) followed by SiO$_x$ deposition from hexamethyldisiloxane (HMDSO) in oxygen atmosphere (20 minutes, 50 W, 0.5 sccm of HMDSO, 9.5 sccm O$_2$). PECVD deposition took place in capacitively coupled RF discharge in bell-jar type glass reactor with flow regime. Samples were attached to the upper electrode (both electrodes were made from stainless steel, 130 mm in diameter and in distance of 80 mm from each other). Scheme of the reactor is shown in Fig. 2.
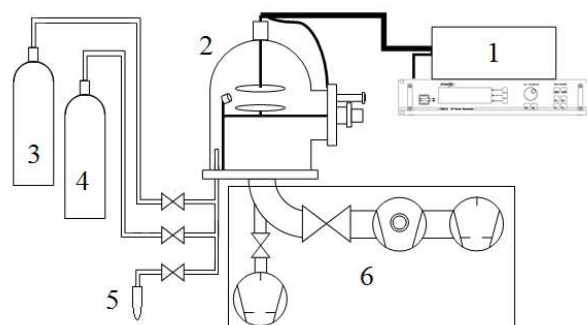
Fig.2: *Scheme of PECVD apparatus [12]: 1) RF generator (13.56 MHz) with impedance matching network; 2) Glass reactor; 3) Oxygen bottle; 4) Argon bottle; 5) Precursor reservoir; 6) Pumping system*

Following conditions of the experiments were done:

- Bilayer system – single deposition of one Parylene C and one SiO$_x$ layer
- Double bilayer system – deposition of Parylene C and SiO$_x$ bilayer repeated twice
- Triple bilayer system – deposition of Parylene C and SiO$_x$ bilayer repeated for three times

3 Results and discussion

3.1 Oxygen transmission rate (OTR)

In these measurements we measured the amount of oxygen that penetrates through examined material. In our case, it is a polypropylene (PP). Values measured for three prepared systems are shown in table 1.

	OTR (cm^3·m^{-2}·bar^{-1}·day^{-1})
Clean PP	1 320 ± 80
Parylene C	195 ± 3
Single bilayer	180 ± 1
Double bilayer	5 ± 2
Triple bilayer	38 ± 19

Tab. 1: Results of OTR measurements

We can see that there is noticeable decrease of the OTR for treated samples, for double bilayer especially. All multilayer systems have the same total thickness (2 µm). Best results were achieved for double bilayer system thanks to the "sponge effect". First Parylene C layer is saturated by immersing gas which decreases the transmission rate of the gas through the layer. Even better results would be achieved for the triple bilayer system. However, in our case single Parylene C layer was only 0.7 µm thick. This thickness is insufficient because the layer is not pin-hole free.

3.2   Nanoindentation
Nanoindentation was made for consideration of mechanical properties improvement. Only simple bilayer system was tested by this method till now. After comparison of nanoindentation for Parylene C itself and Parylene C + SiO_x layer it showed up that there wasn't any noticeable improvement in mechanical properties of examined system. On the contrary, it was found out that mechanical properties of this system are worse for the sample with SiO_x hardcoating layer.
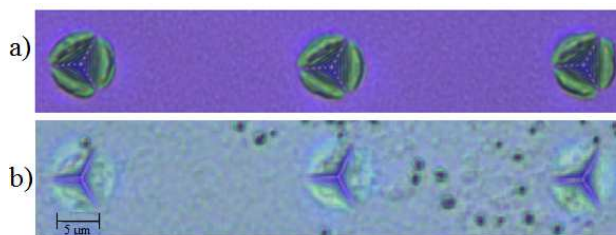
Fig. 3: *Comparision of the nanoindentation (0.5 mN load) for: a) Parylene C and b) Single bilayer*

It is visible that both indentations are similar. There is observable amount of extruded Parylene C around the injection sites. That is caused by the tip that penetrated through the SiO_x layer (Fig. 3). It seems that SiO_x layer in estimated thickness of 200 nm is not sufficient enough.

Nanoindentation measurements of other systems are scheduled and will be realized within a few months.

4 Conclusion
In this work we discussed the results of our intention to improve Parylene C barrier and mechanical properties by adding hardcoating layer in the system. According to the obtained data, we can say that multi bilayers can be used for improving system barrier properties but there is strong dependence of barrier properties on Parylene C thickness. Unfortunately, no improvement of mechanical properties of prepared multilayer was observed. However, plasma treatment has crucial influence on mechanical properties of prepared bilayer. Improvements in this way have already been proven. Therefore the following research will be focused on better understanding of processes that took place in plasma environment. Not only on SiO_x coating formation and ideal thickness formation but also on reactions that proceed on Parylene C layer.

5 Acknowledgment

6 References
[1] J. B. Fortin and T. Lu, Chemical vapour deposition polymerization: the growth and properties of parylene thin films, 1st edn (Kluwer Academic Publishers, New York, 2004.
[2] R. Sreenivasan and K.K. Gleason, *Chemical vapor deposition*, 15 (2009) 77-90.
[3] M. Cieślik, S. Zimowski, M. Gołda, K. Engvall, J. Pan, W. Rakowski and A. Kotarba, Materials Science and Engineering: C, 32 (2012), 2431-2435.

[4] X. Xie, L. Rieht, L. Williams, S. Negi, R. Bhandari, R. Caldwell, et al., Journal of Neural Engineering, 11 (2014), 026016.

[5] D. Zeniieh, L. Ledernez, G. Urban, *Procedia Engineering*, 87 (2014), 1398-1401.

[6] E.Pierstorff, R. Lam and D. Ho, Nanotechnology, 19 (2008), 445104.

[7] E.F. Hansen and W.S. Ginell, ACS Symposium Series, 410 (1989), 109-133.

[8] D. Sosna and J.S. Illingworth, Archeologicke rozhledy, 54 (2002), in Czech, 877-890.

[9] B. Arkles, Silane coupling agents connecting across boundaries, 2nd edn (Gelest, Inc., Morrisville, 2006)

[10] D. Zeniieh, A. Bajwa, L. Ledernez and G. Urban, Plasma Processes and Polymers, 10 (2013), 1081-1089.

[11] R. Wang, L.S. Li,J.Y. Gao and H.N.Cui, Advanced Materials Research, PTS1-2 (2011), 148-149.

[12] M. Prochazka, in 5th Central European Symposium on Plasma Chemistry – Book of Abstracts, Budapest, 2013, p. 198-199.

Observation of cathode voltage and discharge current oscillations and spoke behaviour in HiPIMS

P. Klein[1], J. Hnilica[1], Zdeněk Hubička[2], Martin Čada[2], P. Vašina[1],

[1]*Department of Physical Electronics, Masaryk University, Brno (Czech Republic), E-mail: pklein@mail.muni.cz*
[2]*Institute of Physics v. v. i., Academy of Science of the Czech Republic, Prague (Czech Republic)*

The oscillations were observed on cathode voltage and discharge current temporal evolution in HiPIMS pulse. The frequency of the oscillations depends at given pressure only on actual value of the discharge current. Rotation of the spokes over the cathode and the frequency of the oscillations shows different trends. The oscillations are observed at conditions where at least certain critical amount of spokes emerges.

1 Introduction

High Power Impulse Magnetron Sputtering (HiPIMS) is relatively new technique for depositing thin films [1]. It leads to the formation of dense plasmas with high fraction of ionized species and consequently higher ion flux towards substrate which enables to tailor specific properties of the deposited film [2]. In HiPIMS discharge the power is focused into short high energetic pulse followed by long off time. Recent observations using high speed imaging revealed that plasma is not homogenously distributed over the target surface, but it is concentrated in regions of ionization zones called spokes [3, 4]. Spokes are drifting in ExB direction [4]. Further observations differentiated ionization zone shapes into triangular or diffusive shape based on the target material [5]. Spokes emerge only for certain discharge current and certain pressure range [6]. The spoke rotation speed was evaluated around ~10 km/s [4]. Similar spoke rotation speed was obtained from oscillations on both floating potential of the probe and collimated optical signal [7]. A spoke model was developed too [8].

Apart from previously mentioned inhomogeneity, several observations of oscillations on both discharge current and cathode voltage were reported during the high current phase of HiPIMS pulse [9, 10]. Usually these oscillations were attributed as peculiar generator effect. Recently it was reported that such oscillations indicate the spoke formation [11]. Aim of this paper was to find out direct relation between spoke presence and oscillations on cathode voltage and discharge current.

2 Experimental setup

Alcatel SCM 650 magnetron sputtering system was used. 20 cm in diameter titanium target with purity 99,95% in balanced magnetic field was used as a sputter source. Argon supply with purity 99,999% was directed to the substrate area in the range 1-100 sccm. Pressure was measured by Baratron gauge as well as Pfeiffer Vacuum full range gauge. Background pressure was 10-3 Pa and working pressure was from 0,18 Pa to 5 Pa. Dual-channel Melec SIPP 2000 HiPIMS generator capable of pulse peak up to 500 A and up to 1000 V supplied the discharge with power. Voltages and currents were measured directly at the output of the Melec power supply. For advanced high frequency measurements calibrated current and voltage probe connected directly to the target was employed. Optical screening was

made by the ICCD camera PI-MAX 3 working in dual image mode which enables us to capture two snapshots in row with 3 μs between them. Exposure time was 100 ns. The pictures were later converted from greyscale by MATLAB Jet(72) scale colours.

3 Results

3.1 Cathode voltage and discharge current measurements

Fig. 1 showed typical example of cathode voltage and discharge current waveforms measured for 200 μs pulse length, 20 Hz repetition frequency and 1 Pa working pressure. Oscillations on both cathode voltage and discharge current were clearly visible and two different types of oscillations were identified. The first type of oscillation was at the beginning of the pulse and the second type of oscillation was present during high current pulse phase. First type of oscillation was dampened shortly after the beginning of the pulse. Amplitude of the cathode voltage of second type of oscillation was up to 500 V and amplitude of the discharge current of second type of oscillation was around 50 A.

Obtained signal from the probe was analysed by Fast Fourier transformation (FFT). Oscillations at the beginning of the pulse had frequency 500 kHz and oscillations during high current phase had frequency around 300 kHz. The oscillations at the beginning of the pulse were present for any experimental conditions. Even when generator was connected only to the 1 Ω resistor (to simulate load of the discharge) and the plasma was absent, the oscillations at the beginning of the pulse were still present. It excludes direct plasma action and indicates direct generator effect. When the generator was loaded by 1 Ω resistor no oscillations of the second type were observed during the high current phase even for currents reaching 400 A. It rule out generation of the oscillations by generator itself, they are observed only in the presence of plasma.
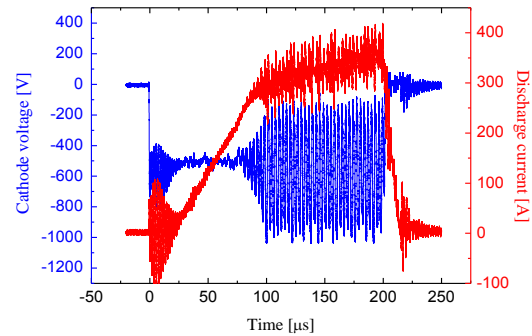
Fig. 1: *Cathode voltage and discharge current oscillations. Pulse length 200 μs, repetition frequency 20 Hz, pressure 1 Pa.*

The coil protecting the generator is an inductance part and the chamber and plasma is a capacity part of resonant LC circuit. Adding additional coil in series between the generator and the magnetron, the oscillations frequency changed only slightly however oscillations amplitude decreased significantly. The LC circuit is not a source of the oscillations, it is rather amplifier for oscillations originating in the plasma.

Periodic oscillations during high current phase were observed only for strict experimental conditions: pressure ranged from 0,3 to 2,0 Pa and discharge current higher than 225 A. For lower pressures only aperiodic oscillations were detected with much lower magnitude. No oscillations were present for the pressure overreaching 2 Pa.

Temporal evolutions of discharge current were recorded at argon pressure 1 Pa for different set of voltages. The frequency of the oscillations decreased as the discharge current evolved in time. Fig. 2 showed main frequency of oscillations as a function of actual discharge current. Data from measurements performed for different voltages were merged together. The frequency ranged from 280 kHz for to 375 kHz. For given pressure the frequency of oscillations depends on actual discharge current independently on the applied voltage. The increase of the discharge current led to

decrease of the oscillations frequency.

Pressure dependency of the oscillation frequency as a function of the actual discharge current is shown in Fig. 3. Again measurements with different set voltages were merged together. The decrease of the oscillation frequency with increase of the discharge current was proved in all studied pressure range. Increasing the pressure the oscillations frequency increased. For 2 Pa the oscillations frequencies changed only slightly. The maximum observed oscillations frequency reached 400 kHz for the 250 A at 2 Pa.
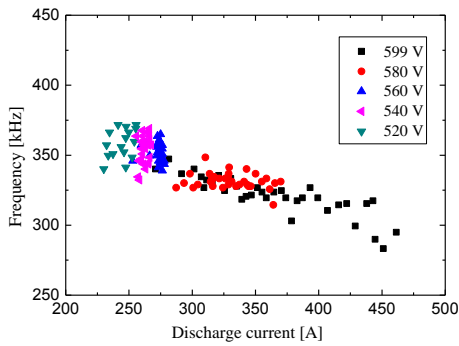
Fig. 2: *Frequency of oscillations as function of actual discharge current for different applied voltages and 1 Pa argon pressure.*
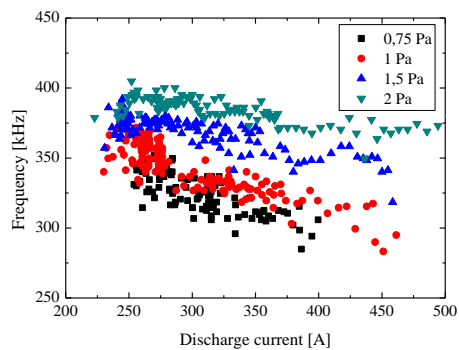
Fig. 3: *Frequency of oscillations as function actual discharge current for different Ar pressures.*

3.2 High-speed camera measurements

The spokes presence and their behaviour were studied by high-speed imaging. Fig. 4 showed typical snapshot of the spokes for different pressures attained at the same actual discharge current (400 A). The spoke appearance was strongly dependent on the pressure. At very low pressure (0,18 Pa), the triangular spoke shape was well recognized (see Fig. 4a). The shape became diffusive with increasing pressure (see Fig. 4b-c), overreaching 2 Pa there were no spokes recognizable (Fig. 4d).

The spokes were imaged for different pressures and different actual discharge currents. Two successive images were taken from the same pulse with time delay of 3 μs. Spoke rotation velocity and frequency was derived from the spoke image shift. The parameters in Table 1 (number of spokes, rotation velocity and spoke characteristic frequency) were determined as average values from series of twenty captured dual-images.

The spoke characteristic frequency was arbitrary determined as multiplication of number of spokes with rotation frequency. The rotation frequency was simply determined from rotation velocity and racetrack diameter (13 cm).

The number of spokes rose significantly with both increasing actual current and increasing pressure. For the lowest pressure (0.08 Pa) the number of spokes was constant for all actual current sets. The statistical error of spoke number was 1.

Rotation velocity significantly decreased with increasing pressure. The rotation velocity rose only slightly with increasing of the actual current. The rotation speed was in the range of 5-10 km/s. The statistical error of rotation velocity was around 500 km/s.

Spoke characteristic frequency was almost constant except the highest current and highest pressure cases. Spoke characteristic frequency is in the same order

of magnitude as observed oscillations on cathode voltage and discharge current, nevertheless they are not identical. Spoke characteristic frequency is 3-4 times lower than the frequency of the oscillations.
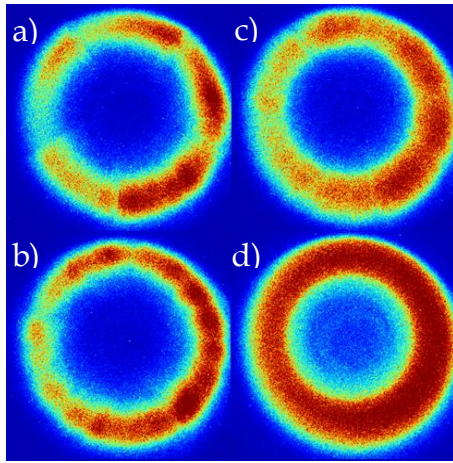
Fig. 4: *Target image for the same actual discharge current of 400 A at different working pressures a) 0,18 Pa,*
b) 1 Pa, c) 1,5 Pa and d) 2,5 Pa. Light intensity is represented in the false colour.

Table 1: *Influence of argon pressure and actual current on average number of spokes, average rotation velocity and characteristic spoke frequency.*

Pressure	Actual current	Number of spokes	Rotation velocity	Spoke characteristic frequency
[Pa]	[A]		[m/s]	[kHz]
0,08	262	5,2	8300	106
0,08	343	5,8	8300	118
0,08	491	5,5	9900	113
0,38	213	6,6	6600	106
0,38	338	7,2	6500	115
0,38	382	10	6800	167
0,50	274	6,1	5100	77
0,50	353	8,3	5700	118
0,50	441	12,1	6000	178

Trends of the evolution of quantities describing spokes are in agreement with other observations. Ehiasarian et al. [7] also observed lowering rotation velocity with increasing the pressure. Decrease of the rotation velocity was explained by more frequent collisions with residual gas at higher pressures. Increase of rotation frequency with actual discharge current growth was also observed by Winter et al. [12].
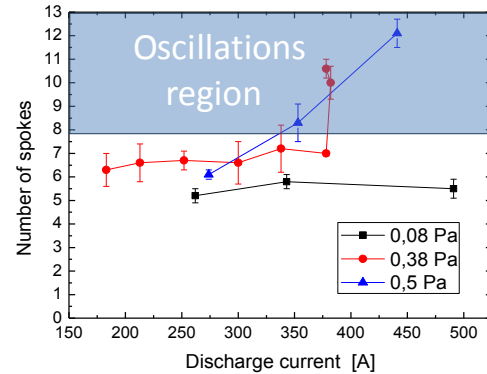
Fig. 5: *Average number of spokes as function of actual discharge current for different working pressures*

4 Discussion

For pressures higher than 2,0 Pa neither the spokes nor the oscillations on cathode voltage and discharge current are detected for the discharge currents in the studied range from 0 to 500 A. At the pressure range from 0,3 to 2,0 Pa, both the periodic oscillations and spokes were detected simultaneously for discharge current higher than 225 A. At lower currents, only spokes showed up. For lower pressures, only spokes are observed, but there are no periodical oscillations detected on cathode voltage and discharge current for discharge currents in the studied range from 0 to 500 A. Despite a broad range of experimental conditions scanned, no particular conditions to detect cathode voltage and discharge current oscillations at spoke absence were found out. Wherever the periodic oscillations on cathode voltage and discharge current were detected, they always accompanied spokes. However, the oscillations on cathode voltage and discharge

current are not a marker of the spoke presence as there exists wide range of conditions (particularly low pressures and low currents) where spokes were clearly identified at absence of the oscillations.

The oscillation frequency is determined in the range from 280 kHz to 400 kHz for the pressure between 0,75 Pa and 2 Pa. Spoke characteristic frequency ranges from 77 kHz to 178 kHz for the pressure from 0,18 Pa to 0,5 Pa. The spokes are well distinguished for chosen pressures. The oscillation frequency and the spoke characteristic frequency are in the same order of magnitude. Nevertheless, the oscillation frequency decreases with increasing discharge current but the spoke characteristic frequency rises. With increasing pressure both the oscillation frequency and the spoke characteristic frequency have rising trends. Dependency of the cathode voltage and discharge current oscillation frequency and spoke characteristic frequency on the discharge current shows opposite trends. The opposite behavior of the spoke characteristic frequency reflecting the spoke amount and motion and cathode voltage and discharge current oscillation frequency point out to no direct correlation between rotational motion of the spokes over magnetron cathode and the emergence of oscillations on cathode voltage and discharge current. This conclusion is in agreement with the observation of rotating spokes at the absence of oscillations on the cathode voltage and discharge current.

The Fig. 5 shows the average number of detected spokes as a function of actual discharge current for different working pressures. The region of the experimental conditions to detect oscillations on cathode voltage and discharge current is depicted, too. The oscillations on cathode voltage and discharge current are observed at conditions where at least 8 spokes emerge. We propose that oscillations on cathode voltage and

discharge current could be the result of spoke to spoke interaction. For the small number of spokes present (less than 8) the spokes are spatially separated and each spoke has enough space for propagation without significant interaction with neighboring spokes. For 8 and more spokes, the limited space over the magnetron cathode forces the spokes to interact with each other. We propose that this spoke to spoke interaction acts at a source of oscillations with certain characteristic oscillation spectrum. The certain oscillation frequency of this spectrum is then amplified by the resonance LC circuit and detected on the oscilloscope. At low pressures and low discharge currents, the amount of the spokes is below the limit value and the oscillations on cathode voltage and discharge current are not detected. At pressures higher than 2,0 Pa the spokes disappeared and consequently the oscillations on cathode voltage and discharge current are no more detected.

5 Conclusion

The periodic oscillations on cathode voltage and discharge current were observed for different experimental conditions. The generator as an oscillations source was ruled out. Increasing the pressure, the oscillations frequencies increased. Increasing actual discharge current the oscillations frequencies decreased.

High-speed camera imaging revealed the spokes present. The number of spokes increased with increasing pressure and discharge current. The rotation velocity increased with increasing discharge current but decreased with increasing pressure. The oscillation frequency and spoke characteristic frequency were in the range of a few 100 kHz, but they showed different trends.

Spoke to spoke interaction taking place at experimental conditions where the amount of the spokes exceed certain limit is

proposed to explain our observations.

6 Acknowledgment

7 References

[1] J. M. Schneider U. Helmersson, V. Kouznetsov, K. Maca, I. Petrov, Surf. Coat. Technol. 122, 290-293 (1999)

[2] A. P. Ehiasarian, W. D. Munz, L. Hultman, U. Helmersson, I. Petrov, Surf. Coat. Technol. 163–164 267 (2003)

[3] A. V. Kozyrev, N. S. Sochugov, K. V. Oskomov, A. N. Zakharov, A. N. Odivanova, Plasma Phys. Rep. 37, 621 (2011)

[4] A. Anders, J. Appl. Phys. 111, 053304 (2012)

[5] A. Hecimovic, M. Böke, J.Winter, J. Phys. D: Appl. Phys. 47, 102003 (2014)

[6] T. De Los Arcos, R. Schröder, Y. A. Gonzalvo, V. Schulz-von Der Gathen, J. Winter, Plasma Sources Sci. Technol. 23, 054008 (2014)

[7] A. P. Ehiasarian A. Hecimovic, T. De Los Arcos, R. New, V. Schulz-Von Der Gathen, M. Böke, J.Winter, Appl. Phys. Lett. 100, 1-5 (2012)

[8] N. Brenning, D. Lundin, T. Minea, C. Costin, C. Vitelaru, J. Phys. D: Appl. Phys. 46, 084005 (2013)

[9] R. Franz, C. Clavero, R. Bolat, R. Mendelsberg, A. Anders, Plasma Sources Sci. Technol. 23, 035001 (2014)

[10] S. Drache, V. Straňák, A. P. Herrendorf, M. Čada, Z. Hubička, M. Tichý, R. Hippler, Vacuum 90, 176-181 (2013)

[11] C. Maszl, W. Breilmann, J. Benedikt, A. von Keudell, J. Phys. D: Appl. Phys. 47, 224002 (2014)

[12] G. J .Winter, A. Hecimovic, T. De los Arcos, M. Böke, V. Schulz-von der Gathen, J. Phys. D: Appl. Phys. 46, 084007 (2013)

Luminescence study of alumina powders

T. Morávek[1], J. Ráheľ[1]

[1]*Masaryk University, Faculty of Science, Department of Physical Electronics, Kotlářská 2, Brno, Czech Republic*

Chemiluminescence of dielectric barrier discharge treated alumina powders could be used with advantage as an effective diagnostic method for determining the efficiency and aging of plasma treatment. However the deflection of detected signal from theoretical prediction suggests that other radiation mechanisms are participating on overall luminescence signal. Presented series of complementary experiments confirmed, that indeed chemiluminescence is the main process behind the observed light emission. Further radiation process associated with plasma treatment was identified as recombination-induced luminescence.

1 General introduction

Chemiluminescence accompanies certain types of exothermic chemical reactions, usually of oxidative nature. It is commonly used for the detection of traces of hydrogen peroxide [1] and monitoring the oxidation stability of polymers [2,3,4]. The measurements of chemiluminescence (CL) typically consists of heating the substrate (isothermally or with steadily increasing temperature) followed by the detection of spectrally unresolved light. This is presumably emitted from the substrate due to the oxidation processes involving the hydroperoxides decay [5,6]. However the measured isothermal luminescence curves do not fully agree with the proposed model in the whole range. The discrepancy is most pronounced in the decay phase, after the peak luminescene intensity has been reached [2,7]. The observation suggests that another process or even more processes are involved. Two additional processes besides CL are described in [8] for the luminescence of plasma treated polypropylene at ambient temperature: UV excitation of chromophores and a long lived recombination-induced luminescence (RIL). In good agreements with this, authors of [9] claim for the luminescence of epoxies at liquid nitrogen temperatures, that the light detected at later times of experiment is emitted by the process of recombination. Thermoluminescence (TL) caused by thermal detrapping of electrons accompanied by emission of light can also play an important role at sufficiently high temperatures. The TL phenomenon is frequently employed in dosimetric applications [10,11]. Therefore, if only the spectrally unresolved signal can be obtained, one has to be very careful in interpreting the results and the relative participation of CL, RIL or TL.

In our experiments we investigated the luminescence of sub-micron alumina powder treated in low-temperature coplanar dielectric barrier discharge [12]. The process of chemiluminescence associated with the presence of hydroperoxides on the powder surface was intended to be used as an indicator of the plasma treatment. A method capable of rapid assessment of plasma treatment for powders was sought, since the conventional methods based on sessile drop measurements are not well suited for particulate materials, and capillary rise Washburn method [13], requires at least several grams of powder for a single measurement. This can be a major drawback

when dealing with expensive powders, or when plasma treats at very slow rate due to its limited size or extremely large surface area of powders. On the other hand only tens of miligrams of powder are needed for the measurement of chemiluminescence. However as stated above the detected luminescence signal may comprise emission by other radiative processes besides CL. This paper presents our attempt to resolve the individual luminescence processes introduced to powder surface by dielectric barrier discharge plasma treatment.

2 Experimental
2.1 Plasma source

DCSBD (Diffuse Coplanar Surface Barrier Discharge) non-thermal plasma generator (Fig. 1) was used. It consisted of a screen-printed array of coplanar strip-like electrodes on the bottom side of a 96% purity Al2O3 plate with the thickness of 0.6 mm. 1.5 mm wide electrodes were separated by 1 mm gaps. The active plasma area of DCSBD unit was 8×20 cm2. The electrode was cooled by circulating transformer oil, which also provides an additional electrical insulation. The system was powered by 14 kHz sinusoidal high-voltage of up to 20 kV peak-to-peak amplitude. By increasing the driving voltage, a thin layer (about 0.3 mm) of low temperature non-equilibrium plasma consisting of H-shaped microdischarges emerges on the upper surface of the ceramic plate [12].
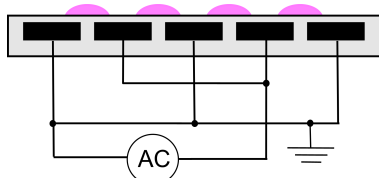
Figure 1 - Schematics of DCSBD setup. Only a reduced number of electrodes is shown for the sake of clarity.

2.2. Material

Plasma treatment was carried out on the sub-micron alumina powder Taimicron TM-DAR (Taimei Chemicals Co.,Ltd., 99.995% purity) with surface area of 13.7 m^2/g and primary particle size of 150 nm. Prior to the treatment, a small amount (approximately 1 g) of alumina powder was poured through a sieve on the surface of discharge ceramics (plasma area). The thin powder layer was covered with the shield glass plate. Alumina powder was treated in DCSBD operating in atmospheric pressure ambient air at input power of 400W for 1 minute.

2.3 Measurement

Luminescence experiments were performed on the photon-counting instrument Lumipol 3 manufactured by the Polymer Institute of Slovak Academy of Sciences, Bratislava, Slovakia. The measurements were done in a nitrogen flow of 25 mL/min. The weight of each sample was 80.0 ± 0.5 mg. The instrument dark count rate was $1 – 5$ counts/s at 50 °C, spectral range of instument was 290-630 nm.

3. Results

The shape of luminescence curve on Figure 2 clearly shows that indeed multiple processes are involved. Before the maximum is reached a shoulder appears, the origin of which had to be identified.
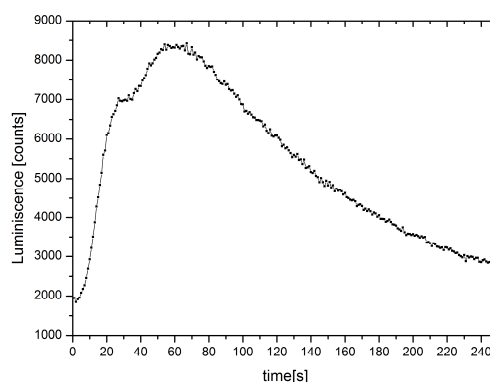
Figure 2 - Luminescence signal detected from plasma treated alumina powder (thermally cleaned at 600°C for 1 hour) in isothermal mode at 50°C.

Plasma treated alumina powders were left to age for a certain amount of time at ambient air, before investigated by chemiluminometer set to 120°C isothermal mode. The resulting curves are shown on Figure 3. It can be seen that as the peroxides (introduced to the surface by plasma treatment) decay during the aging process, the maximum of the curve decreases as well. Hence the dominant process present during the maximum can be assigned to the chemiluminescence, which is in good agreement with [8]. One can see, however, that even after 29 hours since plasma treatment, the effect of surface activation is still present.
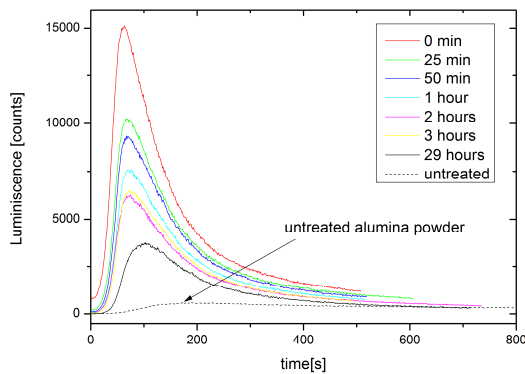
Figure 3 - Luminescence signal detected from plasma treated alumina powder in isothermal mode at 120°C for aging times 0 - 29 hours.

The more challenging part was to determine the process responsible for the shoulder appearance, which is most probably the same process responsible for the slower rate of luminescence decay. For this purpose we have performed a set of non-isothermal measurements for four distinct heat rates (2.5, 5, 10 and 20 °C/min). The resulting curves on Figure 4 exhibit maxima at different temperatures.
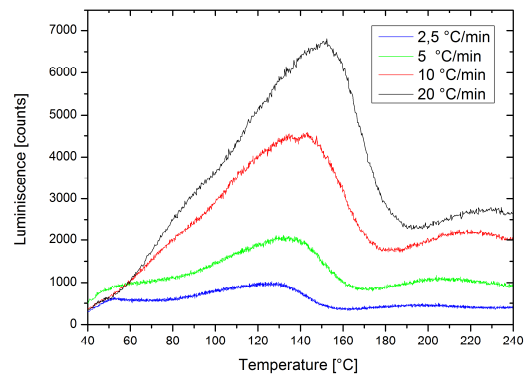
Figure. 4 - Luminescence signal detected from plasma treated alumina powder in non-isothermal mode for various rates of heating.

If the thermoluminescence was responsible, the maxima of the curves would be inherently independent of the rate of heating. According to the TL theory, the critical temperature depends only on the height of energy trap. In addition to that the minimum trap activation temperature reported for alumina TL is 390K [14]. In our case the luminescence signal was detected already at ambient temperature. These facts lead us to conclusion, that the process of TL can be excluded. The secondary process of light emission should be attributed to recombination-induced luminescence (RIL).

4. Conclusion

Luminescence measurements were performed on alumina powders treated by DCSBD. From the set of performed experiments it follows that the main processes contributing to the overall luminescence is the chemiluminescence, whereas the recombination induced luminescence starts to dominate in the later phases of the measurements. Participation of the thermoluminescence was excluded on the basis of non-isothermal experiments using various heating rates.

7. References

[1] A. Campbell, L. Kricka, P. Stanley, Bioluminescence and chemiluminescence, fundamentals and applied aspects. Chi-cester: John Wiley & Sons, (1994).

[2] P. Cerruti, C. Carfagnaa, J. Rychlý, L. Matisová -Rychlá, Polymer Degradation and Stability, 82, 477–485, (2003).

[3] P. Cerruti, M. Malinconico, J. Rychly, L. Matisova-Rychla, C. Carfagna, Polymer Degradation and Stability 94, 2095–2100, (2009).

[4] W. Camacho, S. Karlsson, Polymer Degradation and Stability, 78, 385–391, (2002).

[5] L. Matisova-Rychla , J. Rychly, M. Vavreková, European Polymer Journal, Volume 14, Issue 12, 1033–1037, (1978).

[6] L. Zlatkevich, Luminescence technique in solid state polymer research, New York, ISBN: 978-0824780456,93, (1989).

[7] L. Matisová -Rychlá, J. Rychlý, Polymer Degradation and Stability, 67, 515-525, (2000).

[8] M. Duran, F. Massines, G. Teyssedre, Ch. Laurent, Surface and Coatings Technology, 142-144, 743-747, (2001).

[9] Griseri et al., J. Phys. D: Appl. Phys., 34, 2534–2540, (2001).

[10] A.J.J. Bos, Radiation Measurements, 41, 45–56, (2007).

[11] M. Oberhofer, A. Scharmann, Applied thermoluminescence dosimetry, ISBN: 0-85274-544-3, (1981).

[12] Šimor et al., Applied Physics Letters, 81, 2716 (2002).

[13] T. Morávek et al., Open Chem., 13, 236-244, (2015).

[14] P.F. Ambrico et al., J. Phys. D: Appl. Phys. 43 (2010).

Functionalisation of electrospun polyamide nanofibres using atmosphreric microwave plasma jet

D. Pavliňák[1], J. Hnilica[1], M. Alberti[1], V. Kudrle[1]

[1]Department of Physical Electronics, Masaryk University, Brno (Czech Republic),
E-mail: d.pavlinak@mail.muni.cz

Polyamide (PA6) nanofibers prepared by electrospinning were treated using a microwave surface-wave plasma jet at the atmospheric pressure. The aim of this work was to induce the plasma-chemical modification of nanofibers without the damage of polymer bulk. For sample comparison, plasma treatment and heat air-flow treatment at the same temperature were carried out.

1 General introduction

In this study the microwave plasma jet is used to improve the surface properties of polyamide nanofibers. The aim of this work is to induce the plasma-chemical modification of nanofibers without the significant damage of polymer bulk. Newly acquired functional groups may have significant influence on the applicability of the improved nanofibrous material. For instance, good adhesion properties depend on appropriate surface free energy, which simultaneously corresponds to wettability and hydrophilic/hydrophobic behavior. Enhanced nanofibers may play the key role in the production of composites or in the grafting of biological active materials for tissue engineering. [1-8]

The influence of the plasma discharge on electrospun polyamide-6 nanofibers is studied here. The optimization properties of nanofibrous materials and especially sintered nanofiber mats with controlled pore size for given application were in the focus of interest. A microwave atmospheric plasma jet (surfatron) operated in Ar and Ar+O_2 gas mixtures was chosen as an experimental plasma source. To distinguish plasma induced and heat-induced changes, a control sample treated by hot air-flow gun at similar temperature was carried out, as well. [4, 8]

2 Results and discussion

2.1 Experimental set-up

The plasma was carried out from commercial SAIREM Surfatron 80 with integrated matching unit. The microwaves were fed from the magnetron generator (SAIREM GMP 20 KED) to the surface wave launcher via a wave-guide, a ferrite circulator and a coaxial cable. The microwave generator (2.45 GHz) operated in continuous mode with power 150 W. The reflected microwave power was adjusted below 10 W.

During the plasma treatment, the PA6 nanofibers were fixed on a planar substrate holder and placed 0.7 cm under the end of the plasma discharge, i.e. 15 mm from the end of the capillary. The motorized holder was moving at 12 mm/s.

The effect of the plasma treatment was compared to exclusively thermal treatment by an air-flow heat gun. The temperature of air-ow was set to 300° C and treatment time was 60 s.

2.2 Diagnostic techniques

- Scanning electron microscopy (SEM) was carried out by Tescan MIRA3. In order to achieve better resolution, the samples were coated by 30nm gold layer. For better visualization, SEM images were coloring.

- Infrared spectroscopy was measured in evacuated attenuated total reflectance (ATR-FTIR) mode by Bruker Vertex 80V spectrometer using a diamond crystal. Spectral range was set from 4000 to 600 cm^{-1} with the spectral resolution of4 cm^{-1}. Each spectrum consists of 100 scans. The spectra were evaluated by Bruker OPUS software (version 6.5) using "rubber-band" baseline correction.

2.3 SEM imaging of samples treated by Ar and Ar+O$_2$ plasma

Electrospun polyamide nanofibers were plasma-chemically treated using microwave discharge in pure argon or argon with 2% oxygen admixture. After the plasma treatment, the sintering of nanofibers was observed (see Fig. 1). Samples treated by pure argon plasma are shown on the top, the nanofibres treated by argon with oxygen admixture plasma are on the bottom. The number of successive treatments increases from left to right and is shown in the lower left corner of each image.
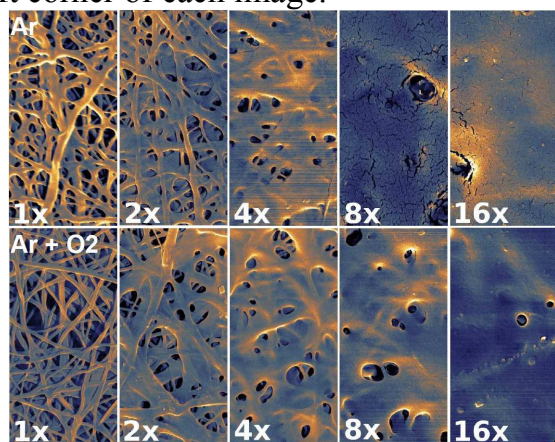
Fig. 1: *SEM images of the PA6 nanofibers for experiment with the increasing number of plasma treatment repetitions. Firstly published in [4].*

As expected, the degree of sintering increases with the number of treatments for both plasma gas com- positions. The results of plasma discharge in argon and argon + oxygen are the nearly the same, despite the high oxygen reactivity. This could be explained by a discharge inhibiting effect due to increased electron attachment to oxygen.

In the following experiment the effect of plasma-induced sintering was compared to purely thermal treatment. In Fig. 2 are shown the images of thermal effect on the nanofiber mat treated by a heat gun. The image 2(a) shows the sintered surface at the side facing the heat gun. Small particles on the image are probably the dust blown by the heat gun.
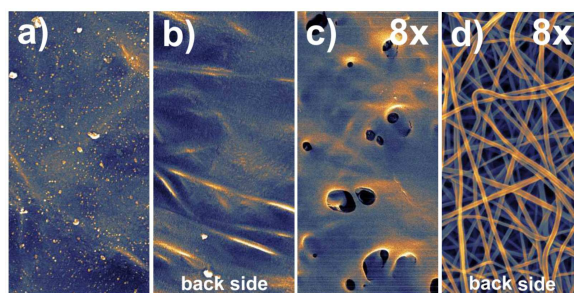
Fig. 2: *SEM images of the PA6 fibers after different treatments. (a) heat gun treated mat - front side, (b) heat gun treated mat - back side, (c) 8x plasma treated (Ar+2%O2) mat - front side and (d) 8x plasma treated (Ar+2%O2) mat - back side. Firstly published in [4].*

The back side of the same sample image 2(b) shows similar sintered nanofibers but without visible dust particles. The temperature conditions of the sample treated by plasma discharge (images c and d) were also around 300°C [4]. The images of the front 2(c) and back 2(d) side demonstrate that plasma treatment causes sintering only at the side facing the plasma discharge. Sintering process does not penetrate deeper to its interior. This is in stark contrast with the thermal treatment, during which the heat gun fused the nanofibers in the entire volume.

2.4 SEM imaging of samples treated by Ar and Ar+O₂ plasma

The infrared spectra of nanofibers for the increasing number of repetitions are shown in Fig. 3. The measured spectrum of non-treated nanofibers revealed a good qualitative agreement with the reference of PA6. Essentially, two distinct phenomena were described by ATR-FTIR spectroscopy.

The first one is observable in the enlarged part of region (C4) 1650-1785 cm^{-1}. This part can be interpreted as a polymer oxidation process. Most likely it describes the increased abundance of carbonyl groups (C=O). The broadening of absorption peak to an interval with the central position at 1733 cm^{-1} is caused by the various positions of carbonyl groups in the polymer structure. [4]

Fig. 2: *Typical overview ATR-FTIR spectra of the electrospun PA6 nanofibers for different plasma treatment repetitions with. In upper corner is magnified area for carbonyl absorption bands. Firstly published in [4].*

The structural transitions of the polymer are reflected by another effect in region B1. The tendency to the increase of absorption band at 690 cm^{-1} during the plasma treatment repetitions can be explained as a transition process from the thermodynamically unstable γ-form to more stable α-form. While the first effect is present exclusively after the plasma treatment, the second effect is common for both plasma and thermal treatment of the polymer mats. [4]

3 Conclusion

- While the plasma treatment caused the sintering of polyamide nanofibers only onto the facing surface, the heat treatment sintered the PA6 mats in whole volume.
- The ATR-FTIR confirmed the significant increase of oxidation products on the polymer surface. However, the fibrous PA6 material treated with heat air-flow gun did not exhibit any oxidative changes.
- The increasing time of treatment raised the level of surface oxidation. As was predicted, the maximum oxidation effects were higher in the of Ar+O₂ plasma treatment that in the case of pure Ar plasma discharge.

3 Acknowledgment

4 References

[1]   R. Neppalli, C. Marega, A. Marigo, M. P. Bajgai, H. Y. Kim, and V. Causin. Poly(e-caprolactone) filled with electrospun nylon fibres: A model for a facile composite fabrication. European Polymer Journal, 46(5), (2010).

[2]   Ch. Xu, F. Xu, B. Wang, and T. J. Lu. Electrospinning of poly(ethylene-co-vinyl alcohol) nanofibres encapsulated with Ag nanoparticles for skin wound healing. Journal of Nanomaterials, 3, (2011).

[3]   Y.K. Wang, T. Yong, and S. Ramakrishna. Nanofibres and their influence on cells for tissue regeneration. Australian Journal of Chemistry, 2005.

[4]   D. Pavlinak, J. Hnilica, A. Quade, J. Schafer, M. Alberti, and V. Kudrle. Functionalisation and pore size control of electrospun PA6 nanofibres using a microwave jet plasma. Polymer Degradation and Stability, 108:48(55), (2014).

[5]   A. Manakhov, D. Nečas, J. Čechal, D. Pavliňák, M. Eliáš, L. Zajíčková, Deposition of stable amine coating onto polycaprolactone nanofibers by low pressure cyclopropylamine plasma polymerization. Thin Solid Films, 581, 30, (2015).

[6]   Pavliňák, D., Švachová, V., Vojtek, L., Zarzycká, J., Hyršl, P., Alberti, M., & Vojtová, L. Plasma-chemical modifications of cellulose for biomedical applications. Open Chemistry, 13(1), (2015).

[7]   Pavliňák, D. and Galmiz, O. and Zemánek, M. and Brablec, A. and Čech, J. and Černák, M. Permanent hydrophilization of outer and inner surfaces of polytetrafluoroethylene tubes using ambient air plasma generated by surface dielectric barrier discharges. Applied Physics Letters, 105, 154102, (2014).

[8]   Pavliňák, D. Ph.D. thesis Plasma-chemical modifications of polymeric materials. Masaryk University, (2015).

Phase synchronized ICCD imaging of power modulated microwave plasma jet at atmospheric pressure

L. Potočňáková[1], J. Voráč[1], P. Synek[1, 2], J. Hnilica[1] and V. Kudrle[1]

[1]*Department of Physical Electronics, Masaryk University, Brno (Czech Republic), E-mail: nanai@mail.muni.cz*
[2]*The Central European Institute of Technology (CEITEC), Masaryk University, Kamenice 5, CZ-62500, Brno, Czech Republic*

In this paper, spatially resolved and phase synchronized optical diagnostics of power modulated microwave plasma jet operating at atmospheric pressure is described. The overall plasma effluent appearance and flow dynamics were found to be strongly influenced by the modulation frequency, mostly through the formation of a vortex at the boundary of expanding hot plasma channel and cold surrounding atmosphere.

1 Introduction

Atmospheric pressure plasma jets are well known and suitable for many applications [1]. They are often operated in pulsed or modulated regime, which can provide further advantages over continuous wave regime. Particularly, it is the ability to achieve higher active particle density at the same mean excitation power or significantly lower thermal loading of the substrate for the same treatment rate. These effects can be attributed to a non-linear relation between the supplied power, electron temperature and gas temperature. In our previous studies [2, 3], we demonstrated the application potential of microwave plasma jet with power modulated by sinusoidal wave.

The pulsed and modulated discharges are of great interest also for the fundamental plasma physics research, as they represent a suitable experimental tool for the study of the plasma kinetics [4, 5]. In this work we used optical examination of modulated discharge to study the non-stationary gas flow phenomena and the distribution of excited species in the discharge and its vicinity.

2 Experimental setup

The experimental setup can be seen in Fig. 1. As a plasma source, the atmospheric pressure microwave plasma jet - surfatron [6] - was used. The plasma was excited inside the fused silica discharge tube (2 mm inner diameter, 4 mm outer one) in argon with 2600 ppm(v) of water vapour by the surface wave propagating along the interface between the plasma and the dielectric tube wall. As for other discharges with surface wave, also the surfatron plasma exhibits typical elongated plasma form with slow decrease of the plasma density towards the discharge tube end. The discharge tube was open into outer atmosphere, where the plasma effluent mixed with air and where a possible material treatment would take place. This plasma plume was the main focus of our attention in this research.

Power to the surfatron was supplied

by microwave (2.45 GHz) generator in amplitude modulated (AM) mode, for which sinusoidal envelope (modulation frequencies 90 Hz and 1710 Hz, 150 W in minimum and 300 W in maximum) was used. The discharge was observed by ICCD camera, either directly (covering UV-VIS-NIR range) or through suitable bandpass filters. For phase synchronized measurements, the camera was triggered by the function generator used for modulation of the power generator.
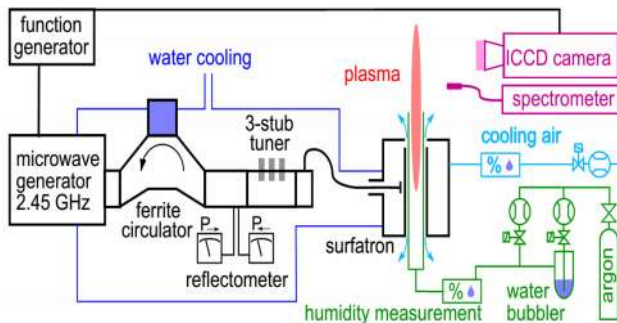
Fig. 1: *Schematic drawing of the experimental set-up.*

3 Results

In Fig. 2, the time averaged (200 single shots of 10 μs each) image of the discharge at (a) 90 Hz and (c) 1710 Hz can be seen. The trigger delay was set to observe the discharge in the rising part of the sinusoidal modulation period. Comparing the images for the two frequencies, several features can be discussed. While the plasma effluent at lower AM frequency has rather regular shape of a plume, a transient vortex [7] is formed for higher frequency. The temporal instability, i.e. fluctuation of the discharge is visualized in Fig. 2 (b) and (d) through the relative standard deviation. The lower part of the discharge part (close to the tube exit, where the gas flow is laminar) is quite stable for both frequencies. For 90 Hz, the deviations are

mostly present only around the very end of the discharge, but for 1710 Hz they appear to be significant in the whole area from the vortex structure to the plasma jet tip.
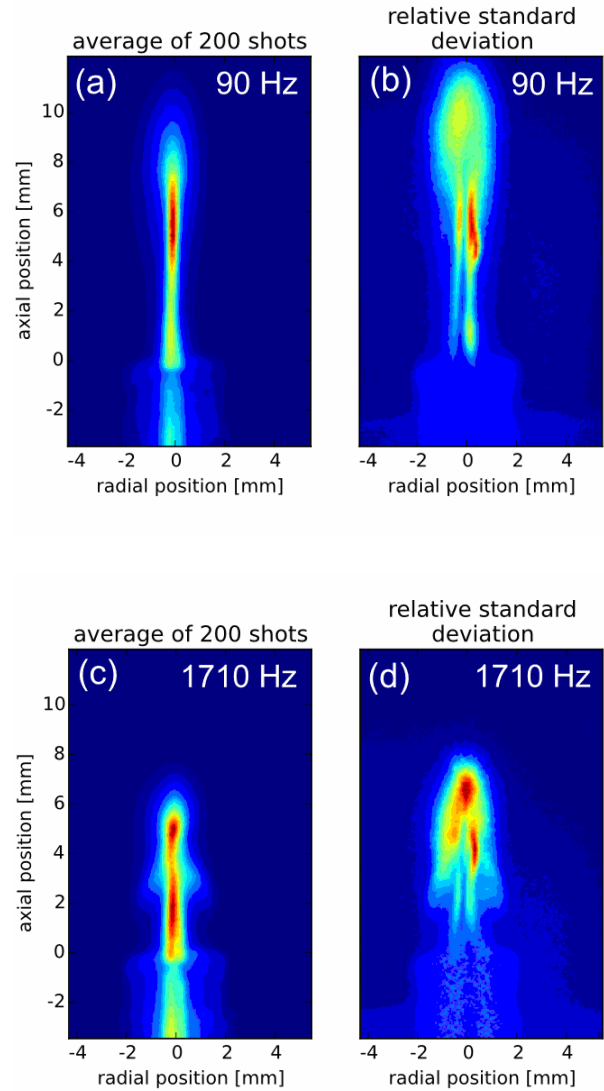
Fig. 2: *The time averaged images of the discharge during the rising slope of sinusoidal AM modulation at (a) 90 Hz and (c) 1710 Hz and corresponding relative standard deviations ((b) and (d)).*

The absence/presence of the vortex and its development can be recognized also in Fig. 3. In Fig. 3 (a) and (c), there is an axially resolved time evolution of laterally integrated intensity of the discharge. For both frequencies, the length of the

discharge follows the sinusoidal modulation, but even though the power setting was the same for both AM frequencies, the discharge was longer for 90 Hz, especially in the power minimum. The emission is not axially homogeneous as local emission maximum can be observed in the effluent. It is best visible during the decreasing power (i.e. decreasing length of the discharge) at 90 Hz while for 1710 Hz it happens when the discharge elongates. In Fig. 3 (b) and (d), the width of the discharge is shown. For 90 Hz, no unexpected evolution can be found – the discharge is the widest at the end, where it is more turbulent. For 1710 Hz, the movement of the vortex is clearly recognizable in the Fig. 3 (d) as the narrow strip of locally widened discharge channel. It starts shortly after the minimum elongation of the discharge and can be traced up to the turbulent tip of the discharge.
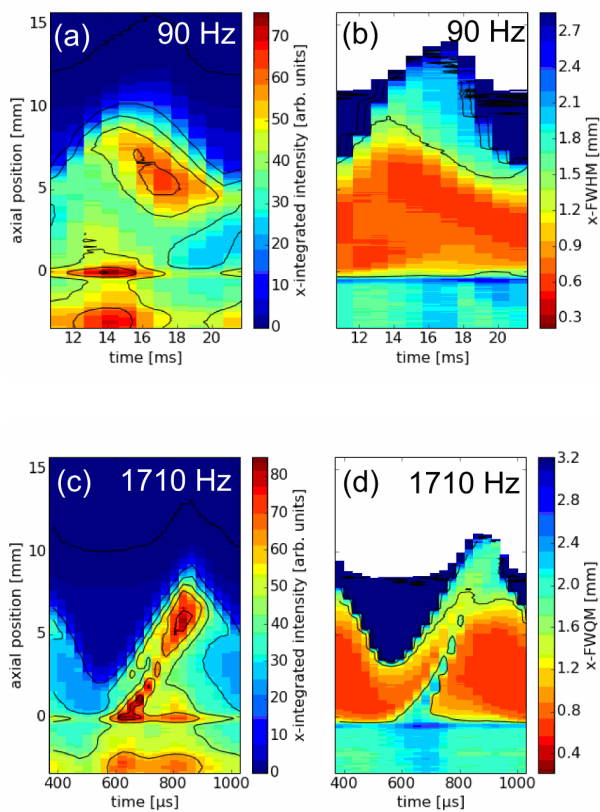
Fig. 3: *(a) and (c) - axially resolved time evolution of laterally integrated intensity of the discharge for one period of sinusoidal modulation at 90 Hz and 1710 Hz and (b) and (d) - corresponding full width of the discharge at quarter maximum of its intensity.*

Using various bandpass spectral filters, it was found out that the vortex is emitting the strongest at wavelengths around 307 nm corresponding to the OH radical. Although there was a water vapour intentionally added into argon, this result suggests that the vortex is probably formed due to interaction of the discharge with the surrounding air atmosphere. As it was not observed for 90 Hz, the vortex presumably originates in faster gas heating during the steeper rising slope of the AM envelope at 1710 Hz. The friction between the rapidly accelerating hot plasma and cold environment would then result in the annular vortex encircling the plasma channel.

The increased rate of air mixed into the argon discharge in the presence of the vortex might be one of the reasons, why the stronger quenching and shortening of the discharge was observed for higher AM frequency. On the other hand, such effect might be advantageous for higher efficiency of the surface plasma treatment by pulsed or modulated discharges. Thanks to the vortex, more airborne reactive species such as OH or NOx radicals, crucial for various kinds of treatment, can be produced. In case of plasma deposition, where some precursor is deliberately admixed into the discharge, the existence of vortex causes more turbulent behaviour, better mixing and better homogeneity, which might be strongly beneficial, too.

4 Conclusion

Atmospheric pressure microwave plasma jet with sinusoidal power modulation at

two modulation frequencies was studied by means of the phase synchronized ICCD camera imaging. The discharge was found to have a different shape and length for different modulation frequencies and in different modulation phases. The main distinction between the AM frequencies was the formation of transient vortex for higher frequency. The vortex probably originates in the friction between rapidly expanding hot plasma channel during the rising modulation slope and the cold surrounding environment. The presence of the vortex negatively influences the plasma itself but might be very useful for applications, where mixing of plasma with air or precursors is needed.

5 Acknowledgement

6 References

[1] M. Laroussi, T. Akan, *Plasma Processes and Polymers* **4** (2007) 9

[2] L. Potočňáková, J. Hnilica, V. Kudrle, *International Journal of Adhesion and Adhesives* **45** (2013)

[3] J. Hnilica, L. Potočňáková, M. Stupavská, V. Kudrle, *Applied Surface Science* **288** (2014)

[4] St. Behle, A Brockhaus, J Engemann, *Plasma Sources Science and Technology* **9** (2000) 1

[5] N. Britun, T. Godfroid, S. Konstantinidis, R. Snyders *Applied Physics Letters* **94** (2011) 14

[6] M. Moisan, C. Beaudry, P. Leprince, *Physical Letters A* **50** (1974)

[7] S. Zhang, A. Sobota, E.M. van Veldhuizen, P.J. Bruggeman, *J. Phys. D:Appl. Phys.* **48** (2015)

Striated Patterns in Coplanar Barrier Discharge

J. Ráheľ, J. Čech, T. Morávek

Masaryk University - CEPLANT, Kotlářská 2, 611 37 Brno, Czech Republic, E-mail: ra-hel@maul.muni.cz

Atmospheric pressure rare gases of helium, neon and argon were investigated by means of high speed ICCD camera for the presence of striated structures in single pair strips geometry of coplanar dielectric barrier discharge. In helium stratification occurs over the instantaneous anode. In neon two distinct regimes of striation were observed – spatially stable diffuse over the anode, and unstable filamentary over the interelectrode gap and anode. In argon only the filamentary striation regime was observed.

1 Introduction

Deposition of surface charge on insulating barrier is a key phenomenon responsible for short duration of breakdown event in dielectric barrier discharge (DBD) and hence its highly non-isothermal character. Further phenomena associated with the surface charge are lowering the breakdown voltage of DBD [1], re-appearance of discharge microfilaments at the same spot [2], falling slope breakdown of pulsed DBD [3] or the formation of stratified discharge structures (striations) at coplanar geometry arrangement [4]. The later phenomenon was studied intensively in relation to discharge physics in pixels of plasma display panels (PDP). Owing to that, the research was focused mainly on Ne and Xe gases or their mixtures at reduced pressures up to 500 Torr [5,6]. The role of surface charge played in the coplanar DBD striation process was elucidated mainly by the numerical modelling [6,7]. Striations are formed sequentially after the initial breakdown as discharge electrons are depositing over the anode. Resulting distortion of electric field above the anode causes its local reduction ("well-like field" [8]) which, and similarly to the phenomena of Faraday dark space, lowers the intensity of light emission. Numerical simulations of Lee *et al.* [9] showed that the striation is substantially more pronounced when the particle-in-cell code instead of 2-dimensional fluid model is employed. This result suggests an important role of non-local electron kinetics in the striation onset. The key role of non-local electron kinetics was confirmed further by [7], but the charge accumulated over the anode still remains to be the necessary condition for striation onset.

Our motivation to study of the striation effect comes from our interest in addressing the lack of knowledge on the role of residual positive charge being left on the anode dielectric from the previous half-cycle. To measure the weak optical signal associated with its presence (e.g. charge recombination), some of the single photon counting methods has to be employed. For this however, it is important to achieve a high spatio-temporal stability of observed event, which may be compromised if the anode striations are present. We have made therefore high speed ICCD camera recordings for our atmospheric pressure discharge arrangement for three different rare gases – helium, neon and argon.

2 Experimental setup

Two co-planar metal electrodes, forming rectangular electrode gap of 4.65 mm width and 20 mm length, were immersed into insulation oil and covered by 96% Al_2O_3 with the thickness of 0.635 mm. The electrodes were housed in a plastic gas-tight chamber, continuously flown with the working gas.

Helium and neon with purity of 5.0 and technical purity argon were used. For experiments with argon, higher spatial stability of breakdown microfilament was achieved by replacing one of straight electrodes with a sharp one, with 45° angular dimension of its vertex. The discharge was driven at the frequency of 9.4 kHz taken from the function generator (Agilent 33220A), with the voltage amplitude varying from 1.2 to 4 kV.

Phase resolved images of discharge were captured using PI-MAX3 ICCD camera (Princeton Instruments). The camera comprises: an interline CCD detector with 1024×1024 pixels resolution coupled by fibre-optic to optical signal intensifier capable of the gate time down to 3 ns @ 1 MHz repetition rate. The intensifier has spectral sensitivity from 180 to 920 nm (SR photocathode) and a fast P46 phosphor. For the VIS spectral range imaging the camera was mounted with SIGMA lens (105 mm 1:2.8 DG MACRO EX) with true 1:1 macro capability. For the UV-VIS spectral range imaging the camera was mounted with CoastalOpt. lens (105 mm f/4 UV-MICRO-APO) with 1:2 macro capability. Optical resolution enhancement of approx. 2× was adopted optionally using the Soligor C/D7 AF TELECONVERTER 2× in the VIS spectral range or Soligor Extension Tube (12+20+36 mm) in the UV-VIS spectral range.

The phase-locked discharge imaging was realized with the external clock signal delivered from the function generator used for driving the high-voltage generator.

3 Results and discussion

We have observed striation effect in all investigated gases. In helium and neon it was possible to achieve highly stable discharge structures. This allowed us to employ the image accumulation function to improve the time resolution of recorded breakdown development.

The view on critical moments in discharge formation of helium and neon are shown in Fig. 1 and Fig. 2 respectively. Both discharges are diffuse in appearance, free of any narrow microfilaments. The uniform appearance along the vertical axis is a welcomed feature for our intended application of time-correlated single photon counting (TCSPC) measurements of weak optical spectra, for it will prevent the rise of signal artefacts due to the random appearance of microfilaments.

In helium (Fig. 1) initial Townsend phase of discharge formation resulted in formation of luminous layer along the anode edge at the time of t_0. After that, transition to the glow discharge occurs, with the wide ionization front propagating towards the cathode region. Due to the coplanar geometry the uniform ionization front is allowed to freely propagate along the dielectric surface above the cathode. In helium the cathode-directed ionization front can propagate up to the walls of our discharge chamber without losing its uniform appearance. Electrons originating from the ionization front are pulled to electric field towards the anode, where they are allowed to freely propagate as well. Nevertheless, behind the primary anode ionization front, an interplay between the local electric field and electron energy distribution function causes a gradual rise and decay of stationary luminous belts, which we have identified as the anode striations.

In neon (Fig. 2) similar discharge formation scenario takes place, although at approximately two times longer time scale. The striations formed at anode region exhibit a much finer structure and are larger in number. As the discharge decays, formed anode striations are fading radially outward from the center of electrode.
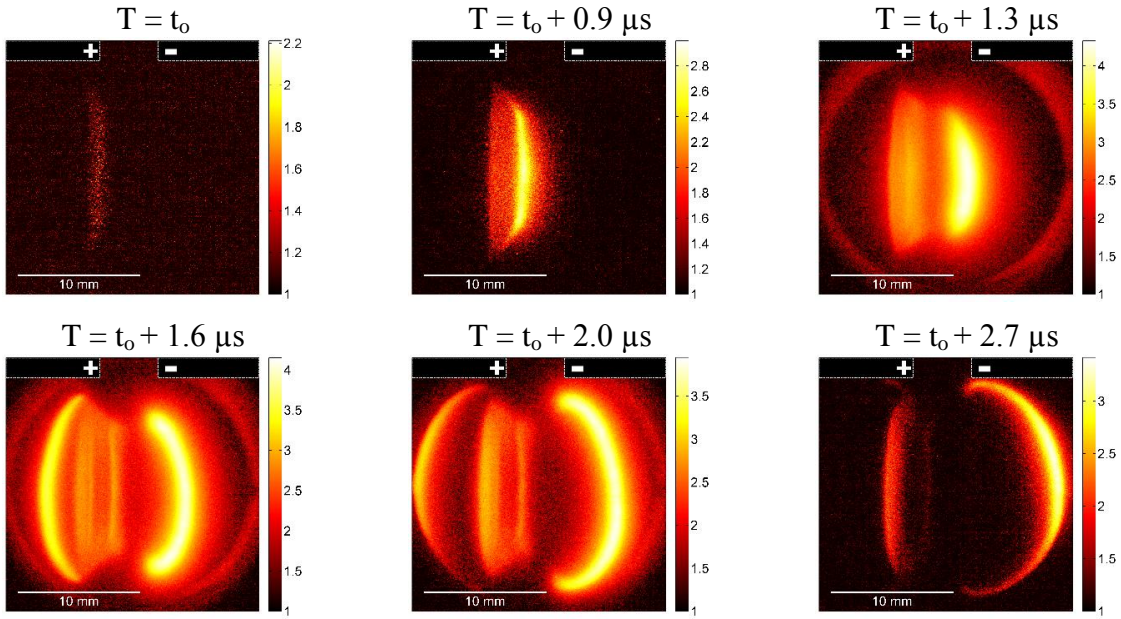
Fig. 1: ICCD record of helium breakdown and striation formation. Exposure time 50 ns. Accumulation of 500.
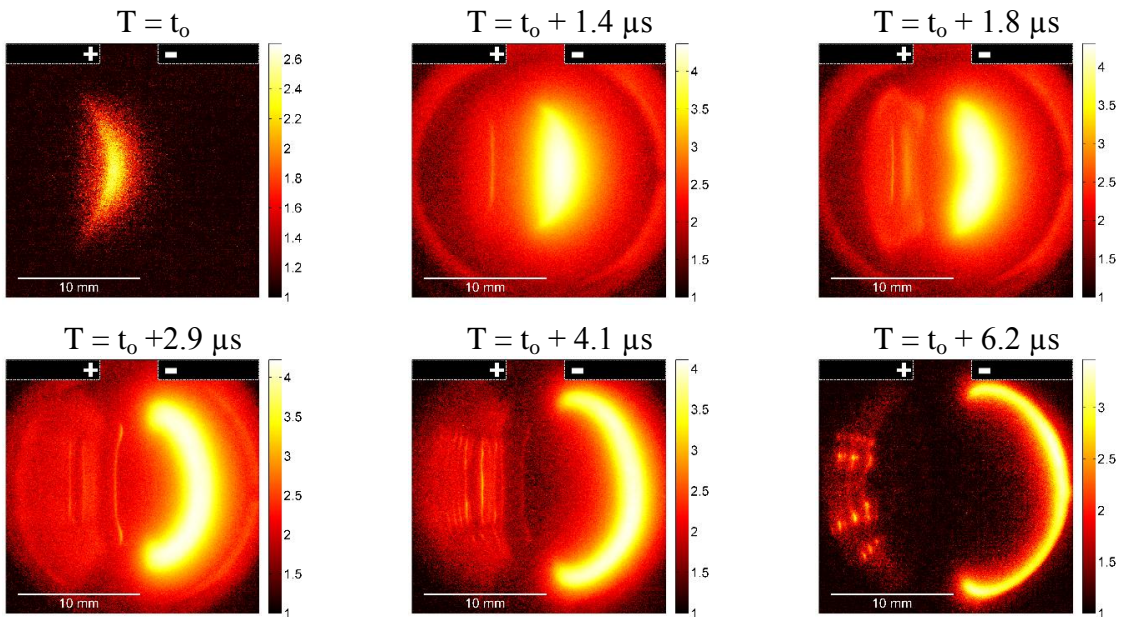
Fig. 2: ICCD record of neon breakdown and striation formation. Exposure time 100 ns. Accumulation of 200.

The stability of discharge structures on ICCD images allowed us to simulate TCSPC signal along the horizontal axis for both gases. Results presented in the form of 2D graphs in Fig. 3a and Fig. 3b for helium and neon respectively, allows the reader to get a better insight into the striation formation dynamics. More importantly, in our future work with TCSPC it allows to distinguish the striation originated anomalies in observed accumulated optical signal above the anode region.

In neon, by increasing the applied voltage above some critical value (2.8 kV in our case) we were able to achieve the transition into the filamentary regime. Multiple

(a)   (b)
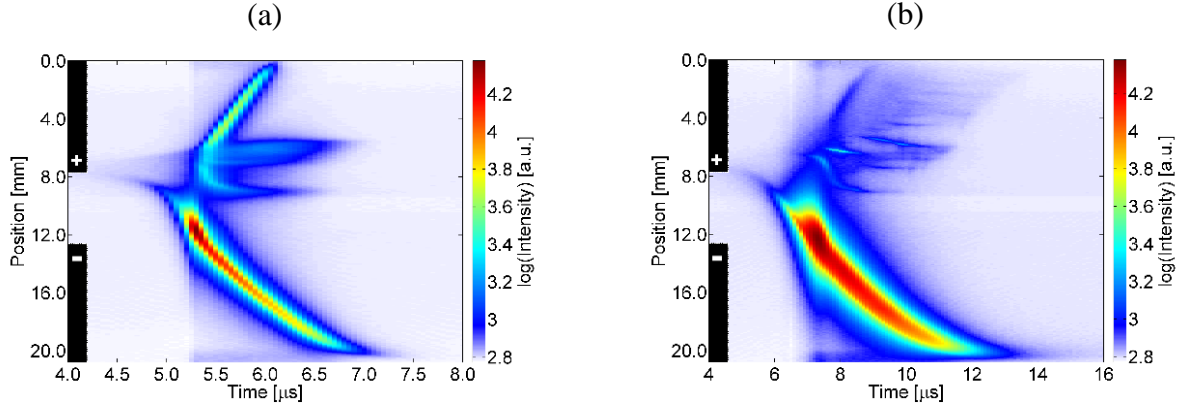
Fig. 3: Simulated TCSPC signal from ICCD images for: (a) helium; (b) neon.

(a)   (b)   (c)
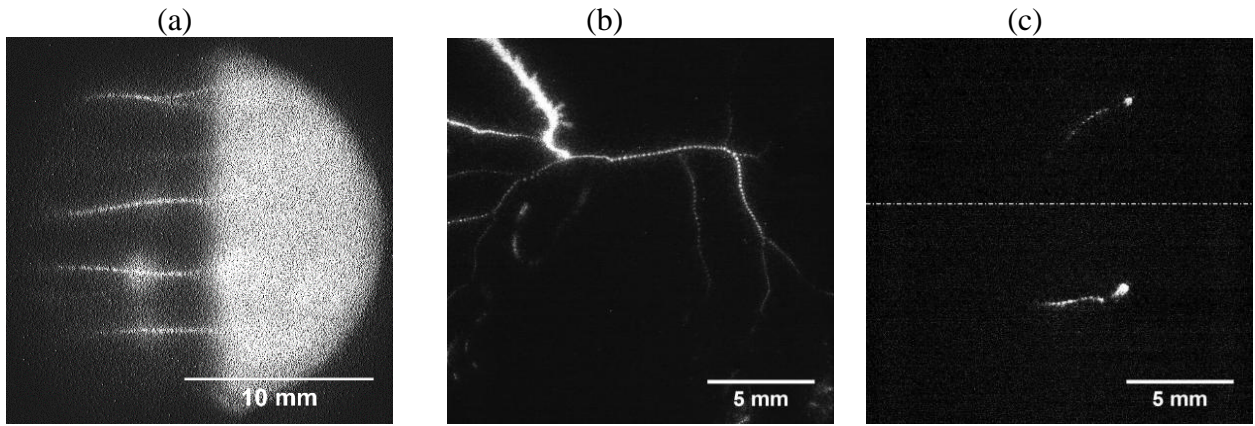
Fig. 4: (a) Jellyfish like structures of filamentary discharge in neon over single half period; (b) Striations in argon microfilaments – 100 ns exposure time; (c) Striation formation in argon – 3 ns exposure time.

microfilaments are formed above the anode and inter-electrode space within the same half period. Nevertheless visual appearance of discharge above the cathode remains diffuse. Resulting discharge structure similar to jellyfish is shown in Fig. 4a. Interestingly enough the new appeared microfilaments exhibit a striated structure as well. Unfortunately, due to the random appearance of discharge microfilaments, we could not have obtained a more time-resolved view on dynamics of striation formation.

Similar stratification of discharge microfilament has been reported recently for volume DBD at atmospheric pressure argon [10]. We have therefore tested also argon in our coplanar set-up. Unlike in neon, we were able to stabilize only filamentary regime.

Nevertheless, all microfilaments revealed a striated pattern, when the exposure time bellow 100 ns has been used, which suggests the presence of moving striations (Fig. 4b). In some cases stationary striations were observed as well. To get some better insight into the striation formation dynamics we have made some ultra-short exposure times images intended to record only the first moments of striation being formed. We have found that the striation is formed immediately after the ionization front is formed above the cathode and begin to propagate (Fig. 4c). This sequence of events is essentially the same as for diffuse regime observed for helium and neon.

4 Conclusion

The use of high speed ICCD camera to investigate formation dynamics of atmospheric pressure rare gases breakdown at coplanar electrode arrangements confirmed the existence of striation effect. Presented observations suggest that the striations, especially moving striations, are a quite common phenomenon in coplanar DBD in both diffuse and filamentary operation regime.

References

[1] N. Gherardi, and F. Massines: IEEE Trans. Plasma Sci. 29, 3 (2001), 536.

[2] Y. Akishev, G. Aponin, et al.: Plasma Sources Sci. Technol. 20, 2 (2011), 024005.

[3] M. Kettlitz, H. Höft, et al.: J. Phys. D: Appl. Phys. 45, 24 (2012), 245201.

[4] Cho, G et al.: J. Appl. Phys. 87, 9 (2000), 4113.

[5] R. Ganter, J. Ouyang et al.: J. Appl. Phys. 91, 3(2002), 992.

[6] S. Feng, F. He, and J. Ouyang: Chin. Phys. Lett. 24, 8 (2007), 2304.

[7] F. Iza, S. S. Yang, et al.: J. Appl. Phys. 98 (2005), 043302.

[8] J. Ouyang, F. He, et al.: Physics Letters A 360 (2007), 619.

[9] J. K. Lee, S. Dastgeer et al.: Jpn. J. Appl. Phys. 40 (2001), L 528.

[10] T. Hoder, et al.: Phys. Rev. E 84, 4 (2009), 046404.

INVESTIGATION OF DIFFUSE HELIUM COPLANAR BARRIER DISCHARGE BY SINGLE PHOTON COUNTING

Jozef Ráheľ, Tomáš Morávek, Zdeněk Navrátil, Jan Čech

Department of Physical Electronics, Masaryk University, Brno (Czech Republic), E-mail: rahel@mail.muni.cz

Atmospheric pressure discharges are prone to streamer breakdown, which leads to their filamentation. Homogeneous discharges can be generated in helium, neon and nitrogen in volume configuration of electrodes. However the use of coplanar configuration typically leads to a filamentary discharge. We report observation of a stable homogeneous discharge in coplanar configuration in helium. Spatio-temporally resolved profile of electrical field was calculated from the intensity ratio of He lines. The intensity distributions of the lines were measured using Time-Correlated Single Photon Counting. The results show two cathode and anode-directed ionizing waves with origin above the anode.

1 Introduction

Dielectric Barrier Discharges (DBD) are widely used for generation of atmospheric non-equilibrium plasma. They are usually observed in filamentary mode, with multiple microfilaments bridging the gap between the electrodes covered by dielectric barrier. In inert gases or for special geometries DBDs can be generated in a diffuse mode. These discharges are referred to as Atmospheric Pressure Glow Discharges (APGD) and due to their properties, they offer unique possibilities in the areas where homogenity is required. This prompted the study of APGD by many research groups, which discovered its existence in various gas mixtures [1-3], obtained spatio-temporaly resolved images of the discharge [4,5], and clarified the physical processes leading to the formation of APGD [1,5,6]. These works focused on the volume configuration of DBD. In this work we present our results on TCSPC (Time-Correlated Single Photon Counting) study on coplanar barrier discharge in helium at atmospheric pressure. By varying the parameters of a discharge in coplanar configuration, we managed to obtain a stable filament-free mode. Spatio-temporal emission patterns of several spectral lines (706.5 nm, 667.8 nm and 728.1 nm) were recorded. The ratio of intensities of spectral lines 667.8 nm and 728.1 nm can be used to estimate the reduced electric field in the discharge [7]. In this paper spatio-temporally resolved distribution of the ratio $R_{667/728}$ is presented, which qualitatively represents the distribution of the reduced electric field strength in the discharge.

2 Experimental

Presented measurements were carried out in a coplanar electrode configuration described in [8]. The metal electrodes with rectangular electrode gap of 4.65 mm, immersed into oil and covered with alumina dielectric, were placed into a small chamber equipped with a quartz window for discharge diagnostics. Helium with purity 5.0 was flowing through the chamber at flow rate of 555 sccm. The discharge was driven by an AC voltage of frequency 9.4 kHz, generated with function generator (Agilent 33220A) and amplified to a high voltage signal with amplitude of 1.6 kV. The applied voltage and the discharge current were measured by a digital oscilloscope (LeCroyWaveRunner 6100A). The discharge current was inferred from a

voltage measured on a 3 kΩ resistor, connected in series with the electrodes.

The light coming out of the discharge was first monochromatized (Jobin Yvon HR-640) and then analyzed by single photon counter (Becker-Hickl SPC-150) equipped with photomultiplier working in photon counting mode (PMC-100-4). A time-resolution of 0.2 μs was achieved by synchronization of the photon counter with the voltage signal. A spatial resolution of 0.1 mm was obtained by projecting the discharge by a quartz lens onto a movable slit, with optical fibre located beyond it. Using the TCSPC following emission lines were measured: 706.5 nm, 667.8 nm and 728.1 nm. The pictures of the discharge were taken by digital camera Casio EXILIM F1.

3 Results

Figure 1 shows a typical oscillogram for He discharge. It can be seen that only one current peak per half period is recorded without any additional microdischarge pulses. The absence of any bright microfilaments can be also seen in Figure 2, showing the image of the discharge taken with digital camera. Figure 3, Figure 4 and Figure 5 show the intensity distributions of three He lines. Intensity distributions of all helium lines investigated in this study exhibited similar behaviour, described in detail in the following paragraph.

At first, a low intensity builds up near the anode. This pre-breakdown phase is attributed to the initial Townsend avalanching. After that a strong ionizing wave is started and propagates towards the cathode. At the same time a second less intense ionisation wave heading to the anode appears. It can be seen that the maximum intensity for triplet line 706 nm appears sooner than for the singlet lines 667 nm and 728 nm. Triplet states can be populated by

stepwise excitation through metastables, efficient also at low electric field [7]. On the other hand the upper states of singlet transitions are populated from the ground state. Hence higher field strength is required.
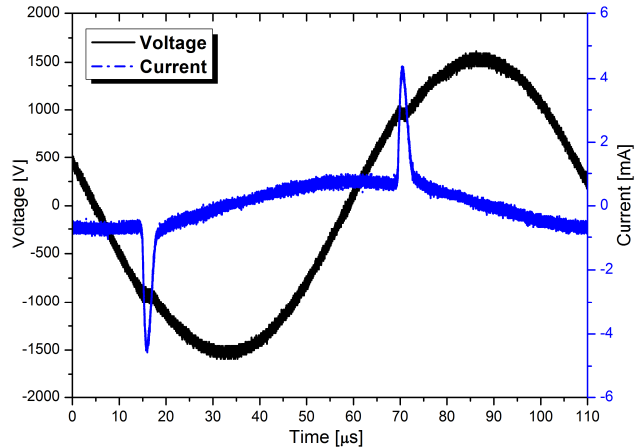
Fig. 1: *Evolution of the current and applied voltage in the diffuse APGD discharge in He.*
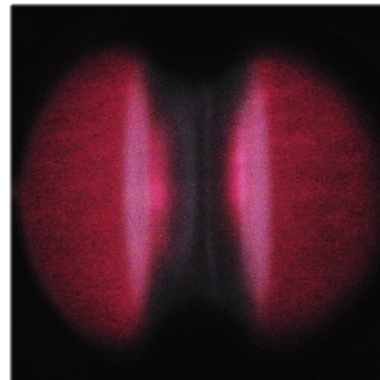
Fig. 2: *The visual appearence of the filament-free discharge in He. Exposure time was 1/6s..*

This expectation is supported by Figure 6, which shows the ratio of intensities of spectral lines 667.8 nm and 728.1 nm. It can be seen that the maximum of the ratio $R_{667/728}(E/N)$ occurs about 1.5 μs after the maximum of 706 nm line. The intensity distribution of $R_{667/728}(E/N)$ also shows two ionizing waves started between the electrodes heading for anode and cathode. The black areas represent the spatio-temporal

coordinates, where the intensity was weak and the ratio could lead to misleading results.

Fig. 3: *Spatio-temporally resolved intensity distribution of 706.5nm He line for 4.65mm interelectrode gap. The positions of cathode and anode are denoted by letters C and A, respectively.*

Fig. 4: *Spatio-temporally resolved intensity distribution of 667.8 nm He line for 4.65mm interelectrode gap.*

the anode and cathode side of our experimental set-up.

Fig. 5: *Spatio-temporally resolved intensity distribution of 728.1 nm He line for 4.65mm interelectrode gap.*
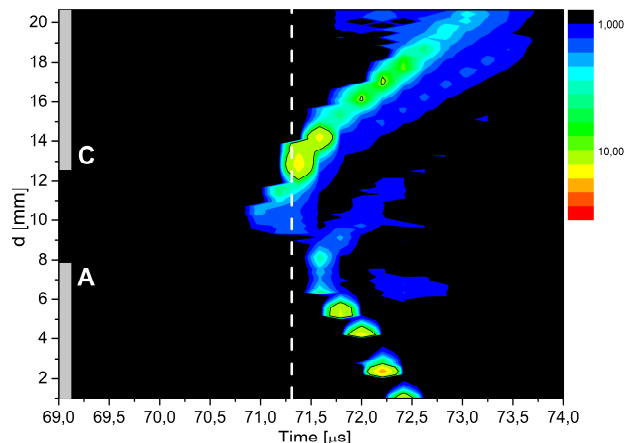
Fig. 6 *Spatio-temporally resolved ratio of intensity distributions $R_{667/728}(E/N)$ for He lines 667.8 nm and 728.1 nm.*

4 Conclusion

In this work a stable filament-free discharge with coplanar configuration of electrodes in helium was investigated. Using the TCSPC a spatio-temporal spectroscopy was performed on three helium lines. From the ratio of intensities of 667.8 nm and 728.1 nm helium spectral lines the relative development of electric field was calculated. The $R_{667/728}$ (E/N) ratio exhibits two maxima heading for

4 References

[1] F. Massines et al., J. Appl. Phys., 83 (1998)

[2] D. Trunec et al., J. Phys. D: Appl. Phys., 34 (2001)

[3] N. Gherardi et al., Plasma Sources Sci. Technol., 9 (2000)

[4] Ricard et al., Surf. Coat. Technol., 112 (1999)

[5] K. Kozlov et al., J. Phys. D: Appl. Phys., 38 (2005)

[6] I. Radu et al., J. Phys. D: Appl. Phys., 37 (2004)

[7] S.S. Ivkovic et al., J. Phys. D: Appl. Phys., 47 (2014)

[8] J. Čech et al., The European Physical Journal D, 54 (2009)

Interaction of atmospheric pressure plasma and silicon surface

D. Skácelová[1] , J. Čech[1] , M. Černák[1,2]

[1]*Department of Physical Electronics, Masaryk University, Kotlářská 2, 611 37, Brno (Czech Republic), E-mail: skacelova@mail.muni.cz*
[2]*Department of Experimental Physics, Faculty of Mathematics, Physics and Informatics, Comenius University, Mlynska dolina F2, 842 48, Bratislava (Slovak Republic)*

The aim of this work is to study the characterization of plasma-surface interaction of silicon in DCSBD plasma. The influence of the plasma, generated in ambient air on the silicon surface properties with respect to the filamentary nature of DCSBD was studied. Surface properties and chemical composition of silicon were studied by SEM and EDX, respectively. The experimental data were successfully supported by the modeling.

1 Introduction

Low temperature plasma technology is finding applications in many industrial areas [1, 2] and provides a good innovation for the future. Unfortunately, the standard operational mode of the atmospheric pressure DBDs is filamentary, leading to strong spatial non-uniformity and affecting the quality of the treated surface.

In this research, we have studied the interaction of silicon wafer surface and atmospheric pressure plasma generated by Diffuse Coplanar Surface Barrier Discharge (DCSBD) [3-6]. DCSBD represents dielectric barrier discharge in coplanar geometry operating in ambient air at atmospheric pressure. Due to the geometry, DCSBD produces the large area of thin layer of non-equilibrium cold plasma on the surface of the dielectric barrier with high density of active particles. Such geometry and properties provide many options for fast discharge surface modification (e.g. cleaning, activation) of various materials, especially for large flat surfaces such as wood, nonwoven textile, glass etc. [6, 7].

In our previous articles we discussed activation, cleaning and oxidation process of silicon wafers [8, 9]. It was proven that plasma treatment of Si in DCSBD can efficiently clean carbon impurities in a short time, activate the Si surface due to the adsorption of hydrophilic radicals on the surface [8], as well as, DCSBD technique enables create thin SiO2 film [9]. However, understanding of the phenomena associated with plasma-surface interaction is still the subject of scientific discussion.

The aim of this work was to study the interaction of Si sample surface and DCSBD plasma during plasma modification. Surface modifications and the chemical changes of Si were studied by scanning electron microscopy and energy dispersive X-ray spectroscopy. The simulation described in this work demonstrated the behavior of electric field during plasma treatment and approximately reflects the microscopic processes observed during plasma – surface interaction.

2 Experimental

The plasma was generated at atmospheric pressure by DCSBD. The DCSBD geometry consists of many parallel silver electrodes embedded in Al2O3 ceramics, see Fig. 1a). The discharge was powered by a high frequency voltage (14 kHz, 14 kV peak to

peak). The treatment has been carried out in ambient air at the discharge power of 300 W. The treated samples were placed at fix position in the plasma layer. The distance between the sample and the ceramics plate was 0.3 mm. Before plasma treatment all samples were cleaned by isopropyl alcohol and dried with flow of air.

The surface morphology of the Si surface was determined using SEM (TESCAN Mira 3) equipped with a Schottky Field Emission electron gun, secondary electron detector and back-scattered electron detector. Both detectors are also located in the objective lens. Maximal resolution is 1.0 nm by 30 kV. Additional equipment are electron beam induced current (EBIC), Energy Dispersive X-ray Spectroscopy (EDX) and Wavelength Dispersive Spectroscopy (WDS) detectors (Oxford instruments) and low vacuum mode with chamber pressure up to 500 Pa.

The simulations were carried out using COMSOL Multiphysics simulation software. The simple 2D model of DCSBD electrode was used to determine the static electric field in the plasma gap (see Fig. 1b). The Electrostatic module of COMSOL was adopted using FEM (Finite Elements Method). The influence of the presence of treated material (silicon wafer, silica glass) on the electric field distribution was studied (see Fig. 2).

3 Results

The electric field distribution simulation serves as an approximation of microscopic processes observed during plasma – surface interaction. In the presence of plasma, the situation becomes more complicated. Plasma equalizes the differences in electric field distribution: it increases the weak electric field while reducing the strong electric field. Despite this fact the simulation of the electric field distribution can reveal the background of plasma - surface processes and interactions partially.

The vectors of electric field intensity were calculated on the free triangular mesh by the FEM refined in the vicinity of plasma gap. Figure 1b) shows the distribution of static electric field surrounding DCSBD generated in ambient air. The colors of the map and the length of the arrows are proportional to the logarithm of electric field $(\log |\bar{E}|)$. The arrow direction represents the direction of electric field vector.

The electric field maximum occupies a small area above the corners of powered electrodes embedded in ceramic. The electric field in the ceramic is non-uniform, its maximum is observed between electrodes and its minimum is directly upward the electrodes. However, the electric field generated above the dielectric in the plasma area is uniformly distributed and its intensity is proportional to the distance from the
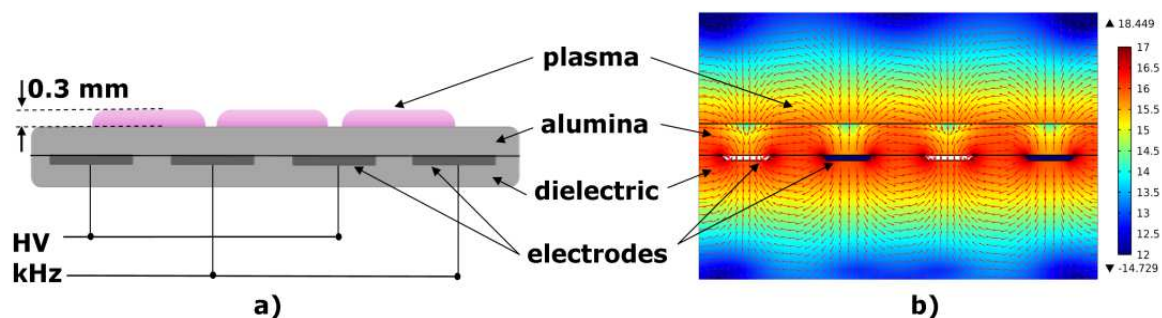
Fig. 1: *a) The cross-section of an electrode system. b) 2D distribution of static electric field at 14 kV surrounding DCSBD electrode.*

surface. The model describes well the reality: the DCSBD consists of numerous H-shaped elementary discharges developing in the area of the highest electric field and running randomly along the electrodes creating the homogeneous uniform plasma layer on the ceramic surface [4, 5].

The presence of the treated sample changes the distribution of the electric field and these changes depend mainly on the material.

Figure 2 shows the distribution of electric field in the ceramic, plasma gap and in the treated sample during the plasma treatment. Effect of two materials was simulated: silicon with relative permittivity of ε_r = 11.7 and silica glass with relative permittivity of ε_r = 2.09. The thickness of the plasma layer in air is approx. 0.3 mm [5]. Therefore, the optimal plasma gap in model was fixed at 0.3 mm.

Evidently, the silica glass placed in the plasma slightly influences the distribution of the electric field in the plasma gap. On the other hand, silicon placed in the plasma changes the distribution of electric field in plasma gap considerably. The field is reduced in the area between the electrodes and strongly intensified above the electrodes, i.e. in the plasma gap between the electrode and Si sample. Apparently, the presence of the material with higher dielectric constant in plasma leads to the deflection of the electric field and according to the simulation, plasma would be preferentially generated between the electrodes and Si. Thus, diffuse coplanar surface discharge converts into the volume DBD. This hypothesis fully corresponds with the experimental data discussed below.

Figure 3 shows the Si surface after 10 minutes plasma treatment and related chemical composition. The modification of the silicon surface exposed to the DCSBD plasma consists of the formation of regular strip-like structure accordant with the structure of embedded electrodes.
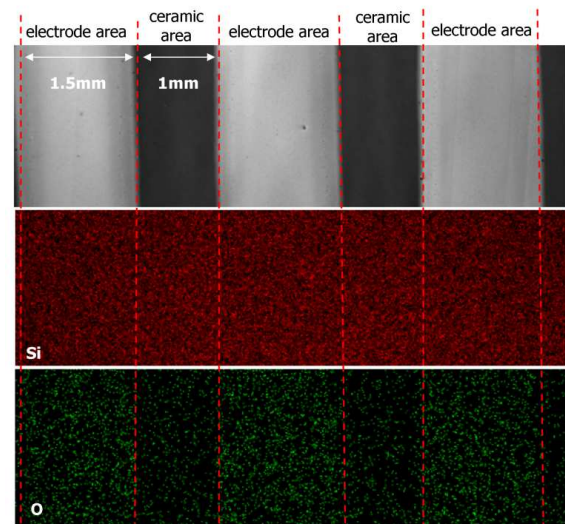
Fig. 3: *The modified silicon surface after 10 minutes plasma treatment and related chemical composition. The regular strip-like structure observed by SEM and Si and O distribution.*
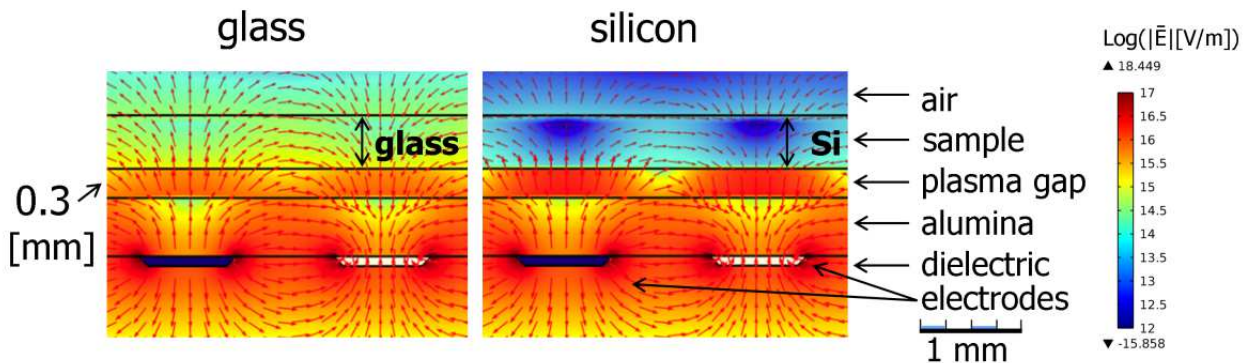
Fig. 2: Comsol model of electric field distribution at 14 kV during the treatment of glass and silicon.

Experimental results correlate with the model. The effect of plasma is dominant in the electrode area, the effect of plasma on the silicon surface between the electrodes (noted as ceramic area in Figure 3) is negligible. Moreover, in comparison with the model, plasma boundaries are explicit and finely defined. This variance is given by the model assumptions and simplifications.

The chemical composition was obtained by EDX at 5kV accelerated voltage corresponding to 10-20 nm penetration depth. Si and O distribution proved that the electrode area is oxidized because the plasma preferentially burn in this area, whereas the area between electrodes composed from the trace amount of oxygen.

4 Conclusion

Interaction of silicon surface and atmospheric pressure plasma generated in air at atmospheric pressure was studied. It was proven, that the treated sample strongly affects the plasma properties and its distribution in plasma gap. The experimental data were supplemented by the Comsol model. It was also shown, that the distribution of electric field in the plasma gap depends on the treated material. The material with the higher relative permittivity has a stronger effect on the field distribution. It was experimentally proven, that the plasma converts into the volume DBD generated between Si sample and one electrode. Such exposed surface is slightly oxidized.

4 References

[1] Z. Nishi, R. Doering, CRC Press, Taylor & Francis Group, Boca Raton (2008)

[2] P. Siffert, E. F. Krimmel, Springer – Verlag, Berlin, Heidenberg, New York (2004)

[3] M. Černák, European Patent EP 1387901 B1, (2002)

[4] M. Šimor, J. Ráhel´, P. Vojtek, M. Černák: Appl. Phys. Letters, 81 2 (2002).

[5] M. Černák, L. Černáková, I. Hudec, D. Kováčik, A. Zahoranová: The Eur. Phys. J-Appl. Phys., 47 6 (2009).

[6] M. Černák, J. Ráheĺ, Patent WO 2008085139. (2008).

[7] M. Černák, J. Ráhel, D. Kováčik, M. Šimor, A. Brablec, P. Slavíček: Contrib. Plasma Phys. 44 3 (2004).

[8] A. Pamreddy, D. Skácelová, M. Haničinec, P. Sťahel, M. Stupavská, M. Černák, J. Havel, Surf. Coat. Technol., 236 5 (2013).

[9] D. Skácelová, V. Danilov, J. Schäfer, A. Quade, P. Sťahel, M. Černák, J. Meichsner, Mat.Sci. Engineer:B, 178 5 (2013).

Deposition of Hard Yet Moderately Ductile MoBC Coatings by p-DC Magnetron Sputtering

P. Souček[1], V. Buršíková[1], L. Zábranský[1], J. Buršík[2], P. Vašina[1]

[1]*Department of Physical Electronics, Masaryk University, Brno (Czech Republic),*
E-mail: soucek@physics.muni.cz
[2] *Institute of Physics of Materials of the Academy of Sciences of the Czech Republic, v. v. i., Brno (Czech Republic)*

Novel nanolaminated MoBC coatings were prepared using a combination of non-reactive direct current and pulsed direct current magnetron sputtering. Depending on the deposition conditions the coatings were either of amorphous or of nanocomposite nature. Nanocomposite coatings showed good hardness and Young's modulus and showed no tendency to form cracks even for high-load nanoindentation testing.

1 Introduction

Standard ceramic materials nowadays used as protective coatings such as TiN, TiAlN, c-BN, etc. exhibit high hardness and high stiffness. However these are often connected with brittle behaviour of the coating thus limiting the lifetime of the coating and of the coated tool as well. To overcome these limitations, a new generation of materials with high hardness and moderate ductility is sought for.

Recently, nanolaminate Mo_2BC coatings were predicted to have these advantageous properties [1]. However deposition conditions so far necessary to deposit Mo_2BC coatings are a limiting factor. First, deposition process utilizing combinatorial DC magnetron sputtering required substrate temperature of 900°C was reported [1]. Secondly, a low temperature synthesis method reducing the substrate temperature to 380°C required using High Power Impulse Magnetron Sputtering (HiPIMS) with compound Mo_2BC target [2]. Both of these methods pose significant problems with industrial scale production. High deposition temperatures that are at or above tempering temperature of the tools

would worsen the mechanical properties of the coated tools and HiPIMS technology is still not widely used due to its high cost and relatively complicated operation. Thus a different method to produce crystalline Mo_2BC coatings would be advantageous.

2 Experimental setup

Multi-target sputtering system equipped with four targets (B_4C, C and Mo targets were used) aimed at central RF biasable and up to 750 °C heatable substrate holder was employed for all depositions.

First the hardmetal (cemented tungsten carbide) substrates were ultrasonicated in acetone and then in isopropylalcohol. After insertion in the chamber, the samples were cleaned by argon ion bombardment for 20 minutes. Then the deposition itself commenced, B4C and Mo targets were DC driven, while the C target was connected to a pulsed DC source. Various deposition temperatures were used. Both conditions with and without substrate bias were used.

The crystallinity of the samples was investigated using Rigaku SmartLab diffractometer with Cu Kα radiation in

68

grazing angle of incidence geometry. Surface of the samples was imaged using Tescan MIRA3 scanning electron microscope. Thin lamellas were prepared using FIB on Tescan LYRA 3 XMU FEG/SEMxFIB microscope and the resulting lamellas were imaged using JEOL JEM-2100F transmission electron microscope. The mechanical properties of the coatings were evaluated by TI 950 TriboIndenter by Hysitron.

2 Results and discussion

Pulsed DC plasma generation was used in order to increase the localized heating of the sample due to ion bombardment. Thus in order to quantify the ion flux on the growing film a simple planar Langmuir probe in place of the substrate was used to measure the saturated ion current as a function of the pulsing frequency and the duty cycle. The resulting graph is plotted in Fig. 1. It can be seen that the ion bombardment and in turn also the energy influx of the growing film intensifies as the pulsing frequency is increased and the duty cycle is decreased. Thus pulsing frequency of 350 kHz and duty cycle of 65 % were chosen for coating deposition. The voltage and current waveforms of this pulse are plotted in Fig. 2. The difference in the ion flux with and without pulsing during the deposition is depicted in Fig. 3.

Fig. 2: *Voltage and current waveforms of the pulse used for depositions*
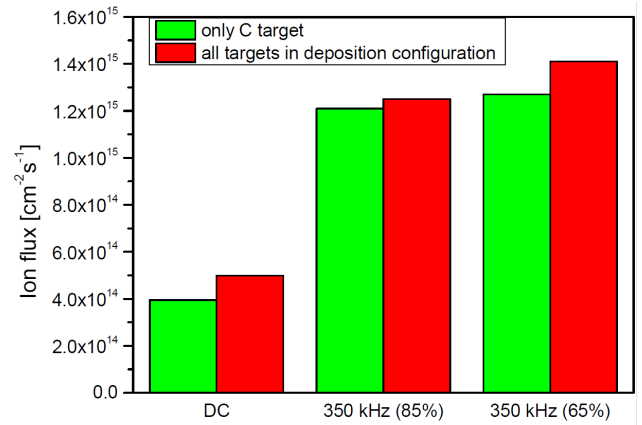
Fig. 3: *Ion fluxes with and without pulsing in deposition configuration. 65% and 85% duty cycles are shown.*

Coatings with (-200 V) and without bias were prepared with C target pulsed at 350 kHz with at different substrate temperatures and the resulting diffractograms presented in Fig. 4. The reference is taken from [2] and position of the peaks corresponding to amorphous (A) and crystalline (C) Mo_2BC phase are marked.

Fig. 1: *Ion flux on the growing film as a function of pulsing frequency and duty cycle.*
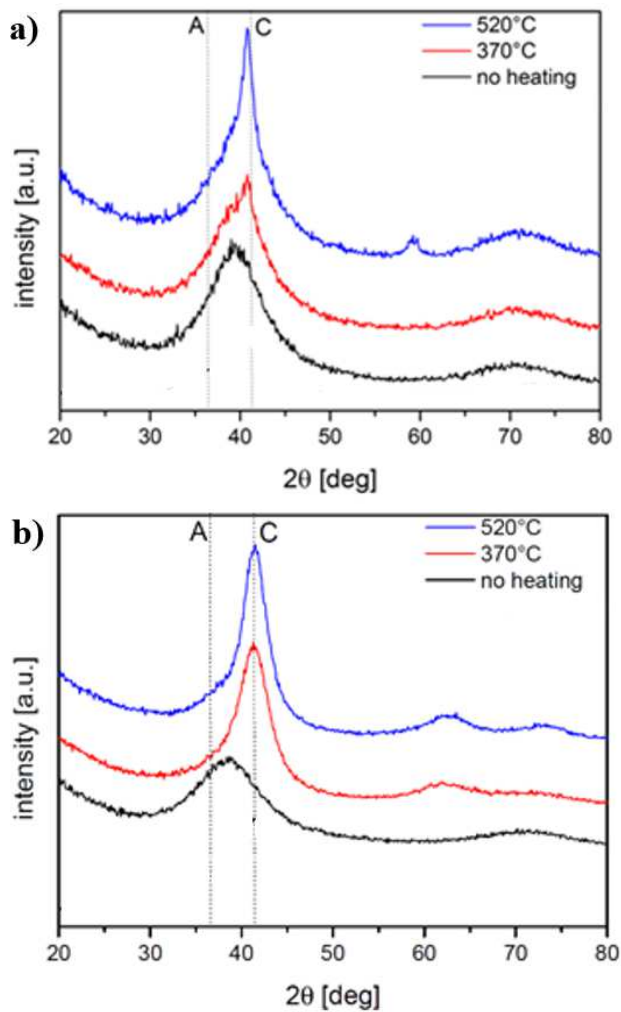
Fig. 4: *XRD patterns of deposited coatings a)*
with -200 V bias b) without bias

Both samples prepared without external heating were amorphous as was proved by TEM and selected area diffraction pattern measurements. Samples prepared at elevated temperatures were of nanocomposite nature with crystalline Mo_2BC phase and another amorphous phase as well.

The hardness and Young's modulus of the **a**morphous as well as nanocomposite coatings were evaluated using nanoindentation technique. The hardness and elastic modulus curves dependence on the depth profile are plotted in Fig. 5a and 5b, respectively. It can be seen that nanocomposite samples show typical hardness of about 30 GPa with elastic modulus about 335 GPa, while the amorphous coatings are considerably softer and show average hardness about 19.5 GPa with elastic modulus about 275 GPa. No pop-in events were detected in the load-displacement curves and also no sudden drops in differential hardness even with cube corner indenter were present, which again indicates no cracking inside the coating.
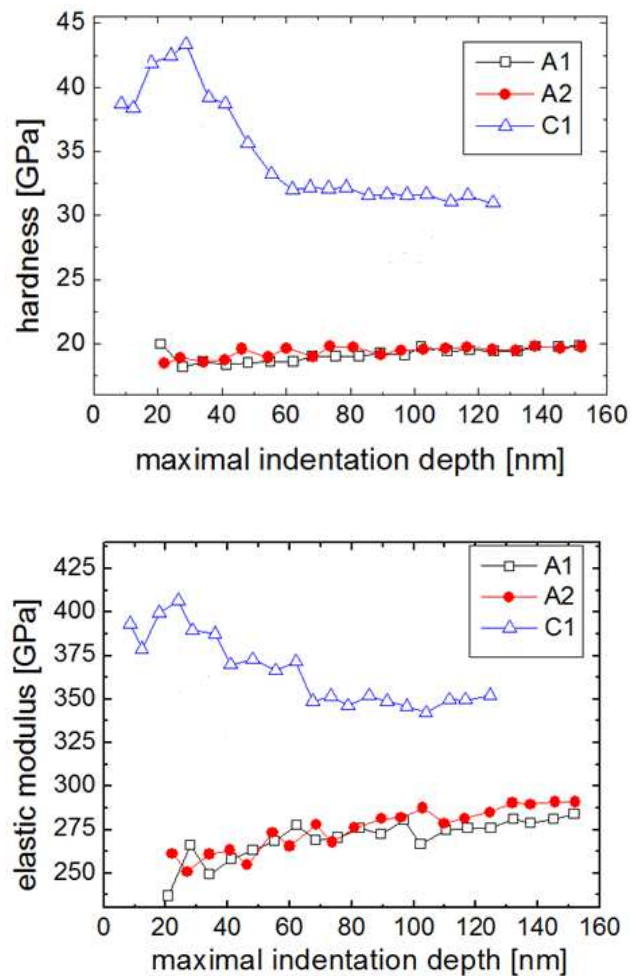
Fig. 5: *Dependence of the hardness and elastic*
modulus on the indentation depth

3 Conclusions

Nanocomposite Mo-B-C coatings were prepared at lower temperature utilizing mid-frequency pulsed DC magnetron sputtering which significantly increases the ion flux and thus the local heating. Coatings exhibit low roughness, good adhesion to metallic substrates, high hardness and no cracks were observed even at high load

indentation tests.

4 Acknowledgment

5 References

[1] J. Emmerlich, D. Music, M. Braun, P. Fayek, F. Munnik, J.M. Schneider, J. Phys. D: Appl. Phys., 2009 42 185406 (6pp).

[2] H. Bolvardi, J. Emmerlich, S. Mráz, M. Amdt, H. Rudigier, J.M. Schneider, Thin Solid Films, 2013 542 5-7

Electrospinning of Biopolymers Suitable for Medical Applications

V. Švachová[1], K. Slánská[2], M. Slánská[3], L. Vojtová[4], D. Pavliňák[5]

[1]*Brno University of Technology, Faculty of Chemistry, Brno (Czech Republic),*
E-mail: xcsvachova@fch.vutbr.cz
[2]*Gymnázium Brno-Řečkovice, Brno (Czech Republic), E-mail: katerina.slanska@seznam.cz*
[3]*Gymnázium Brno-Řečkovice, Brno (Czech Republic), E-mail: misel.slanska@seznam.cz*
[4]*CEITEC – Central European Institute of Technology, Brno University of Technology,*
Brno (Czech Republic), Email: Lucy.Vojtova@ceitec.vubr.cz
[5]*Department of Physical Electronics, Masaryk University Brno (Czech Republic),*
Email: d.pavlinak@mail.muni.cz

This work deals with the preparation of nanofibers for medical application. The type and the concentration of polymer solution exhibited significantly effects influencing the polymer mixture spinnability, the fiber diameter and the physical and chemical properties of the obtained nanofibers. The crosslinking process of nanofibers prepared from water soluble polymer is necessary step to improve water stability, thermo-mechanical properties and to enhance mechanical strength of these nanofibers.

1 Introduction

Nowadays, many people suffer from pain as a result of illness and/or diseases. Therefore, it is necessary to find a new biomaterials' system to treat these diseases and help ill patients. Biomaterials can be in the several type of structure, e.g. scaffolds, porous microsphere, hydrogel or nanofibers. This work deals with nanofibrous mats.

Electrospinning is a simple method for nanofiber production in the range from tens nanometers to several micrometers [1-3]. Prepared nanofibers have many important characteristics including high porosity, mechanical properties and/or high ratio of surface area to mass [4]. Many natural, synthetic or hybrid blends can be spun from their polymer solutions or melt [5,6]. Electrospun nanofibers have various potential applications in different areas such as membrane filtration [7], cosmetics masks [8], military protective clothes [9], nanofibrous sensors [10], scaffolds for tissue engineering [11], wound healing [12] and drug delivery system [13]. Size, density and morphology of nanofibers depend on various parameters including the polymer solution parameters, such as concentration type of solvent, etc., the processing conditions as applied voltage and distance of electrodes and the ambient parameters such as temperature and relative humidity [14-16]. A delicate balance among all the above mentioned parameters leads to the success of the electrospinning process.

Blending polymers with other natural and/or synthetic polymers is aided by tissue engineers to fine tune the desired properties of the prepared electrospun mats. Thus, the presence of bioactive macromolecules in synthetic polymers enhances biocompatibility and bioactivity of electrospun mats. On the other hands, synthetic polymer improves the nanofiber

mechanical properties [17].

In this work, the effect of concentration, the type of solvent and the type of crosslinking agent on the properties of gelatin nanofibers were studied.

2 MATERIALS AND METHODS

2.1 Materials

Gelatin (Type B), 1-ethyl-3-(3-dimethyl-aminopropyl)-1-carbo diimide hydrochloride (EDC), N-hydroxysuccinimide (NHS)–all purchased from Sigma Aldrich), acetic acid (99%, Penta, Czech Republic) and ethanol (p.a., Lachner, Czech Republic) without further purification were used.

2.2 Electrospinning set up

Gelatin solution with concentration 9 wt % and 15 wt% of gelatin was prepared from concentrated acetic acid at room temperature by Nanospider^{TM} technology (NS LAB 500S from Elmarco s r. o.) using rotary spinning electrode.

2.3 Crosslinking of gelatin nanofibers

Two crosslinking methods for the crosslinking process of gelatin nanofibers were used. One of them was dehydrothermal treatment (DHT) and other was the post crosslinking method with carbodiimides.

2.4 Characterizations
2.4.1 Infrared Spectroscopy

Attenuated total reflectance Fourier-transform infrared spectra (ATR-FTIR) were recorded to study the composition of obtained nanofibrous mats using Bruker Vertex80V spectrometer. Spectral range was set from 4000 to 650 cm^{-1}. Each spectrum consists of 128 scans. The spectra were evaluated by OPUS software (version 6.5) using "rubber-band" baseline correction and then by program OriginPro 8.

2.4.2 Scanning Electron Microscopy

The nanofibers were imaged by scanning electron microscope (SEM) Tescan MIRA3. If not specified otherwise, all samples were measured in secondary emission, depth regime with 15 kV. For a better resolution, nanofibers were coated by the 10nm gold layer.

3 Results and Discussion

3.1 The effect of crosslinking process on the chemical composition of nanofibers

The ATR FTIR analysis was examined in the spectral range $4000 – 650$ cm^{-1}. The ATR FTIR spectra of obtained nanofibrous mats are shown in Fig. 1. The ATR FTIR spectrum of pure gelatin nanofibers (black curve) shows Amide A vibration at 3273 cm^{-1} and the absorption band of Amide I at 1632 cm^{-1}. The absorption band at 1532 cm^{-1} region belongs to Amide II vibration. The absorption intensity at 1444 cm^{-1} and 1399 cm^{-1} is representing for CH$_2$ scissoring and asymmetric bending of the CH$_3$ group. At 1332 cm^{-1} occurs valence vibration of C-H band and at 1240 cm^{-1} valence vibration of Amide III band [18].

In the case of post crosslinked gelatin nanofibers with carbodiimides (blue curve), ATR spectrum exhibits new band at 1730 cm^{-1} that is characteristics for C=O vibration. This new carbonyl group probably created during the crosslinking reaction between amino and carboxyl groups of the gelatin. DHT treatment did not cause any visible changes in the ATR-FTIR spectrum of gelatin nanofibers (red curve).

3.2 The effect of polymer concentration on the nanofibrous structure

To compare the effect of concentration on the gelatin nanofibrous structure, gelatin nanofibers from 9 and 15wt % of gelatin solutions were prepared. The SEM images showed uniform structure of both samples, as

can be seen in Fig. 2. Moreover, 15wt % gelatin nanofibers had three times thicker fiber diameter than 9wt% gelatin nanofibers which is in agreement with the literature [19,20].
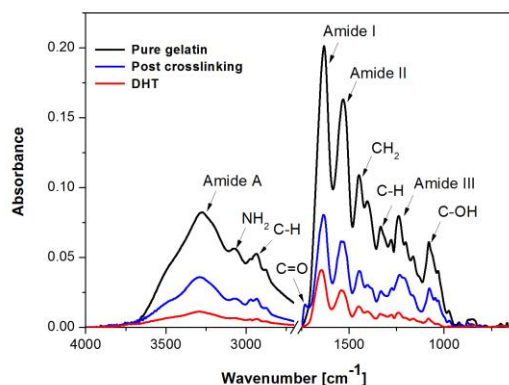
Fig. 1: *ATR-FTIR spectra of nanofibers: pure gelatin nanofibers (black curve), gelatin nanofibers post crosslinked with carbodiimide (blue curve) and gelatin nanofibers crosslinked by DHT treatment (red curve).*
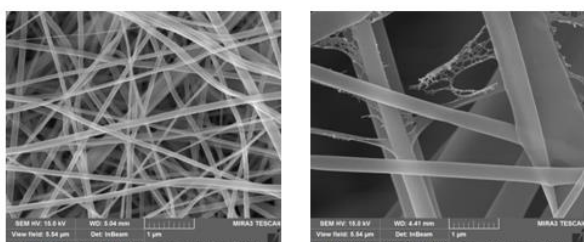
Fig. 2: *SEM images of obtained gelatin nanofibers. Gelatin nanofibers spun from 9wt % gelatin solution are depicted on the left and from 15wt % gelatin solution are on the right.*

3.3 The effect of solvent on nanofiber surface structure

It is well known that the presence of acetic acid effects the surface tension of solutions in a way which the surface tension could be decreased by increasing acetic acid concentration [19]. Gelatin can be easily dissolved in water, however gelatin/water solution was not applicable for gelatin nanofibers production [20]. Increasing concentration of acetic acid led from beads over defects to nanofiber production. Using

concentrated acetic acid homogenous gelatin nanofibers with the fiber diameter of 102 ± 20 nm were obtained. Fig. 3 illustrates the gelatin (9wt %) structures electrospun from the increasing concentration of acetic acid.
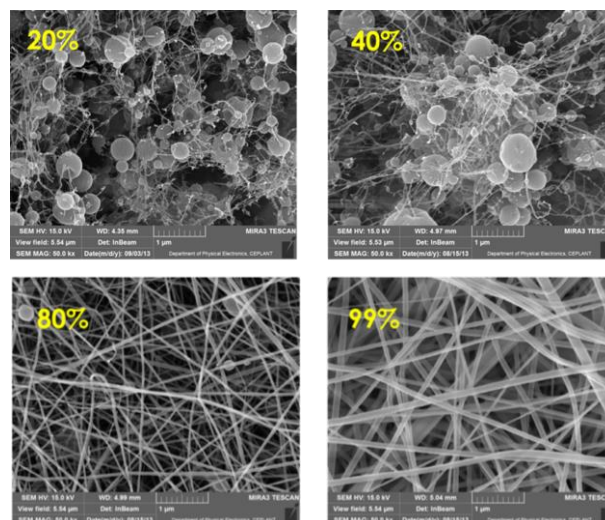
Fig. 3: *SEM images of obtained gelatin structure spun from increasing acetic acid concentration.*

3.4 The effect of crosslinking on nanofibrous gelatin structure

SEM pictures of obtained crosslinked gelatin nanofibers are shown in Fig. 4. Post crosslinking treatment with carbodiimide caused the sintering of gelatin nanofibers. On the other hand, gelatin nanofibers crosslinked by DHT kept their origin fibrous structure. Fiber diameter these nanofibers increased to 144 ± 25 nm, it can be caused by moisture of gelatin nanofibers.
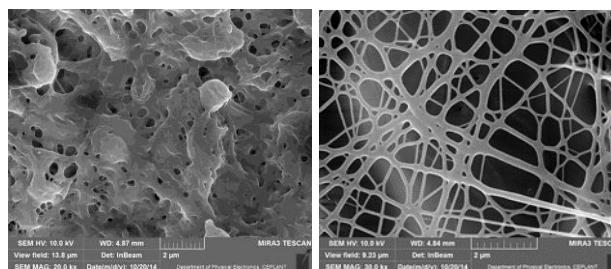
Fig. 4: *SEM images of crosslinked gelatin nanofibers. On the left post crosslinked gelatin nanofibers with carbodiimides are shown. On the right crosslinked gelatin nanofibers by*

DHT treatment are illustrated.

4 Conclusion

Gelatin nanofibers from acetic acid and crosslinked gelatin nanofibers were prepared. The effect of concentration, the type of solvents and type of crosslinking on the chemical composition and the surface morphology of obtained gelatin nanofibers were studied. With the increasing concentration of gelatin solution raised the fiber diameter of prepared gelatin nanofibers. With the growing concentration of acetic acid gelatin beads, defects and finally homogenous nanofibers were obtained. The type of crosslinking process of gelatin nanofibers played also important role on the surface morphology of nanofibers.

5 Acknowledgment

6 References

[1] J. Doshi, D.H. Reneker: Journal of Electrostatics 35 (1995), 151 - 160.

[2] Z. M. Huang, Y. Z. Zhang, M. Kotaki, S. Ramakrishna: Composites Science and Technology 63 (2003), 2223 – 2253.

[3] D. H. Reneker, I. Chun: Nanotechnology 7 (1996), 216 – 223.

[4] G. Jiang, S. Zhang, X. Qin, R. S. Tuan, F. K. Ko, Z. Fan, G. M. Glenn, W. J. Orts, W. R. MacLellan: Journal of Industrial Textiles 196 (2011), 1024 - 1031.

[5] D. Pavlinak, V. Svachova, L. Vojtek, J. Zarzycka, P. Hyrsl, M. Alberti, L. Vojtova: Open Chemistry 13 (2015), 229 - 235.

[6] D. Pavlinak, J. Hnilica, A. Quade, J. Schafer, M. Alberti, V. Kudrle: Polymer Degradation and Stability 108 (2014), 48 – 55.

[7] R. Gopal, S. Kaur, Z. Ma, C. Chan, S. Ramakrishna, T. Matsuura, L.C. du Toit, V.M.K. Ndesendo: Journal of Membrane Science 281 (2006), 581 – 586.

[8] Q. Z. Gu: CN Patent App. CN 200810195080 (2009).

[9] S. Lee, S. K. Obendorf, J. D. Schiffman, I. S. Kim, N. Bhattarai, P. Kumar, L. C. du Toit, V. M. K. Ndesendo: Journal of Applied Polymer Science 102 (2006), 3430 – 3437.

[10] T. Kowalczyk, A. Nowicka, D. Elbaum, T. A. Kowalewski: Biomacromolecules 9 (2008), 2087 – 2090.

[11] P. Zahedi, I. Rezaeian, S. O. Ranaei-Siadat, S. H. Jafari, P. Supaphol, P. Kumar, L. C. du Toit, V. M. K. Ndesendo: Polymers for Advanced Technologies 2013 (2009), 75 – 95.

[12] M. S. Khil, D. I. Cha, H. Y. Kim, I. S. Kim, N. Bhattarai, P. Kumar, L. C. du Toit, V. M. K. Ndesendo: Journal of Biomedical Materials Research 67B (2003), 675 -679.

[13] T. J. Sill, H. A. von Recum, S. K. Young, A. Subramanian, Y. W. Tong, L. Y. Yung, D. W. Hutmacher, C. Sheppard, M. Raghunath, B. M. Min: Biomaterials 29 (2008), 1989 – 2006.

[14] G. Jiang, S. Zhang, X. Qin, R. S. Tuan, F. K. Ko, Z. Fan, G. M. Glenn, W. J. Orts, W. R. MacLellan: Journal of Industrial Textiles 196 (2011), 1024 – 1031.

[15] N. G. Rim, C. S. Shin, H. Shin: Biomedical Materials 8 (2013), 014102 -014110.

[16] A. Rogina: Applied Surface Science 296 (2014), 221 – 230.

[17] W. He, T. Yong, W. E. Teo, Z. Ma, S. Ramakrishna, Y. Wang, A. S. Weiss:

Tissue Engineering 11 (2005), 1574 – 1588.

[18] C. Yang, X. Wu, Y. Zhao, L. Xu, S. Wei: Journal of Applied Polymer Science 121 (2011), 3047 – 3055.

[19] C. S. Ki, D. H. Baek, K. D. Gang, K. H. Lee, I. C. Um, Y. H. Park: Polymer 46 (2005), 5094 – 5102.

[20] M. Erencia, F. Cano, J. A. Tornero, M. M. Fernandes, T. Tzanov, J. Macanas, F. Carillo: Journal of Applied Polymer Science 132 (2015), 42115 - 42126

[20] S. Heydarkhan-Hagvall, K. Schenke-Layland, A. P. Dhanasopon, F. Rofail, H. Smith, B. M. Wu, R. E. Beygui, W. R. MacLellan: Biomaterials 29 (2008), 2907 – 2914.

Study of the adhesion of nc-TiC/a-C:H coatings deposited on steel substrates

<u>L. Zábranský</u>[1], V. Buršíková[1], P. Souček[1], P. Vašina[1]

[1]*Department of Physical Electronics, Masaryk University, Brno (Czech Republic), E-mail: zerafel@mail.muni.cz*

This work is aimed on the study of adhesion of nc-TiC/a-C:H coatings with or without titanium interlayer. These coatings were prepared using standard DC magnetron sputtering with unbalanced configuration of magnetic field and HiPIMS. The scratch test and the differential hardness measurements results were compared.

1 Introduction

Nanocrystalline titanium carbide embedded in an hydrogenated amorphous carbon matrix (nc-TiC/a-C:H) shows high hardness and Young's modulus together with low wear and low friction coefficient [1-7]. Because the adhesion of nc-TiC/a-C(:H) films to industrially attractive substrates is often poor, an adhesion promoting interlayer is routinely introduced to overcome this problem. Usually titanium [8] or chromium [9] interlayers are employed. A wide variety of preparation processes have been developed over the years including reactive magnetron sputtering of Ti target in hydrocarbon containing atmosphere [7, 10,11], where the hydrogenized carbon matrix a-C:H is formed due to the presence of hydrogen in a hydrocarbon precursor. On the other hand, using co-sputtering of Ti and C targets [4], the hydrogen-free amorphous carbon matrix a-C is formed.

By the deposition of the titanium interlayer prior to the deposition of the coating, a superior adhesion to hard-metal or high speed steel (HSS) substrates can be achieved. This adhesion in case of Ti interlayer prepared on HSS substrate can sustain temperatures up to 700 °C, as it was shown in our previous work [12]. This paper discuss the necessity of the presence of the titanium interlayer and its impact on the adhesion of nc-TiC/a-C:H coatings. For this purpose, several nc-TiC/a-C:H coatings with different [Ti]/[C] ratio were tailored using hybrid PVD-PECVD process with the DC power of 1.5 kW and with the unbalanced configuration of magnetic field. The RF bias of -100 V on the substrate holder was used. Additionally, the HiPIMS with the power of 1.5 kW was used for preparation of two samples in order to compare the effect of high ion energy bombardment with the low energy in case of DC process. The puls duration was 1200 μs, the puls frequency was set to 20 Hz and the off-time was 48.8 ms. In both cases the buffer gas was argon and the reactive gas was acetylene. The deposition time was always 60 minutes.

2 Results and discussion
2.1 Prepared samples

In Tab.1 there is a summary of preparation method, thickness of the interlayer, the thickness t of coatings and the chemical composition which was measured by EDX for all prepared samples. Because the EDX cannot reliable measure the C content, all these results of chemical composition in Tab.1 should be taken only indicatively in order to roughly compare all the samples. The thickness, evaluated by mechanical

profilometry, was significantly lower for both samples prepared using HiPIMS because of the lower deposition rate (the deposition time was always 60 minutes). Therefore, the lower thickness will infuence the measurement on scratch test and the critical loads cannot by directly compared with the critical loads found for samples prepared with DC sputtering. In this case, only the prevailing failure mode was compared. The value of the thickness t is including the potential thickness of the interlayer.

sample	prep. method	Ti interlayer	t [µm]	Ti at.%	C at.%
1	DC	~700 nm	5.4	18	73
2	DC	~700 nm	6.5	66	34
3	DC	~700 nm	5.4	58	42
4	HiPIMS	~300 nm	2.4	19	81
5	HiPIMS	~300 nm	2.1	72	28
6	DC	-	6.2	66	34
7	DC	-	6.5	71	29
8	DC	-	6.7	56	44

Tab.1: *Summary of all prepared samples, their thickness t, interlayer and chemical composition focused on C content and Ti content evaluated by EDX.*

2.2 Hardness, elastic modulus and differential hardness

Prior to the scratch test the mechanical properties such as hardness and elastic modulus were measured using the nanoindentation technique on Fisherscope H100 equipped with Berkovich tip. The results are shown in Tab.2. For this purpose, the correct load using which the substrate or the interlayer did not infuence the measurement was found. Using the measurement of the differential hardness [13, 14] also on Fisherscope H100, the threshold load where the underlying layer starts to influence the measurement of hardness was found as it is shown in Fig.1 for sample 1 and in Fig.2 for sample 5. The onset of smooth (not sudden) increase or decrease of the differential hardness with increase of

penetration depth determines the threshold load which occurs in certain critical depth.

sample	load [mN]	H [GPa]	E [GPa]	H/E	H^3/E^2
1	100	9.6 ± 0.4	90 ± 2	0.101	0.093
2	100	9.0 ± 0.9	190 ± 10	0.047	0.020
3	100	17.0 ± 1.1	230 ± 7	0.074	0.093
4	40	14.6 ± 0.6	90 ± 1	0.146	0.311
5	40	20.7 ± 0.6	210 ± 5	0.099	0.201
6	100	14.5 ± 1.5	220 ± 11	0.066	0.063
7	100	6.6 ± 0.8	170 ± 13	0.039	0.010
8	100	11.8 ± 3.5	230 ± 36	0.051	0.031

Tab.2: *Hardness and elastic modulus for all samples with calculated H/E ratio (toughness) and resistance to plastic deformation H^3/E^2 with highlighted highest results.*
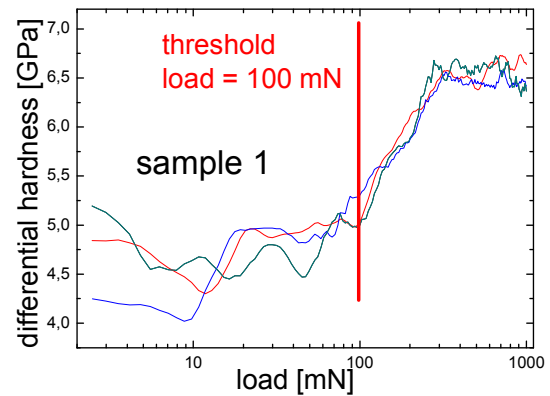
Fig.1: *Differential hardness for sample 1 where the hardness of the coating was lower than that of the substrate.*
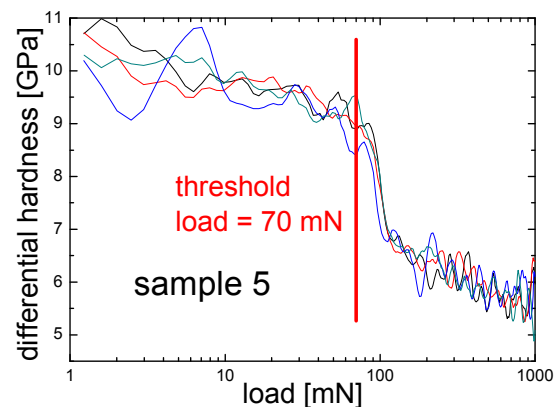
Fig.2: *Differential hardness for sample 5 where the hardness of the coating was higher than that of the substrate.*

In case of hard coating (see Tab.2), with

hardness higher than that of the substrate (11 GPa), the critical depth corresponded to size of the plastic zone calculated using Johnson contact model [15]. According to measurement of differential hardness, the suitable load was chosen – 100 mN for samples prepared by DC sputtering, 40 mN for samples prepared by HiPIMS (here the load is lower due to lower overall thickness).

Measurement of differential hardness can also detect cracking in the vicinity of the tip for which there is a typical behavior in differential hardness curve – a sudden drop. In our case, no sudden drops in case of all samples were observed, i.e. no cracks occurred for loads up to 1 N which was confirmed using scanning electron microscope Mira 3 FEG-SEM (see Fig. 3, here for sample 6).
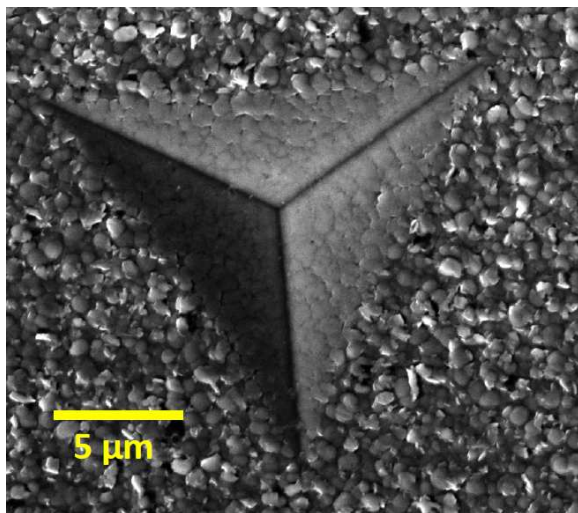
Fig.3: *SEM image of the residual 1 N imprint. No cracking inside, around or from the corners of the imprint observed.*

2.3 Scratch test

The scratch measurements were performed on Revetest Xpress from CSM Instruments. The Rockwell indenter with diameter of 200 nm was used. The progressive mode of loading from 1 N up to 71 N was set with the loading rate of 40 N/min. Several scratches per sample with the line length of 8 mm were performed and afterwards scanned using confocal microscope LEXT OLS4000 with 405 nm semiconductor laser.

Three critical loads L_C were defined: L_{C1} was defined as the actual applied load on the indenter where first isolated defect occurred, L_{C2} was defined as load with continuous cohesive failure and, finally, L_{C3} was the load that corresponded with the onset of continuous adhesive failure. It is important to state that it wasn't always possible to distinguish between adhesive and cohesive failure, therefore, the combination of both types of failure was recorded as L_{C3} value (see Fig.4). The results of critical loads with the probability that this failure mode occurred, average roughness measured by confocal microscope and a short comment about prevailing deformation mode are presented in Tab.3.
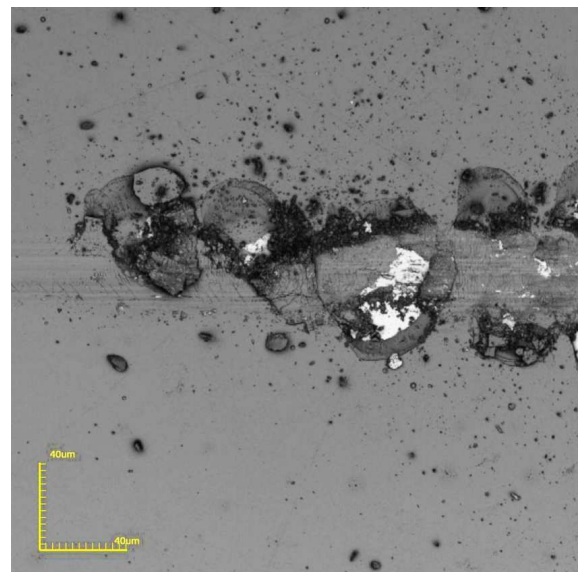
Fig.4: *Image of ridge spallation from confocal microscope, the typical representative of mixture of adhesive and cohesive failure where we cannot reliably state which mode prevailed.*

The best cohesive and adhesive properties had the sample with high Ti content prepared by DC sputtering and containing Ti interlayer (sample 2). From Tab.3 when comparing samples 2, 6 and 7 (similar composition), we can see that absence of Ti interlayer caused

decrease of adhesion (the prevailing failure mode was adhesive). And the more Ti content the film has, the greater the decrease is. But when compared samples 3 and 8, both containing more carbon, we can see that there is no decrease of adhesion. The low values of critical loads for samples 4 and 5 are partially caused by their lower thickness. On the other hand, the adhesion of samples with coatings with higher C content – see and compare samples 1 and 8 where the ratio of [Ti]/[C] is close to 50/50 – the adhesion is almost independent of the presence of the Ti interlayer.

sample	R_a [μm]	L_{C1} [N]	L_{C2} [N]	L_{C3} [N]	comment
1	12 ± 2	17 ± 4 (38%)	23 ± 5 (100%)	27 ± 9 (100%)	cohesive + adhesive
2	50 ± 3	37 ± 6 (67%)	-	-	only isolated defects
3	50 ± 3	30 ± 8 (60%)	37 ± 2 (100%)	39 ± 3 (100%)	cohesive + adhesive
4	7 ± 1	4 ± 2 (60%)	9 ± 5 (100%)	21 ± 12 (40%)	mostly cohesive failure
5	8 ± 1	12 ± 3 (60%)	15 ± 6 (100%)	20 ± 4 (60%)	cohesive + adhesive
6	34 ± 3	23 ± 3 (86%)	-	35 ± 3 (100%)	adhesive failure
7	50 ± 4	16 ± 1 (33%)	-	19 ± 2 (100%)	adhesive failure
8	85 ± 4	34 ± 5 (43%)	40 ± 6 (100%)	40 ± 6 (100%)	cohesive + adhesive

Tab.3: *Summary of results from sratch test and confocal microscope. The average roughness R_a, the critical loads L_{C1}, L_{C2} and L_{C3}, including the probability that this failure mode occured, are compared here with short comment.*

3 Conlusion

In conclusion, several nc-TiC/a-C:H coatings have been prepared with or without the Ti interlayer using DC magnetron sputtering or HiPIMS. Using indentation test the values of hardness and Young modulus have been found correctly without the influence of underlying layers or substrate. From differential hardness curves the first information about the behavior of the coating-substrate or coating-Ti interlayer interface has been obtained. No sudden drops implied that no indentation induced cracking occured which has been confirmed by SEM images of residual imprints.

Using scratch test and defining three critical loads the dominant type of failure has been determined for each sample. The best cohesive and adhesive properties had the sample with high Ti content prepared by DC sputtering and containing Ti interlayer. It was proven that this interlayer plays crucial role to substrate-coating integrity especially for coatings with high Ti content. The critical loads of titanium rich samples without the interlayer was significantly lower compared to samples prepared with the interlayer. For samples with composition close to C/Ti = 50/50 the adhesion is almost independent of the presence of the interlayer

4 Acknowledgment

5 References

[1] Y. Wang, X. Zhang, X. Wu, H. Zhang, X. Zhang, Appl. Surf. Sci. 255 (2008), 1801-1805

[2] P. Souček, T. Schmidtová, L. Zábranský, V. Buršíková, P. Vašina, O. Caha, M. Jílek, A. E. Mel, P.Y. Tessier, J. Schäfer, J. Buršík, V. Peřina, R. Mikšová, Surf. Coat. Tech. 211 (2012), 111-116

[3] A. Czyżniewski, W. Prechtl., J. Mater. Process. Technol. 157-158 (2004), 274

[4] J.C. Sánchez-López, D. Martínez--Martínez, C. López-Cartes, A. Fernández, Surf. Coat. Tech. 202 (2008), 4011-4018

[5] D.M. Cao, B. Feng, W.J. Meng, L.E. Rehn, P.M. Maldo, M.M. Khonsari, Appl. Phys. Lett. 79/3 (2001), 329-331

[6] Y.T. Pei, D. Galvan, J.Th.M. De Hosson, C. Strondl, J. Eur. Ceram. Soc. 26 (2006), 565-570

[7] J. Musil, P. Novák, R. Čerstvý, Z. Soukup, J. Vac. Sci. Technol. A 28(2) (2010), 244-249

[8] Y. Hu, L. Li, X. Cai, Q. Chen, P.K. Chu, Diam. and Relat. Mater. 16 (2007), 181-186

[9] Y.T. Pei, D. Galvan, J.Th.M. De Hosson, A. Cavaleiro, Surf. Coat. Technol. 198 (2005), 44-50

[10] W. Gulbinski, S. Mathur, H.Shen, T. Suszko, A. Gilewicz, B. Warcholinski, Appl. Surf. Sci. 239 (2005), 302-310

[11] K. Polychronopoulou, C. Rebholz., M.A. Baker, L. Theodorou, N.G. Demas, S.J. Hinder, A.A. Polycarpou, C.C. Doumanidis, K. Böbel, Diam. and Relat. Mater. 17 (2008), 2054-2061

[12] L. Zábranský, V. Buršíková, P. Souček, P. Vašina, T. Gardelka, P. Sťahel, O. Caha, V. Peřina, J. Buršík, Surf. Coat. Technol. 242 (2014) 62-67

[13] B. Wolf, A. Richter, New Jour. of Physics 5 (2003), 15.1-15.17

[14] B. Wolf, Mag. And Phil. Mag. Lett. 86 (2006), 5251-5264

[15] K.L. Johnson, J. Mech. Phys. Solids 18 (1970), pp 115-126

Potential Application of Plasma and Nanomaterials 2015

Book of Contributed Papers

12th November – 13th November 2015
Brno, Czech Republic

muni
PRESS